

https://dspace.org/

The determination of form drag coefficient for rigid, emergent objects in open channel flow

Jackson, Kyle Sheldon

2017

http://hdl.handle.net/10539/22962

Jackson, Kyle Sheldon (2017) The determination of form drag coefficient for rigid, emergent objects in open channel flow, University of the Witwatersrand, Johannesburg, <http://hdl.handle.net/10539/22962>

Downloaded from a DSpace repository. https://dspace.org/

THE DETERMINATION OF FORM DRAG COEFFICIENT FOR RIGID, EMERGENT OBJECTS IN OPEN CHANNEL FLOW

Kyle Sheldon Jackson

A research report submitted to the Faculty of Engineering and the Built Environment, University of the Witwatersrand, Johannesburg, in partial fulfillment of the requirements for the degree of Master of Science in Engineering

Johannesburg, 2017

DECLARATION

I declare that this research report is my own unaided work. It is being submitted to the Degree of Master of Science to the University of the Witwatersrand, Johannesburg. It has not been submitted before for any degree or examination to any other University.



……

……9th……day of.....February.....year……2017……

ABSTRACT

The development of methods which are better able to predict the effect of large scale emergent roughness elements on the flow characteristics requires a better understanding of the drag coefficient under conditions likely to occur in the field. A laboratory investigation was carried out with newly developed equipment to quantify the drag force on various shaped cylinders, as well as the drag on an individual cylinder surrounded by an array of cylinders. The relationship between the drag coefficient and cylinder Reynolds number for a single circular cylinder was found to be of similar form but larger in magnitude than the established relationship for an infinitely long cylinder; the relationship departs from the infinite cylinder relationship for low cylinder Reynolds numbers. Contrary to previous research, the results for the multiple cylinder investigation did not reveal a clear relationship between the cylinder density and drag coefficient. Equations were developed and verified with existing laboratory data. These should be improved and extended by further research for field use.

ACKNOWLEDGEMENTS

This research report is the culmination of many hours spent in the laboratory afterhours and over weekends. The journey getting to this point required overcoming a number uncontrollable obstacles and setbacks. The road was littered with frustration but ultimately the satisfaction of seeing the fruits of my labour were worth all the tribulations.

I would like to thank **Professor Chris James** for his patience, knowledge and support throughout the project. I am extremely grateful for the numerous consultations and discussions which combined with his calm and friendly demeanor kept me on track.

A special thanks to my girlfriend **Talisha Britz** who was present with me at all times in the laboratory ensuring I was safe, lending a helping hand, recording readings and keeping me semi calm and sane. I am deeply indebted to her for bearing the brunt of my frustrated rants and perfectionist tendencies which found ourselves in the laboratory well past midnight on a few occasions. It is hard to imagine completing this report without her unwavering support and patience.

I would like to thank **Mr Wayne Costopoulos** for his ever willingness to help me construct various components of the apparatus and his willingness to answer phone calls on weekends to guide me to a solution for any mechanical problem I experienced in the laboratory.

To the engineering library staff at the University of the Witwatersrand, I am grateful for the work done by them in sourcing numerous old and forgotten journal articles for me.

Lastly to my friends and family for their support, patience and encouragement throughout the project.

CONTENTS

ABSTRACT i

ACKNOWLEDGEMENTS ii

CONTENTS iii

LIST OF FIGURES v

LIST OF TABLES x

LIST OF SYMBOLS xi

1 Introduction 1-1

1.1 Layout of the thesis 1-5

2 Background 2-1

3 Experimental Investigation 3-1

3.1 Introduction 3-1

3.2 Apparatus 3-2

3.2.1 Configuration 1 3-3

3.2.2 Configuration 2 3-5

3.2.3 Configuration 3 3-8

3.3 Calibration 3-13

3.4 Verification tests 3-15

3.5 Single cylinder experiments 3-20

3.6 Multiple cylinder experiments 3-25

4 Results 4-1

4.1 Calibration tests 4-1

4.1.1 Tension sensor 4-1

4.1.2 Configuration 1, 2 and 3 4-2

4.1.3 Conclusion 4-5

4.2 Verification tests 4-5

4.2.1 Results 4-5

4.2.2 Conclusion 4-9

4.3 Single circular cylinder experimental investigation 4-9

4.3.1 Results 4-10
4.3.2 Conclusion 4-16
4.4 Single square cylinder experimental investigation 4-17
4.4.1 Results 4-17
4.4.2 Conclusion 4-20
4.5 Single diamond cylinder experimental investigation 4-21
4.5.1 Results 4-21
4.5.2 Conclusion 4-25
4.6 Multiple circular cylinder experimental investigation 4-26
4.6.1 Results 4-26
4.6.2 Conclusion 4-36
5 Application for resistance prediction 5-1
5.1 Results 5-4
5.2 Conclusion 5-6
6 Conclusions 6-1
6.1 Single cylinder experimental investigations 6-1
6.2 Multiple cylinder experimental investigation 6-1
6.3 Recommendations for further research 6-2
7 References 7-1
APPENDIX A A1
APPENDIX B B1
APPENDIX C C1
APPENDIX D D1
APPENDIX E E1

LIST OF FIGURES

Figure 1-1: Leonardo da Vinci's “Old man with water studies”. (Reuteler, 1994) 1-4

Figure 1-2: Leonardo da Vinci's “Studies of water passing obstacles”. (Reuteler, 1994) 1-4

Figure 2-1: Description of the different experimental variables (Ranga Raju, et al., 1983). 2-2

Figure 2-2: Variation of drag force with flow depth and the influence of blockage (d/B) on this relationship. The graph on the right is for a higher discharge and flow depth and therefore has a slightly higher Froude number than the left graph (Ranga Raju, et al., 1983). 2-2

Figure 2-3: Relationship between drag coefficient and areal rod concentration. The different shape represents the different bed slopes as shown (Ishikawa, et al., 2000). 2-4

Figure 2-4: Relationship between drag coefficient and Froude number. (Ishikawa, et al., 2000)..... 2-4

Figure 2-5: Effect of flow depth and stem density on Manning's n. (James, et al., 2004). 2-10

Figure 2-6: Measured and predicted values of F_f for round stems. The solid lines represent calculated F values and the broken lines represent calculated F_f values. (James, et al., 2004)..... 2-10

Figure 2-7: Relationship between the normalized drag and cylinder Reynolds number. Solid lines mark the linear regression for each λ. Grey lines represent Koch and Ladd’s (1997) numerical results at $\lambda = 0.05$ (solid line), 0.2 (dotted line), and 0.4 (dash-dotted line). (Tanino & Nepf, 2008). 2-12

Figure 2-8: Relationship between α_0, α_1 and cylinder areal concentration. (Tanino & Nepf, 2008). 2-12

Figure 2-9: Relationship between the drag coefficient and cylinder Reynolds number for various cylinder concentrations. (Tanino & Nepf, 2008)..... 2-13

Figure 2-10: Variation of F_D with V_c^2 (Kothyari, et al., 2009). 2-15

Figure 2-11: Variation of C_D with R_d and λ (Kothyari, et al., 2009). 2-16

Figure 2-12: Contributions of pressure drag, friction drag, and bed shear to the total energy loss in flow through various cylinder densities and Reynolds numbers. (Stoesser, et al., 2010). 2-18
Figure 2-13: Normalized drag force as a function of cylinder Reynolds number for various cylinder densities. (Stoesser, et al., 2010). 2-19
Figure 2-14: Drag coefficient C_D as a function of cylinder Reynolds number for various cylinder densities (lines represent data of Tanino and Nepf 2008). (Stoesser, et al., 2010). 2-20
Figure 2-15: Two scenarios proposed by Cheng (2013). Dashed lines show control volume. 2-23
Figure 2-16: Variation of drag coefficient with cylinder Reynolds number for a single isolated cylinder in open channel flow (Cheng, 2013). 2-24
Figure 2-17: Comparison of calculated and measured average velocities through cylindrical stems (Cheng, 2013). 2-25
Figure 2-18: Variations of drag coefficient with Reynolds number and cylinder concentrations (Cheng, 2013). 2-25
Figure 2-19: Generalized relationship between drag coefficient and Reynolds number for different cylinder configurations (Cheng, 2013). 2-26
Figure 3-1: Flume A. School of Civil and Environmental Engineering Hydraulics Laboratory. 3-1
Figure 3-2: Lorenz Messtechnik K-1107 10 Newton tension force sensor photograph. (Lorenz Messtechnik GmbH, 2015) 3-2
Figure 3-3: Configuration 1 apparatus set up. (Madhi & Bismilla, 2014) 3-3
Figure 3-4: Configuration 1 sliding mechanism 3-4
Figure 3-5: Close-up of ball bearing tracks. 3-5
Figure 3-6: Configuration 2 schematic. Longitudinal and cross sections. 3-6
Figure 3-7: Close-up of configuration 2 sliding mechanism. 3-7
Figure 3-8: Stabilizing mechanism. 3-7
Figure 3-9: Configuration 3 schematic. 3-9
Figure 3-10: Tension tensor mechanism. 3-11
Figure 3-11: Calibration set-up 3-13
Figure 3-12: Verification test set-up. 3-16

Figure 3-13: Horizontal cylinder support..... 3-17
Figure 4-1: Load measured versus load applied for tension sensor. 4-2
Figure 4-2: Load measured versus load applied for Configuration 1. 4-3
Figure 4-3: Load measured versus load applied for Configuration 2 (static). 4-3
Figure 4-4: Load measured versus load applied for Configuration 2 (dynamic) . 4-4
Figure 4-5: Load measured versus load applied for Configuration 3. 4-4
Figure 4-6: Drag coefficient vs Reynolds number for infinitely long cylinder (local velocity)..... 4-7
Figure 4-7: Drag coefficient vs Reynolds number for infinitely long cylinder (average velocity)..... 4-8
Figure 4-8: Drag force vs local velocity^2 for infinitely long cylinder..... 4-8
Figure 4-9: Drag force vs cylinder Reynolds number for an infinitely long cylinder 4-9
Figure 4-10:Photograph of von Kármán vortex street behind test cylinder..... 4-10
Figure 4-11: Photograph of dye being displaced in front and at the base of the cylinder by the horseshoe vortices. 4-11
Figure 4-12:Relationship between drag coefficient and cylinder Reynolds number for a single emergent circular cylinder..... 4-13
Figure 4-13: Comparison of various researchers reported data sets for drag coefficient versus cylinder Reynolds number 4-14
Figure 4-14: Relationship between drag force and velocity squared for a single emergent circular cylinder..... 4-15
Figure 4-15: Single circular cylinder curve fitting..... 4-16
Figure 4-16: Relationship between drag coefficient and cylinder Reynolds number for a square cylinder..... 4-18
Figure 4-17: Relationship between drag force and average flow velocity for a square cylinder..... 4-18
Figure 4-18: Relationship between drag force and average flow velocity squared for a square cylinder. 4-19
Figure 4-19: Single square cylinder curve fitting. 4-20
Figure 4-20: Relationship between drag coefficient and cylinder Reynolds number for a diamond cylinder. 4-22

Figure 4-21: Relationship between drag force and average flow velocity for a diamond cylinder. 4-23
Figure 4-22: Relationship between drag force and average flow velocity squared for a diamond cylinder. 4-23
Figure 4-23: Single diamond cylinder curve fitting. 4-24
Figure 4-24: Comparison of drag coefficient vs cylinder Reynolds number relationships for circular, square and diamond shaped cylinders. 4-25
Figure 4-25: Relationship between drag coefficient and cylinder Reynolds number for Combination 1 4-27
Figure 4-26: Relationship between drag force and average flow velocity for Combination 1 4-28
Figure 4-27: Relationship between drag force and average flow velocity squared for Combination 1 4-28
Figure 4-28: Relationship between drag coefficient and cylinder Reynolds number for Combination 2 4-29
Figure 4-29: Relationship between drag force and average flow velocity for Combination 2 4-29
Figure 4-30: Relationship between drag force and average flow velocity squared for Combination 2 4-30
Figure 4-31: Relationship between drag coefficient and cylinder Reynolds number for Combination 3 4-30
Figure 4-32: Relationship between drag force and average flow velocity for Combination 3 4-31
Figure 4-33: Relationship between drag force and average flow velocity squared for Combination 3 4-31
Figure 4-34: Relationship between drag coefficient and cylinder Reynolds number for Combination 4 4-32
Figure 4-35: Relationship between drag force and average flow velocity for Combination 4 4-32
Figure 4-36: Relationship between drag force and average flow velocity squared for Combination 4 4-33

Figure 4-37: Comparison of drag coefficient vs cylinder Reynolds number relationships for the four Combinations..... 4-35
Figure 4-38: Multiple cylinder regression analysis..... 4-35
Figure 5-1: Cylinder spacing for series A experiments. Series B and C were created by removing cylinders from this pattern. (Heyneke, et al., 2014) 5-2
Figure 5-2: Measured discharge versus predicted discharge 5-5

LIST OF TABLES

Table 1: Experimental conditions (James, et al., 2004) 2-9
Table 3-1: Single cylinder experimental conditions 3-22
Table 3-2: Multiple cylinder experimental conditions 3-26
Table 5-1: Heyneke et al. (2014) experimental conditions 5-1
Table 5-2: Measured and predicted discharges and corresponding errors for series A data 5-5
Table 5-3: Measured and predicted discharges and corresponding errors for series B data 5-6
Table 5-4: Measured and predicted discharges and corresponding errors for series C data 5-6

LIST OF SYMBOLS

Area of bed not occupied by form roughness elements	A_n
ASCE Task Force on Friction Factors in Open Channels coefficients	a, b, c
Average drag force per unit length	ΔF_D
Average flow velocity (Q/A)	V
Average roughness element height	H
Bed shear drag component	F_b
Bed slope	S_o
Cylinder (stem) plan density	Λ
Cylinder Reynolds number	Re_d
Cylinder spacing perpendicular to flow	B
Density of cylinder for pseudofluid model	ρ_s
Depth averaged cylinder drag	ΔF_{DH}
Depth-averaged velocity at a constricted section in the stem layer	V_c
Difference between upstream and downstream water levels (Afflux)	ΔD
Dimensionless cylinder diameter	d_*
Dimensionless cylinder diameter for pseudofluid model	d_*'
Discharge	Q
Downslope weight component of control volume of water	F_w
Drag coefficient for pseudofluid model	C_D'
Drag coefficient for the cylinder array	C_{Da}
Drag force	F_D
Empirical coefficient	α_0
Empirical coefficient	α_1
Energy slope	S
Equivalent roughness height	k_s
Factor for flow separation over which bed shear does not occur	A
Flow depth	D
Flow depth at i^{th} section	D_i

Fluid density	P
Form (stem) drag component	F_v
Form drag coefficient	C_D
Friction factor of the channel bed	f_b
Froude number	Fr
Froude number at the ith section	Fr_i
Gradient of the free surface	$\frac{d\eta}{dx}$
Gravitational acceleration	G
Gross cross sectional area (h x W)	A
Height above the flume bed level	Y
Height of control volume	M
Hydraulic radius	R
Kinematic viscosity of water	N
Length of control volume	K
Number of cylinders in unit plan area	N
Plan area covering the array of cylinders	A_p
Projected area of the form roughness elements in the flow direction	A_b
Relative density difference	Δ
Relative dynamic viscosity	μ_r
Resistance coefficient accounting for stem drag and bed shear	F_f
Reynolds number	Re
Reynolds number for cylinder array	Re_a
Reynolds number for pseudofluid model	$Re_d^{'}$
Roughness element/stem diameter	D
Shear Reynolds number	Re^*
Shear velocity	u_*
Spatially averaged velocity in stem layer	V_{cs}
Staggering pattern coefficient	Ξ
Stem area concentration	l^*

Surface area on which the bed shear stress acts	A_{bf}
Volume of water	Vol
Water density	P
Water viscosity	M
Wetted stem length	L
Width of channel/flume	W
Width of control volume	L

1 INTRODUCTION

The inconsideration of the actions we as humans potentially have on given water courses has resulted in the alteration of rivers' natural flows and consequently an often-adverse impact on the rivers' natural ecosystems. River management has been centered around the relationship between hydrology and the hydraulic response of the river under given conditions. Effective management and utilization of water-linked ecosystems requires the ability to predict biological responses to implement management actions. The growing need to predict the various biological impacts related to water management activities demands further understanding of the relationships between hydrological variability and river ecosystem integrity (Richter *et al*., 1997). Hydraulics provides the bridge between hydrology and the biological response of a river. The objective of this research is to gain a better understanding of flow resistance at a finer resolution than that previously provided by the typically used 1D models. "The results will have immediate relevance for low flow hydraulic analyses in environmental flow determinations and in river rehabilitation design involving the placement of boulders to create suitable habitat conditions" (James, 2012).

Flow resistance arises from the interaction between the water and the physical features of the river. Many forms of flow resistance have been identified but the most dominant are boundary shear resistance associated with grain roughness and form drag resistance associated with flow separation around large roughness elements and irregularities. The existing methods for modelling channels, such as Mannings, Chezy and Darcy-Weisbach equations, where the flow depth (D) is large in comprison to the average roughness height (H) of the bed ($D/H > 10$) and there are no large scale roughness elements ($D/H < 10$) are well established and reliable for obtaining "good enough"estimates of the stage discharge relationship for a given water course. These equations do not apply when form drag (through the flow depth) becomes a significant flow resistance contributor. When applying the conventional resistance equations, the depth average velocity is depth-dependent and the resistance coefficient remains relatively constant, however when resistance is applied through the flow depth the depth average velocity tends to a constant and

this consequently requires compensation in the conventional resistance equations using depth-dependent resistance coefficients (James, 2012). The existing methods for determining the flow characteristics of a channel with large scale roughness elements conventionally involves modifying the resistance coefficient of the established Mannings, Chezy and Darcy-Weisbach equations such that the resistance coefficient accounts for all the various resistance effects (termed a lumped coefficient).

The determination of these resistance coefficients is typically conducted by selecting one of the following methods: -

1. Selecting a coefficient value based on judgement of photographs of rivers with similar looking physical features and whose coefficient value has been determined through measurement (e.g. Hicks and Mason 1991);
2. Selecting coefficient values from tables of rivers with various qualitative physical feature descriptions, the values of which have been determined through measurement (e.g. Chow 1959);
3. Determining a coefficient value through direct site measurements or empirically determined resistance coefficients;
4. Accounting for the individual resistance contributions and lumping them together to obtain an overall resistance coefficient. This method is typically known as the SCS Method which was initially proposed by Cowan (1956).

These methods are useful but each of them has flaws and a degree of uncertainty in its application. The use of tabulated values and photographs is unreliable because the values of the resistance coefficient often vary significantly with flow condition. It is difficult to identify a representative value within the often wide range reported or to predict the direction and rate of change of a trend with flow depth or discharge (James, 2012).

The synthesis of form resistance and boundary shear resistance has been considered by many researchers for various objectives such as alluvial channel resistance determination, resistance of vegetated channels and the resistance of channels with

large scale roughness elements (e.g. Einstein and Barbarossa 1952, Shields and Gippel 1995, Petryk and Bosmajian 1975, Stone and Shen 2002). These have yielded promising results. James (2012) has developed the synthesis method for flow through emergent vegetation (originally proposed by Petryk and Bosmajian 1975) and extended it to the case of flow through large scale emergent roughness elements. The research is based on the momentum balance of the downslope weight component (driving force) of a volume of water balanced by the form drag and boundary shear resistance components (resisting forces).

The determination of the boundary shear resistance coefficient can be done using equations such as those presented by the ASCE Task Force on Friction Factors in Open Channels (1963) per given boundary flow condition. The form drag component is accounted for through the general drag equation, however, use of this equation requires knowledge of the drag coefficient (C_D). There exists a lot of research for the relationship between C_D and cylinder Reynolds number (Re_d) for an individual cylinder exposed to a uniform velocity gradient with a diameter much (d) smaller than the flow depth and considered to be infinitely long. Notably, Wieselsberger 1922, Finn 1953, and Tritton 1959 carried out wind tunnel experiments to determine these relationships. Little knowledge exists with regards to the drag coefficient for single and multiple emergent objects with a low aspect ratio ($D/H < 10$). The flow structure around the cylinder is complex and the free surface has a major influence on the drag force exerted on the object as the local water levels are raised and lowered on the upstream and downstream sides of the cylinder respectively. The flow around emergent objects even fascinated and baffled the brilliant Leonardo da Vinci as shown a couple of his drawings (Figure 1-1 and Figure 1-2). The scant research that has been conducted on drag coefficients for groups of objects has been concerned with vegetation stems which are thin and have high areal densities. The results of different researchers' investigations are not always in agreement. The reported C_D vs Re_d relationships by Kothyari *et al*. (2009) and Tanino & Nepf (2008) differ quite considerably in magnitude. Nepf (1999) also reported conflicting evidence to those of Ishikawa *et al*. (2000), James *et al*. (2004), Kothyari *et al*. (2009), and Cheng (2013). This goes to prove how complex the

determination of the drag coefficient is. A thorough empirical investigation is required to present a method (or multiple methods) which is simple in its application and better able to estimate the resistance of a water course with large scale roughness elements than existing methods.



Figure 1-1: Leonardo da Vinci's "Old man with water studies". (Reuteler, 1994)

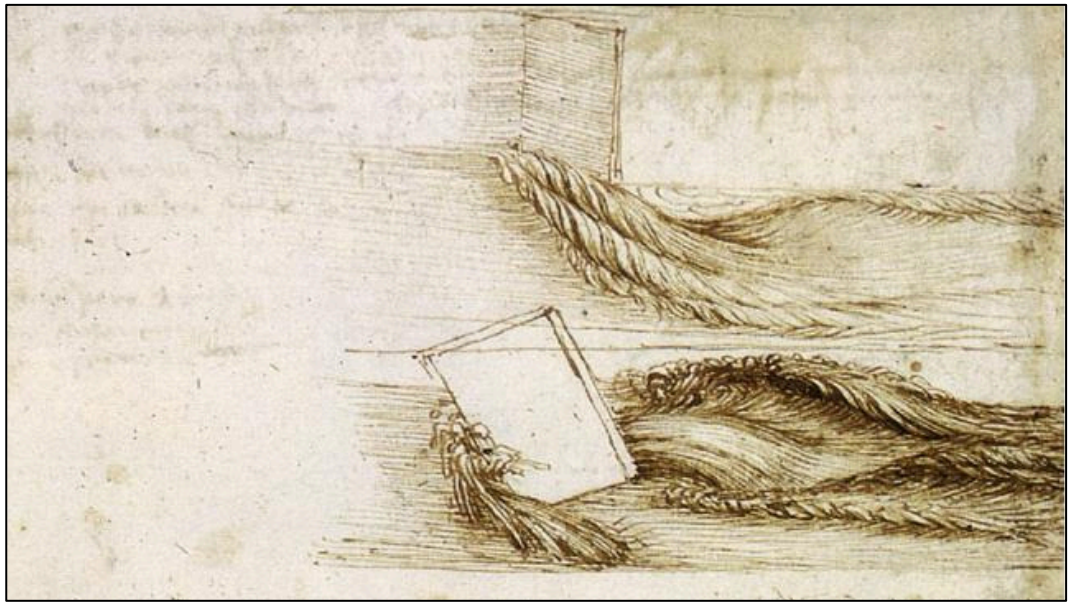

Figure 1-2: Leonardo da Vinci's "Studies of water passing obstacles". (Reuteler, 1994)

The objective of this research is to elucidate the major defining drag coefficient relationships and present effective methods for determining the drag coefficient under various flow conditions. This will be done by carrying out an experimental investigation on single as well as multiple cylinders arranges in different configurations and exposed to varied flow conditions. The resulting data is analysed and equations formulated which are intended to lay the groundworks for future research.

1.1 Layout of the thesis

The report is structured as follows: -

1. **Introduction:** A brief statement of the problem is presented and methods for its solution are presented.
2. **Background:** This chapter presents the existing knowledge in the field. Their research methodologies and outcomes are summarised. Gaps in the research are identified and hence the need for the current research is reinforced.
3. **Experimental investigation:** This chapter covers the research methodology adopted. An explanation is given for the apparatus used and developed during the study. The methods for calibrating the various equipment is covered. The approaches carried out for verifying the results obtained with the apparatus are presented and discussed. Finally, the experimental investigations carried out are discussed.
4. **Results:** The results of the calibration tests, verification tests and experimental investigations are presented. The results are discussed.
5. **Confirmation tests:** The results of the experimental investigations are used to make predictions which are compared to measured laboratory data extracted from a separate study by other researchers.
6. **Conclusions and Recommendations:** This chapter summarises the experimental investigation and the key findings. Recommendations are formulated for further research.

2 BACKGROUND

The determination of drag coefficients has been carried out by several researchers, the research carried out has concentrated on flexible and rigid and submerged and unsubmerged vegetation for various flow conditions. The following research has been identified as most relevant to the research to be carried out, background is also given as to why the drag coefficient is required.

Ranga Raju *et al.* (1983) carried out an experimental investigation to determine the effect of smooth, rigid, emergent cylinders with different blockage values (cylinder diameter (*d*) / cylinder centre to centre spacing (*B*) perpendicular to the flow direction) have on energy loss, afflux and the drag force when exposed to different flow conditions. Of primary concern was the afflux upstream of the cylinder. Ranga Raju *et al.* (1983) showed theoretically that the afflux and energy loss induced by the cylinder are functions of the drag characteristics of the cylinder. The determination of the drag coefficient is therefore required to accurately determine the magnitude of these phenomena. The experiments were carried out in a laboratory flume with smooth boundaries. Smooth cast iron cylinders were placed in a single row perpendicular to the flow with varying degrees of blockage. The central cylinder was fitted with a differential pressure transducer which was used to take pressure measurements vertically along the cylinder. Measurements were made at different angles to the flow by rotating the cylinder. The local drag force per unit length at any given elevation was determined by integrating the pressure distribution around the cylinder in the direction of average flow. The total drag force on the cylinder was obtained by summing the local drag forces.

Ranga Raju *et al.* (1983) found that the drag force exerted on a cylinder increases with increasing blockage. This suggests that the drag coefficient would increase with increasing blockage. The authors further stated that the drag coefficient is related to the Froude number and the ratio of the approach flow depth (10 cylinder diameters upstream) to the diameter of the cylinder. The researchers used the average flow velocity ($V = Q/A$ where "*Q"* is the discharge and *"A"* is the gross cross sectional area) in all their calculations at the appropriate sections. Ranga Raju

et al. (1983) also found that the local drag force per unit length (ΔF_D) close to the bed was low and varied highly but the variation became more gradual and tended towards a constant value towards the water surface. Figure 2-2 illustrates the variation of the drag force per unit length with height above the bed (y). Figure 2-1 illustrates the definitions for the various variables, S_o is the slope of the bed. In Figure 2-2, Fr_3 is the Froude number at section 3, y is the elevation above the bed (shown in Figure 2-1).

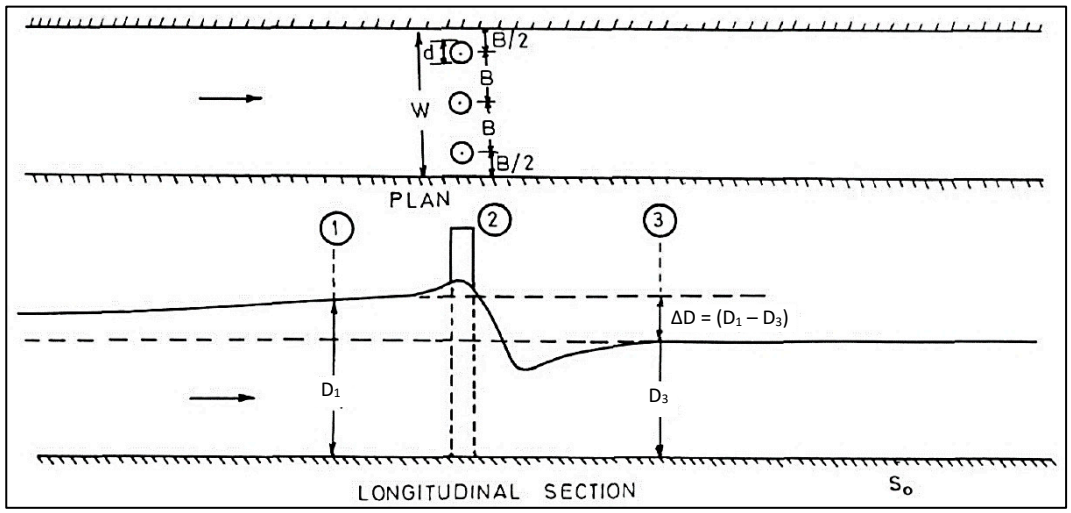

Figure 2-1: Description of the different experimental variables (Ranga Raju, et al., 1983).

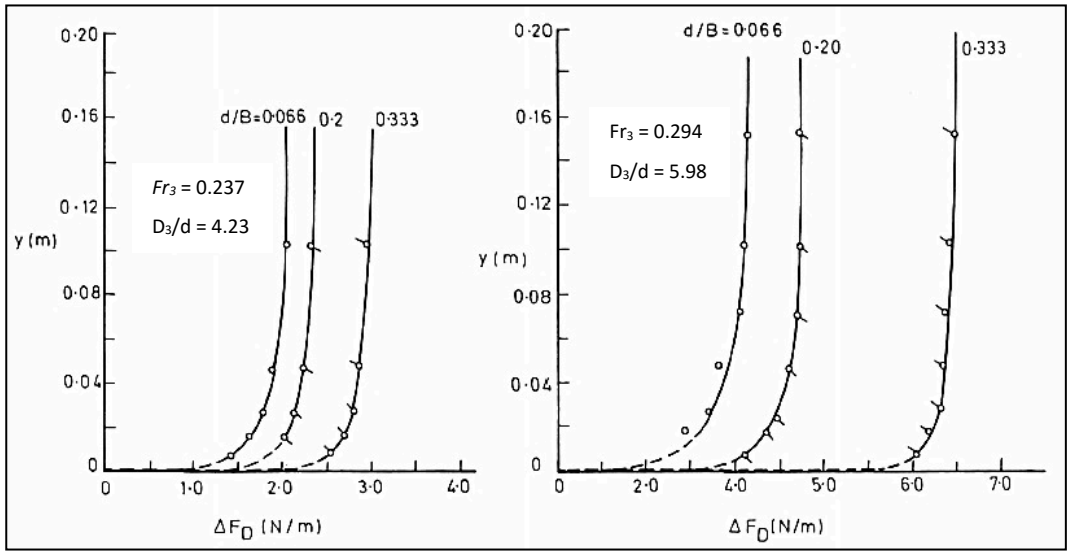

Figure 2-2: Variation of drag force with flow depth and the influence of blockage (d/B) on this relationship. The graph on the right is for a higher discharge and flow depth and therefore has a slightly higher Froude number than the left graph (Ranga Raju, et al., 1983).

Ishikawa *et al.* (2000) carried out an experimental investigation to determine the effect multiple riparian trees have on the drag exerted by a single tree on the river flow. The results of these experiments would then be used to improve bed load transport prediction methods. The experiments were conducted in a laboratory flume with steel rods used to model trees. Two different diameters of rods were used to obtain different areal densities, λ, equation (*2-1*) in separate tests, each type of rod was tested with two centre to centre spacing. Three bed slopes were used and three discharges were used for each slope.

$$\lambda = \frac{1}{A_p}\left(\frac{n\pi d^2}{4}\right) \tag{2-1}$$

where A_p = plan area covering the array of cylinders, n = number of cylinders in the plan area, d = stem diameter.

The general drag (equation (2-2)) was used to calculate the drag coefficient. Calculations were all done with the average flow velocity (V), where the flow depth was measured 4.5 m upstream of the test cylinder. The drag force experienced by a single cylinder was measured using apparatus constructed specifically for the experimental investigation. The apparatus isolates one of the metal rods. This rod is connected to an acrylic plate secured to a rigid platform traversing the width of the flume. Strain gauges were bonded to the acrylic plate (and calibrated) which allowed for the determination of the drag force as the rod and therefore plate deflected in the flow. Drag force measurements were taken at several locations within the array of rods, these values were then averaged to obtain the drag force for each test.

$$C_D = \frac{F_D}{\frac{1}{2}\,\rho\, d\, D V^2} \tag{2-2}$$

where F_D = drag force, ρ = density of water, d = cylinder/stem diameter D = flow depth and V = average flow velocity.

Ishikawa *et al.* (2000) found that C_D is highly dependent on the rod areal density, increasing with areal density (Figure 2-3). Experimental results also revealed; i) an

unclear relationship between C_D and Reynolds number, ii) a decrease of C_D with increasing Froude number (Figure 2-4) and iii) a slight correlation between C_D and the bed slope.

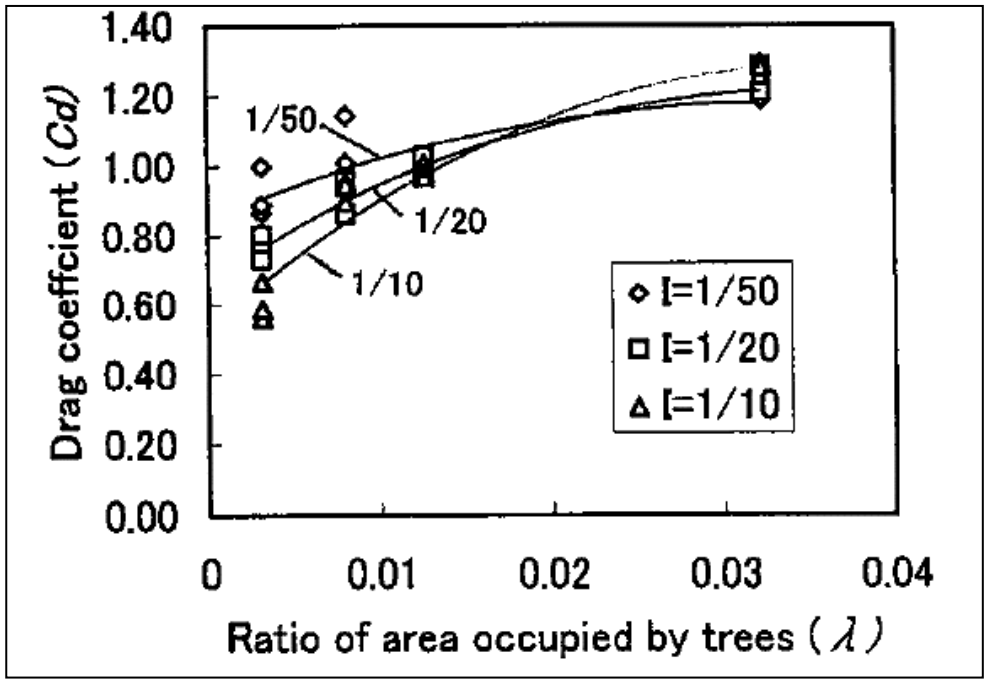

Figure 2-3: Relationship between drag coefficient and areal rod concentration. The different shape represents the different bed slopes as shown (Ishikawa, et al., 2000).

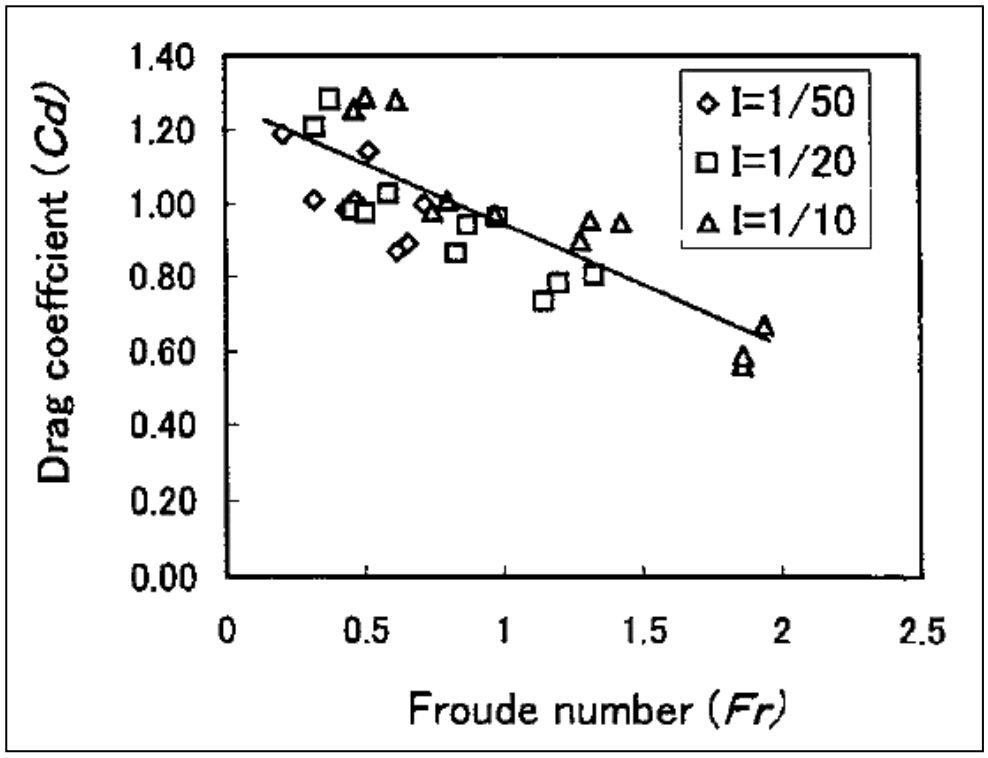

Figure 2-4: Relationship between drag coefficient and Froude number. (Ishikawa, et al., 2000).

Stone and Shen (2002) carried out an experimental investigation to determine the hydraulic resistance characteristics of a channel with vegetation and then to develop equations for the flow resistance and conveyance in these channels. The experiments were conducted in a laboratory flume using cylindrical elements (wooden dowels) under emergent and submerged conditions. The stem area concentrations (λ) tested were 6.10%, 2.20% and 0.55%, the diameter of the wooden dowels ranged from 3.18 to 12.70mm and were arranged in a regular staggered formation with centreline spacing ranging between 38 to 76mm. The discharge for each test was determined based on the pre-selected cylinder Reynolds number and the bed slope, the downstream weir was then adjusted to achieve the pre-selected degree of stem submergence. A magnetic-field velocity meter was used to measure the velocity profiles at predetermined locations within the cylinder array.

Stone and Shen (2002) developed resistance equations based on the momentum balance (equation 2-3) for a control volume of water occupying a unit bed area and extending from the bed to the water surface.

$$F_w = F_v + F_b \tag{2-3}$$

where the streamwise weight component, F_w, of the control volume is given by

$$F_w = \rho g S_o D(1 - \lambda l^*) \tag{2-4}$$

where S_o = bed slope, D = flow depth, λ = stem area concentration, ρ = water density, g = gravitational acceleration, l^* = degree of submergence (wetted stem length / flow depth), $l^* = 1$ for emergent conditions.

The stem induced drag, F_v, is given by the general drag equation rearranged:

$$F_v = \frac{1}{2}\rho C_D n d l V_c^2 \tag{2-5}$$

where ρ = water density, C_D = drag coefficient for a single cylinder in an array of identical cylinders, n = number of cylinders in unit plan area, d = stem diameter, l is the wetted stem length and V_c = depth-averaged velocity at a constricted section

Stone and Shen (2002) recommend the use of V_c rather than the average velocity as the C_D value calculated using V_c compared well with that of a single cylinder. The depth-averaged velocity at a constricted section in the stem layer is the velocity calculated considering the available volume for flow (equation (2-6)). The drag coefficient was reportedly only slightly affected for a wide range of λ, d, and cylinder Reynolds number (Re_d).

$$V_c = \frac{Q}{(W \times D) \times (1 - \lambda)} \tag{2-6}$$

where Q = discharge, W = width of the channel/flume, D = flow depth, λ = cylinder/stem concentration.

$$Re_d = \frac{Vd}{\nu} \tag{2-7}$$

where V = average velocity, d = cylinder/stem diameter, ν = kinematic viscosity of water.

The bed friction, F_b, per unit area is given by

$$F_b = \frac{\rho V^2 f_b}{8}(1 - \lambda) \tag{2-8}$$

where ρ = water density, f_b = friction factor of the channel bed, λ = cylinder/stem concentration and V = average velocity.

The relationship between V_c and V is given by

$$V = V_c \left[1 - \sqrt{\frac{4\lambda}{\pi}}\right] \tag{2-9}$$

Combining equations 2-4 -2-9, equation 2-3 can be written as

$$V = \sqrt{\frac{g(1 - \lambda l^*)}{\frac{f_b(1 - \lambda)}{8} + \left[\frac{2\,\lambda\, l^*\, D\, C_D}{\pi\, d\, \left(1 - \sqrt{4\lambda/\pi}\right)^2}\right]}}\sqrt{D\,S} \tag{2-10}$$

Equation 2-10 provides a conveyance expression for flow through emergent vegetation. In the absence of vegetation and where there is only boundary shear resistance acting, equation 2-10 reduces to equation 2-11 which is the conventional Darcy-Weisbach formula.

$$V = \sqrt{\frac{8\,g}{f_b}}\sqrt{D\,S} \tag{2-11}$$

where S = energy slope

Stone and Shen (2002) took cognisance of the fact that the drag coefficient for a cylinder amongst an array of cylinders may differ from that of an individual cylinder. Equation 2-10 was used to calculate drag coefficient values for each of the test conditions in this study as well as for data obtained from Fenzl (1962) and Tsujimoto and Kitamura (1990), these values were then averaged to obtain a single C_D value which was assumed to cover a range of stem sizes, densities and cylinder Reynolds numbers. This drag coefficient constant (C_D = 1.05) was then used for the development of further conveyance equations for submerged vegetation conditions. Stone and Shen (2002) verified the use of the C_D value by comparing velocity values calculated using C_D = 1.05 in equation 2-10 with experimentally measured velocity values, the results showed a generally close agreement.

Thompson *et al.* (2003) carried out an experimental investigation in to determine the effect of different shaped roughness elements on the form drag coefficient. The shapes tested were circular, rectangular, trapezoidal (square frustum in 3 dimensions) with the large base orientated at the flume floor and trapezoidal with the small base orientated at the flume floor. The experiments were conducted in a laboratory flume where the four different shaped roughness elements were individually tested for various discharges and flow depths in a horizontal and 1% bed slope. Drag forces were measured using apparatus developed specifically for the investigation, a calibrated load cell was used to measure the drag force being applied to the roughness element. Thompson *et al.* (2003) reported that the cylinder drag coefficients determined using the drag forces measured using the aforementioned apparatus is in close agreement with previously reported values from other researchers, thereby giving confidence to the measurements.

The results of the experimental investigation show that the drag coefficient is dependent on the shape of the roughness elements with sharp-edged elements resulting in higher drag coefficient values.

James *et al.* (2004) carried out an experimental investigation in to determine the influence of emergent vegetation on flow resistance. The results of the experimental investigation showed that the resistance coefficients (Manning's n in this case) increase dramatically with flow depth when vegetation is present and by increasing vegetation density the rate of change of the resistance coefficient became steeper (Figure 2-5). This highlights the unsuitability of the conventional resistance equations for use under emergent roughness conditions.

James *et al.* (2004) proposed using an equation which could be related to measurable vegetation characteristics. The equation is based on the balance of driving and resisting forces within the flow which consists of form drag resistance in addition to the conventional boundary shear resistance. The proposed equation (equation 2-12) is developed based on the understanding that the boundary shear resistance that would occur in a clear (no vegetation) channel is reduced by an

amount equal to the total from drag resistance divided by the plan area of flow. The form drag force is represented through the general drag equation.

$$V = \frac{1}{F_f}\sqrt{S} \tag{2-12}$$

where

$$F_f = \sqrt{\left(\frac{1 - \frac{n\,\pi\,d^2}{4}}{\frac{f_b}{8} + C_D\frac{1}{2}\,n\,D\,d}\right) g\,D}$$

Theoretical values for F_f were calculated and compared with those determined experimentally, the results are shown in Figure 2-6 with the theoretical predictions plotted as the dashed lines. Figure 2-6 shows that although the predictions aren't very accurate in magnitude the theoretical trend follows the trend of the experimental results correctly. James *et al.* (2004) suggests that the reason for the relatively large errors in magnitude between experimental and theoretical values comes down to the uncertainty in using C_D values determined from the standard relationship for an infinitely long, individual cylinder (as presented by Albertson *et al.* 1960) to a group of stems where local velocities will be considerably higher than the average approach velocity and additional drag associated with surface distortion at low flow depths will become significant.

Table 1: Experimental conditions (James, et al., 2004)

Test	λ (%)	Stem type	Bed slope	Discharge (l/s)
A1	–	–	0.002	0.963–0.859
A2	3.14	Round (5 mm)	0.010	0.125–1.642
A3	3.14	Round (5 mm)	0.002	0.126–0.726
A4	0.79	Round (5 mm)	0.002	0.164–1.986
A5	0.35	Round (5 mm)	0.002	0.306–2.073
B1	–	–	0.0022	6.00–19.70
B2	0.82	Round (10 mm)	0.002	8.56–16.11
B3	1.52	Round (10 mm)	0.002	6.42–10.92
B4	2.45	Round (10 mm)	0.002	4.60–8.59

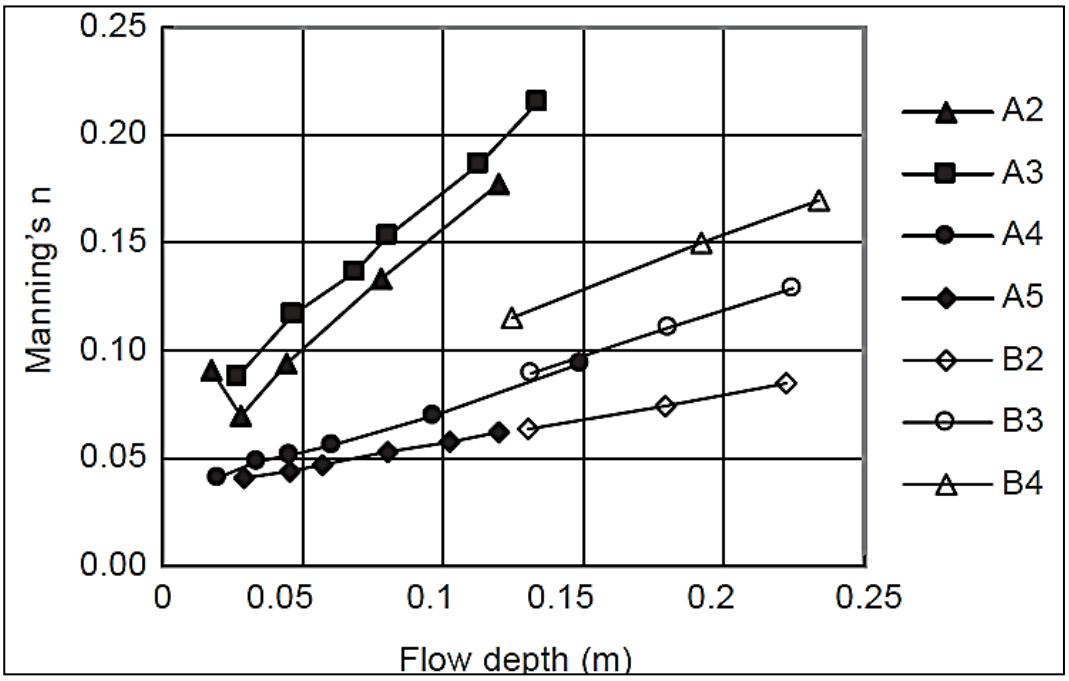

Figure 2-5: Effect of flow depth and stem density on Manning's n. (James, et al., 2004).

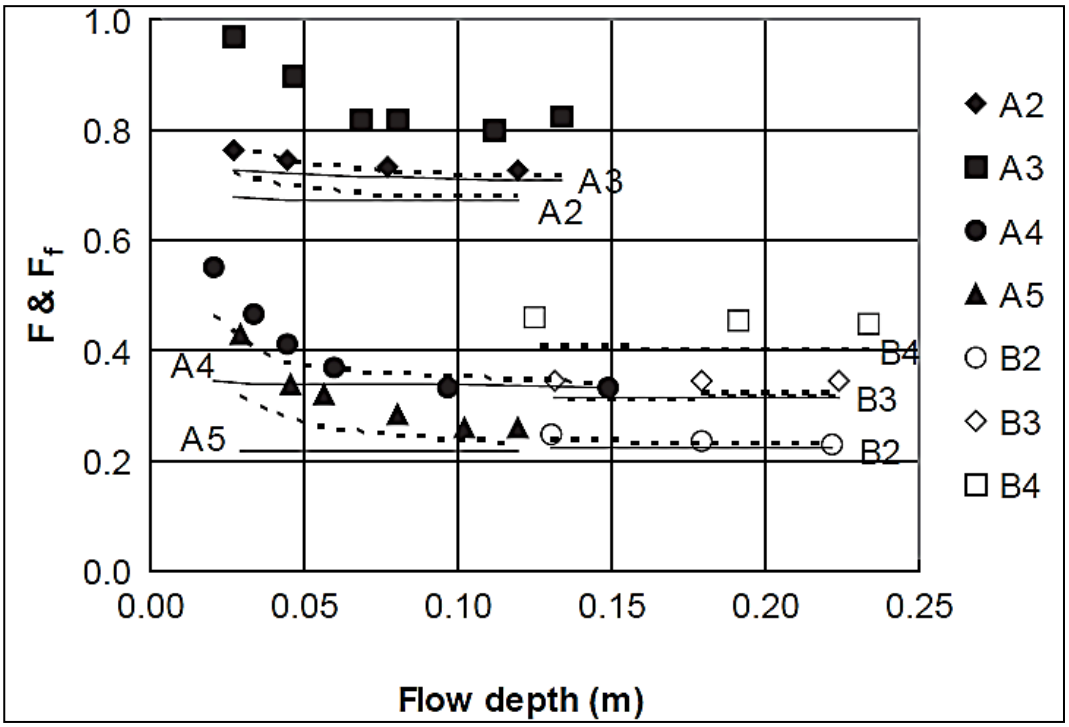

Figure 2-6: Measured and predicted values of F_f for round stems. The solid lines represent calculated F values and the broken lines represent calculated F_f values. (James, et al., 2004).

Tanino and Nepf (2008) carried out an experimental investigation to determine the drag effect of randomly distributed rigid, emergent cylinders. The experiments were carried out in in two laboratory flumes with different dimensions, a wider flume

was used for sparse areal cylinder densities and the narrower flume was used for the dense areal cylinder densities. Wooden dowels of uniform diameter were used to model the vegetation. The dowels were arranged in random configurations in the flume to obtain predetermined cylinder densities.

Tanino and Nepf's (2008) research is based around the general drag equation as well as equation 2-13 proposed by Ergun (1952) which states that the relationship between the normalized drag and cylinder Reynolds number is linear, the slope of the line is given by a constant (α_1) and the y-intercept is given by a variable which is a function of the cylinder density (α_0). Measurements of the change in water surface elevation induced by the cylinders were taken and substituted into the theoretically derived equations 2-14 and 2-15 to determine the total cylinder drag (per unit volume of array) and the drag coefficient, C_D, respectively. The normalized drag for each cylinder density is plotted against the cylinder Reynolds number as shown in Figure 2-7, the plot confirms the linear relationship proposed by Ergun (1952) as well as the differing line slopes for the different cylinder concentrations.

$$\frac{\Delta F_D}{\mu V_{cs}} = \alpha_0 + \alpha_1 Re_d \tag{2-13}$$

where ΔF_D = average drag per unit length, V_{cs} = depth-averaged velocity at a constricted section in the stem layer, Re_d = cylinder Reynolds number, μ = viscosity.

$$\Delta F_{DH}\, n = -(1 - \lambda)\rho g \frac{d\eta}{dx} \tag{2-14}$$

where ΔF_{DH} = depth averaged cylinder drag, n = number of cylinders per unit bed area, $\frac{d\eta}{dx}$ = gradient of the free surface, λ = solid volume fraction, ρ = density, g = acceleration due to gravity.

$$\frac{C_D V_c^2}{2} nd = -(1 - \lambda) g \frac{d\eta}{dx} \tag{2-15}$$

where V_c = depth averaged velocity

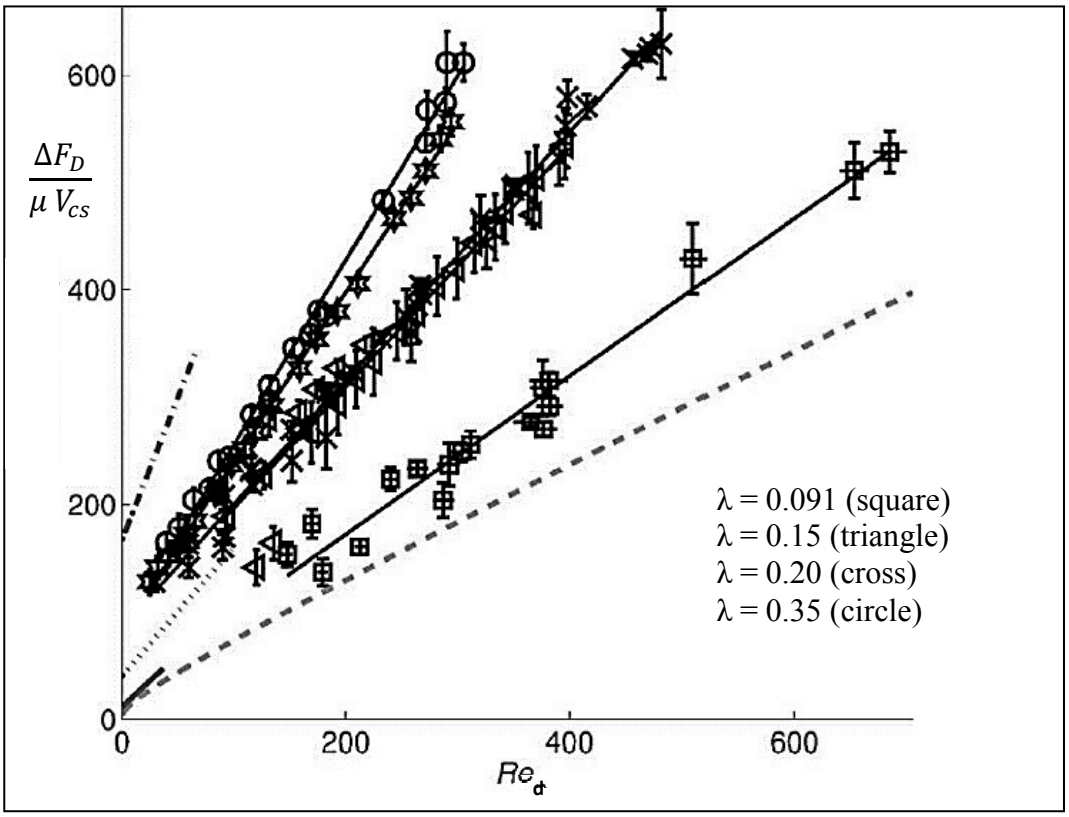

Figure 2-7: Relationship between the normalized drag and cylinder Reynolds number. Solid lines mark the linear regression for each λ. Grey lines represent Koch and Ladd's (1997) numerical results at λ = 0.05 (solid line), 0.2 (dotted line), and 0.4 (dash-dotted line). (Tanino & Nepf, 2008).

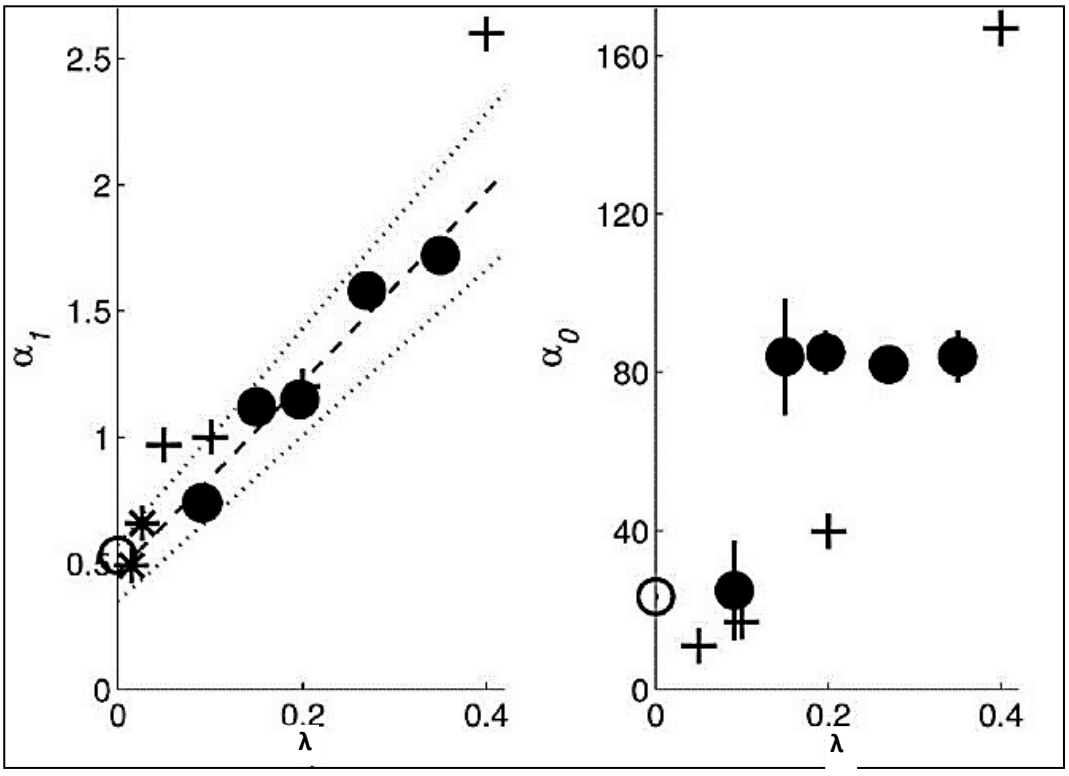

Figure 2-8: Relationship between α_0, α_1 and cylinder areal concentration. (Tanino & Nepf, 2008).

$$\alpha_1 = (0.46 \pm 0.11) + (3.8 \pm 0.5)\lambda \quad (2\text{-}16)$$

Tanino and Nepf (2008) presented Figure 2-8 and equation 2-16 for determining α_0 and α_1 and therefore C_D and the drag force for a given cylinder density using equations 2-17 and 2-13 respectively, it is noted that these results would only be valid for $O(30) \leq Re_d \leq O(700)$.

$$C_D = 2\left(\frac{\alpha_0}{Re_d} + \alpha_1\right) \quad (2\text{-}17)$$

Tanino and Nepf (2008) concluded that the drag coefficient is highly dependent on the areal concentration of cylinders, they also showed that C_D decreases with increasing cylinder Reynolds number (Figure 2-9).

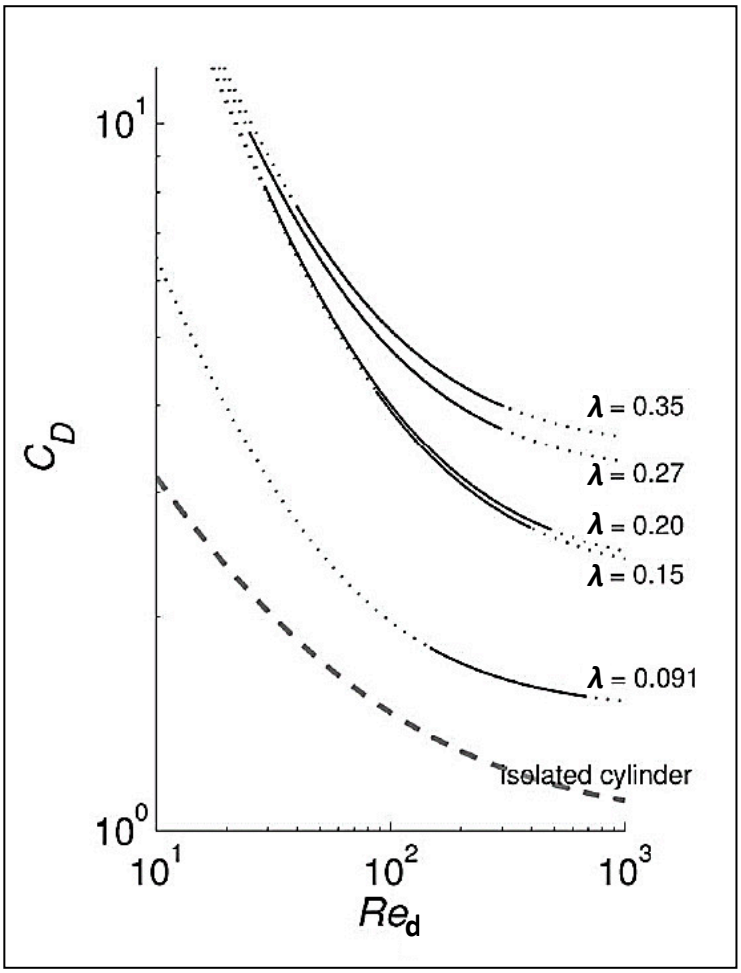

Figure 2-9: Relationship between the drag coefficient and cylinder Reynolds number for various cylinder concentrations. (Tanino & Nepf, 2008).

Kothyari *et al.* (2009) carried out an experimental investigation to determine the relationships between varying stem densities, cylinder Reynolds numbers (Re_d) and Froude numbers (Fr) on the drag coefficient. By considering the individual flow resistance components and isolating the flow resistance induced by the bed material, Kothyari *et al's.* (2009) goal was to determine the effect of varying vegetation densities on sediment transport. The research was carried out in a flume by passing water at various discharges and at varying flume slopes through an array of emergent 10 mm diameter stainless steel circular cylinders arranged in a regular staggered pattern (forming equilateral triangles). An isolated cylinder placed in the centre of the array was connected to a cantilever strain gauge which was secured above the flume to allow for the measurement of the drag force applied by the flowing water onto the cylinder. The areal densities of cylinders ranged from 0.22% to 8.85% and the bed slopes were 0, 1/100 and 1/50. For each density-slope combination discharges of 0.03 m^3/s and 0.072 m^3/s were used. The flow depth was incrementally adjusted between 0.1 m and 0.38 m. The flow regime during all the experiments remained subcritical with the Froude number ranging from 0.1 to 0.8.

The drag coefficient C_D was determined based on the general drag equation (equation (2-2)). The depth-averaged velocity (V_c) was used instead of the average velocity.

Kothyari *et al.* (2009) consider the total flow resistance to be a combination of form drag (vegetation) resistance and boundary shear (grain) resistance. The total resistance equilibrates the streamwise weight component of a control volume of water of unit length and extending from the bed level to the water surface minus the volume of water occupied by the stems.

Kothyari *et al.* (2009) plotted the variation of F_D with V_c^2 as shown in Figure 2-10, which illustrates a generally linear relationship as expected and in agreement with equation (2-2). The deviation from linearity was attributed to the effect of Reynolds number and therefore the influence of Reynolds number on C_D. Kothyari *et al.* (2009) also presented Figure 2-11 which illustrates the variation of C_D with Re_d and λ, it is clear that as stem densities increase so does the value of C_D, the graph also

shows the marginal effect of Reynolds number on C_D with the majority of variation occurring at low Re_d values and tending to a constant trend for high Re_d values. Kothyari *et al.* (2009) presented the following equation for C_D in subcritical flows and a triangular staggering pattern

$$C_D = 1.53[1 + 0.45\ln(1 + 100\lambda)]Re_d^{-3/50} \tag{2-18}$$

Kothyari *et al.* (2009) explains that the reason for the logarithmic expression is due to the large increase of C_D values at low stem densities whereas at high stem densities the C_D value tends to a constant, they also note that the C_D value depends only marginally on Re_d but should nevertheless be included for more accurate results. Equation (2-18) is valid for isolated stems and was able to predict C_D values to a maximum error of ±10% for most of the data in the given study.

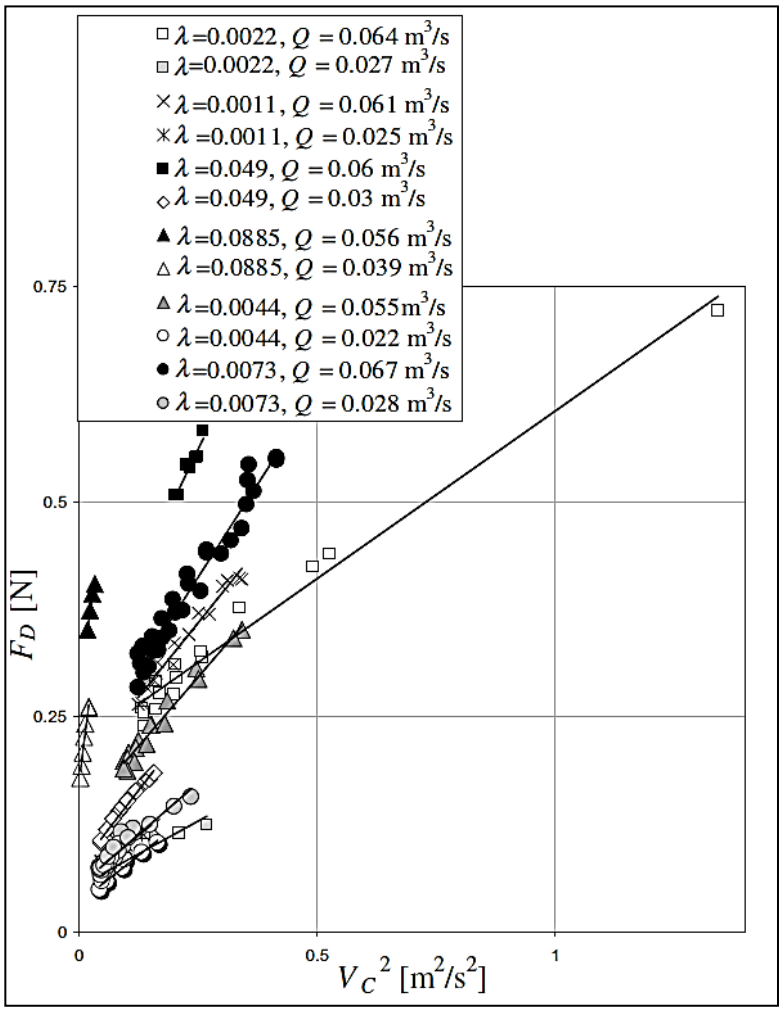

Figure 2-10: Variation of F_D with V_c^2 (Kothyari, et al., 2009).

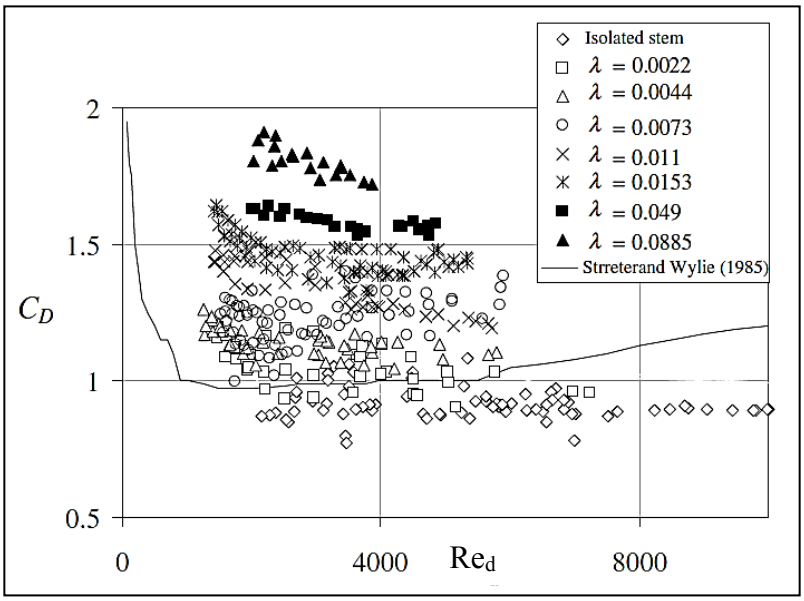

Figure 2-11: Variation of C_D with R_d and λ (Kothyari, et al., 2009).

Kothyari *et al.* (2009) went on to investigate the relationship between the Froude number and C_D, it was found that C_D remains constant for subcritical flows and moderate stem densities which confirms observations made by Kouwen and Fathi-Moghadam (2000). For very high stem densities the value of C_D decreases as Fr increases towards 1.0, however Kothyari *et al.* (2009) points out that these stem densities would be unlikely to occur in the natural environment. Kothyari *et al.* (2009) used the data of Ishikawa *et al.* (2000) to investigate the variation of C_D with Fr under supercritical flows, the results showed that the value of C_D decreases with increasing Fr, the given explanation for this trend is due to the non-uniform averaged vertical velocity distribution through the stems which is proposed to be caused by air entrainment in the flow. Kothyari *et al.* (2009) modifies equation (2-18) to equation 2-19 to account for the different flow conditions as well as for the staggering pattern (ξ), $\xi = 1.0$ for a triangular staggering pattern and $\xi = 0.8$ for a regular-square staggering pattern.

$$C_D = 1.8\xi Re_d^{-3/50}[1 + 0.45\ln(1 + 100\lambda)] \times (0.8 + 0.2Fr - 0.15Fr^2) \qquad (2\text{-}19)$$

Equation 2-19 predicts C_D values for the given investigation and for Ishikawa *et al.* (2000) data to within a maximum error of ±10% for most the data and predicts the maximum errors for data of Thompson *et al.* (2003) to within ±20% for most the

data which was considered satisfactory due to the associated uncertainties involved in the measurement techniques.

Stoesser *et al.* (2010) carried out a series of large-eddy simulations (LES) to determine the applicability of the simulation to flow through an array of emergent, rigid cylinders. The simulation was run for three cylinder densities at two Reynolds number values. Existing experimental results by Tanino and Nepf (2008) and Liu *et al*. (2008) were used to validate the simulations, the results of the comparison between experimental results and the results of the simulation lined up well.

Stoesser *et al.* (2010) considers flow resistance to be a combination of boundary shear drag and form drag, form drag being further decomposed into contributions from the pressure difference between the upstream and downstream sides of the cylinder and viscous shear around the surface of the cylinder. Figure 2-12 was presented and shows the contributions of these three resistance manifestations for different cylinder concentrations and cylinder Reynolds numbers as presented through the simulation. Figure 2-12 shows the minor contribution of bed shear to flow resistance especially where there are high cylinder concentrations, it is also clear that the pressure drag is dominant under all conditions but becomes even more dominant with increasing cylinder concentrations and Reynolds number.

Stoesser *et al.* (2010) found that for sparse cylinder arrangements (10 cylinder diameters between cylinder centres in the flow direction) the flow around the cylinders behave in a similar manner to flow around an isolated cylinder at the Reynolds numbers simulated (squares on Figure 2-14), this indicates that the wake region from the upstream cylinder has dissipated and therefore there is no eddy-cylinder interaction with the downstream cylinder.

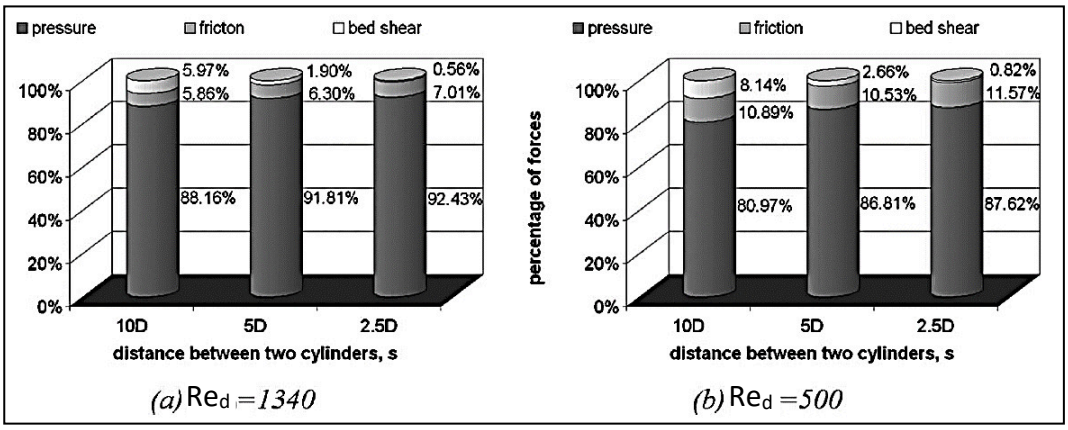

Figure 2-12: Contributions of pressure drag, friction drag, and bed shear to the total energy loss in flow through various cylinder densities and Reynolds numbers. (Stoesser, et al., 2010).

The normalised drag force for the simulation was calculated and plotted along with the results of Tanino and Nepf's (2008) experimental investigation (Figure 2-13), the trend of the lines is noted to match that of the experimental results well. The simulation predicted (LES) drag coefficient values are in close agreement with the experimental results of Tanino and Nepf (2008) as shown in Figure 2-14 . Stoesser *et al.* (2010) concludes that the drag coefficient is a function of cylinder Reynolds number, at least for cylinder Reynolds numbers below 10^3, however cylinder density has a greater influence and the trend seems to be linear (doubling density doubles the drag coefficient).

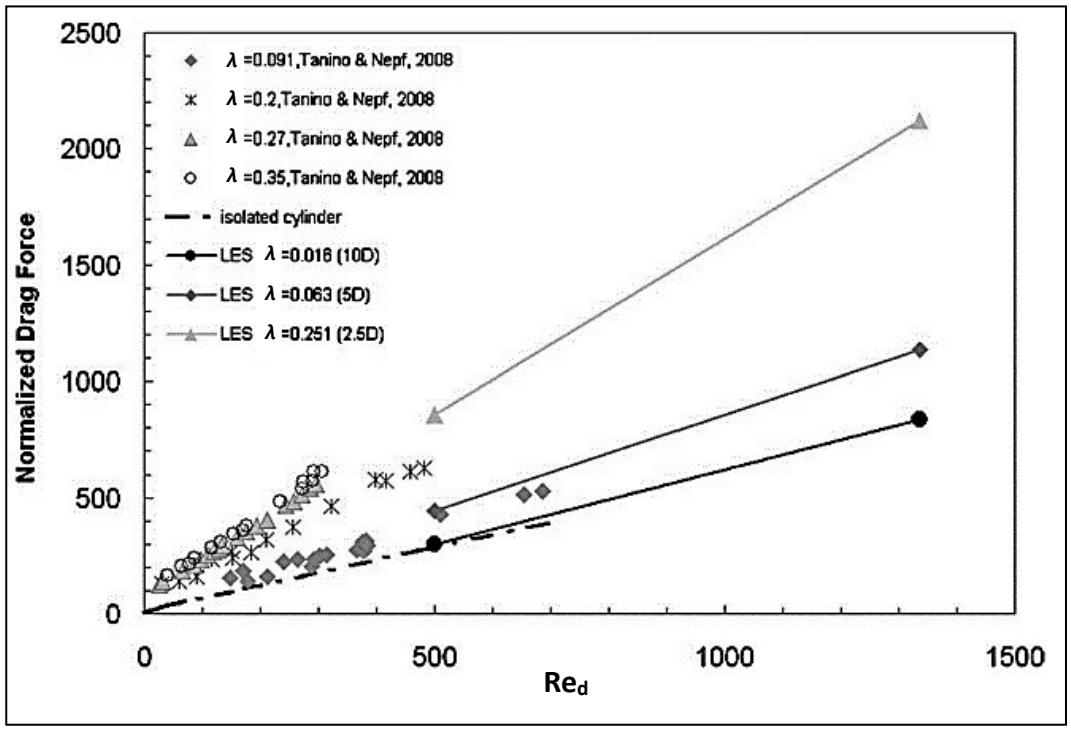

Figure 2-13: Normalized drag force as a function of cylinder Reynolds number for various cylinder densities. (Stoesser, et al., 2010).

Cheng (2013) carried out a study into extending the well-established curve of the drag coefficient vs Reynolds number for a single, isolated, infinite cylinder (Figure 2-16, equation (2-20) to the case of a cylinder amongst multiple cylinders in an open channel. Cheng (2013) made an analogy between water passing through an array of cylinders in a channel and an identical array of cylinders settling in a stationary pseudofluid with the same velocity as the water flowing in the channel.

$$C_D = 11Re_d^{-0.75} + 0.9\left[1 - exp\left(-\frac{1000}{Re_d}\right)\right] + 1.2\left[1 - exp\left(-\left(\frac{Re_d}{4500}\right)^{0.7}\right)\right] \quad (2\text{-}20)$$

Equation (2-20) represents several data sets and is valid for $0.02 \leq Re_d \leq 2 \times 10^5$.

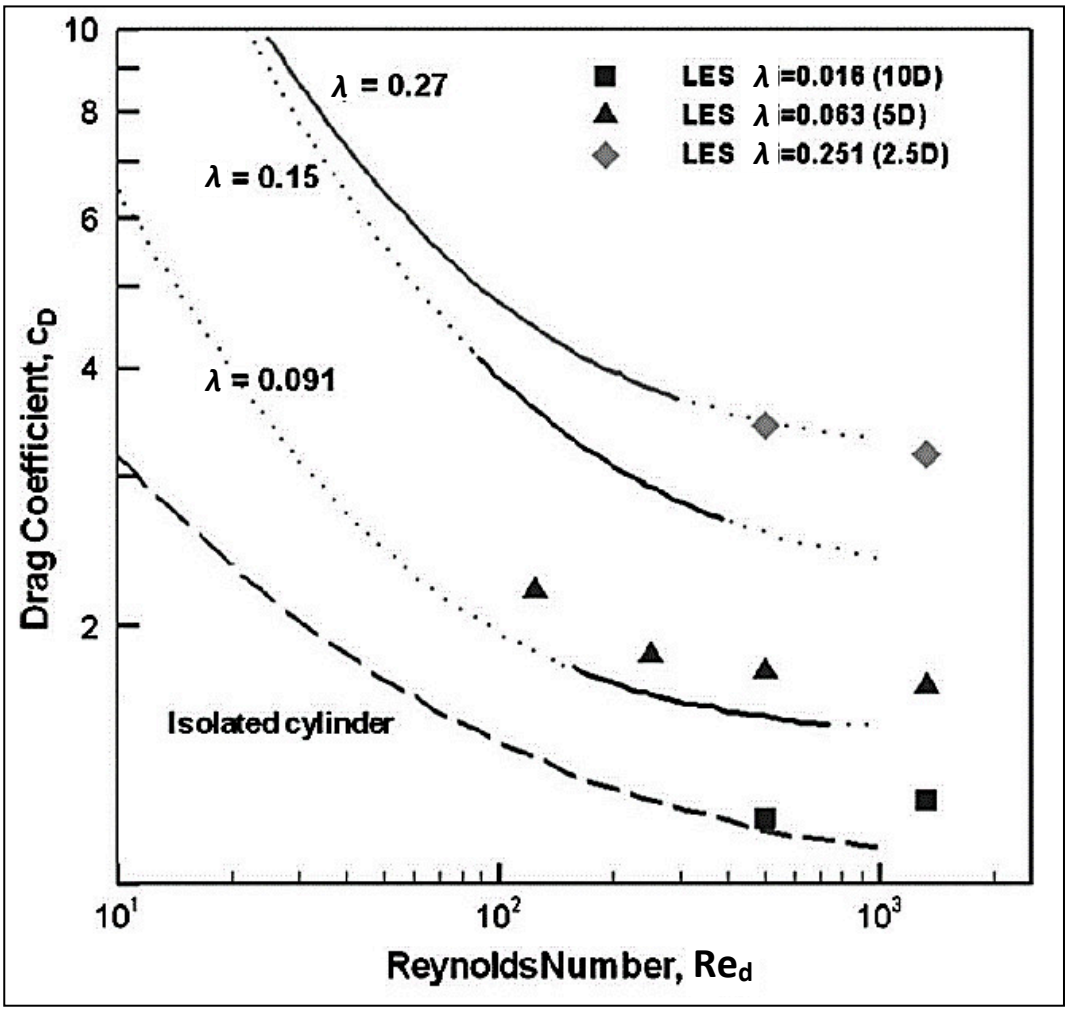

Figure 2-14: Drag coefficient C_D as a function of cylinder Reynolds number for various cylinder densities (lines represent data of Tanino and Nepf 2008). (Stoesser, et al., 2010).

The driving force in the case of a control volume of water moving in a sloped open channel is the streamwise weight component of the volume which is quantified in terms of the energy slope. The driving force in the case of cylinders settling in a fluid is the density difference between the cylinders and the fluid. Cheng (2013) assumes that the form drag is dominant and all other resistance contributions are negligible. The density difference is not a physically applicable parameter for vegetated open channel flows and therefore is expressed in terms of the energy slope given by equation (2-21).

$$\Delta = \frac{S}{\lambda} \tag{2-21}$$

where Δ is the relative density difference, S is the energy slope and λ is the cylinder density

Equation (2-21) connects the open channel flow scenario with the settling scenario by providing a relationship between the two forms of driving force and allows for the development of the pseudofluid model. Cheng (2013) formulated equation (2-21 using the following approach which considers two scenarios. The first scenario is an open channel flow through a rigid array of cylinders, the second scenario involves the settlement of the same array of cylinders in a pseudofluid which allows the cylinders to settle at a rate which is equal to the flow velocity of the first scenario.

For the first scenario ("A" in Figure 2-15), if the drag coefficient is known for the cylinder array (C_{Da}), the average drag per unit length of the cylinder is given by:

$$F_{Da} = \frac{1}{2} C_{Da} \rho d V_c^2 \tag{2-22}$$

Where the subscript a is used to denote the parameters related to the cylinder array. C_{Da} tends to C_D as λ becomes small. If a control volume is considered with n cylinders contained in it (Figure 2-15), then the average drag for a cylinder per unit length is equal to the corresponding streamwise component of the gravity of the fluid (Cheng & Chiew, 1999), i.e.,

$$F_{Da} = \frac{KLM\rho g S}{nZ} = \frac{\pi d^2 \rho g S}{4\lambda} \tag{2-23}$$

where KLM = control volume dimensions (Figure 2-15), $n = KL\lambda/(\pi d^2/4)$

In equation (2-23) the form drag is considered dominant while bed friction, sidewall friction and free surface effects are considered negligible. This effectively means the energy slope (S) is solely associated with the energy loss caused by the cylinders. Combining equations (2-22) and (2-23) gives:

$$C_{Da} = \frac{\pi g d S}{2\lambda V_c^2} \tag{2-24}$$

For the second scenario ("B" in Figure 2-15), the cylinder size, spacing and relative velocity for both scenarios can be considered equivalent. The second scenario is however imaginary and cannot be carried out experimentally, whereas scenario 1 is frequently carried out. For the control volume shown in Figure 2-15, the induced drag per unit length is equal to its effective weight:

$$F_{Da} = \frac{\pi d^2}{4}(\rho_s - \rho)g = \frac{\pi d^2}{4}\Delta\rho g \tag{2-25}$$

It can be seen from the above equation that the drag is proportional to the density difference and it is therefore the density difference that is the driving force for settling the cylinder. This is similar to the first scenario where the energy slope is the driving force in exerting drag onto the cylinders.

Therefore, combining equations (2-23) and (2-25) gives:

$$C_{Da} = \frac{\pi \Delta g d}{2V_c^2} \tag{2-26}$$

This simplifies to equation (2-21).

The pseudofluid model is based on the settling of sediment particles in a fluid whereby the clear fluid is considered to be a new fluid once multiple sediment particles are added. The new fluid has a different (apparent) density and viscosity to that of the clear fluid, these fluid properties being dependent on the concentration of sediment. This concept is adapted and applied to the scenario of fluid flowing in a channel with various concentrations of cylinders. Cheng (2013) first defined a dimensionless cylinder diameter, d_*, which was related to the C_D value of a single cylinder in a similar form to equation (2-20) (equation 2-27).

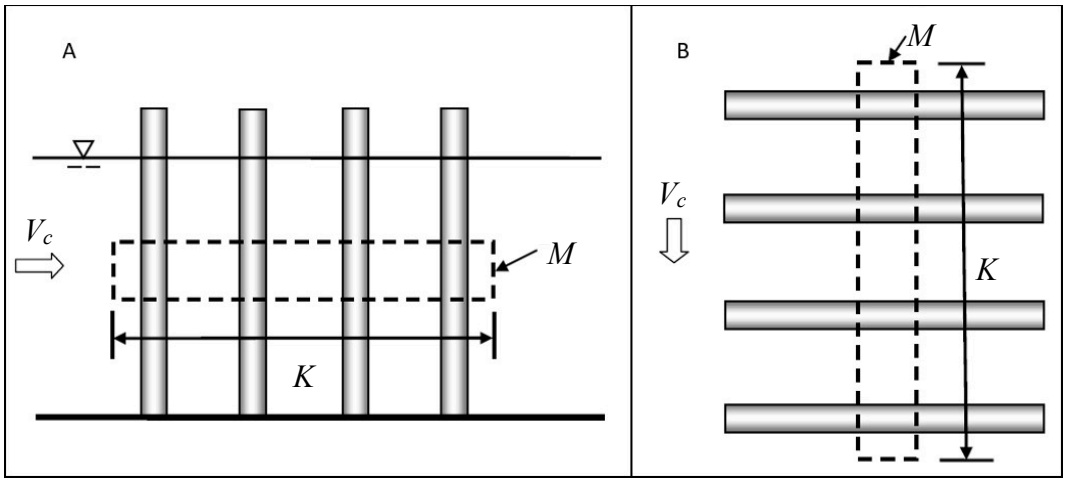

Figure 2-15: Two scenarios proposed by Cheng (2013). Dashed lines show control volume.

$$C_D = 35d_*^{-1.75} + 1.15\left[1 - exp\left(-\frac{80}{d_*}\right)\right] + 1.2\left[1 - exp\left(-\frac{d_*}{330}\right)\right] \qquad (2\text{-}27)$$

where $d_* = \left(\frac{2}{\pi} C_D Re_d^2\right)^{1/3} = \left(\frac{\Delta g}{\nu^2}\right)^{1/3} d$

Equation (2-27) is assumed to hold for the case of multiple cylinders provided the apparent density and viscosity are used. This results in equation (2-28).

$$C_D' = 35d_*'^{-1.75} + 1.15\left[1 - exp\left(-\frac{80}{d_*'}\right)\right] + 1.2\left[1 - exp\left(-\frac{d_*'}{330}\right)\right] \qquad (2\text{-}28)$$

where $d_*' = \left(\frac{(1-\lambda)(1+S)S}{\lambda} \frac{g}{\mu_r^2 \nu^2}\right)^{1/3} d$

For a given slope (S), areal cylinder density (λ), cylinder diameter (d), dynamic viscosity (ν) and experimentally calibrated apparent dynamic viscosity (μ_r), d_* can be calculated. Then, C_D' can be calculated using equation 2-28 and the average flow velocity through the cylinders, V_c, can be calculated using equation 2-29. Cheng (2013) recommended using equation 2-30 for the determination of μ_r with $\alpha = 80$ as it compared best with the measured velocities as shown in Figure 2-17. Except for one set of data, equations 2-28 - 2-30 predict the average velocity between the cylinders with a maximum error of 13.7%. Cheng (2013) found that the predictions were not sensitive to the selection of cylinder diameter.

$$V_c = \sqrt{\frac{\pi}{2}\frac{(1-\lambda)S}{\lambda + \lambda S}\frac{dg}{C_D'}} \tag{2-29}$$

$$\mu_r = 1 + \alpha\lambda \tag{2-30}$$

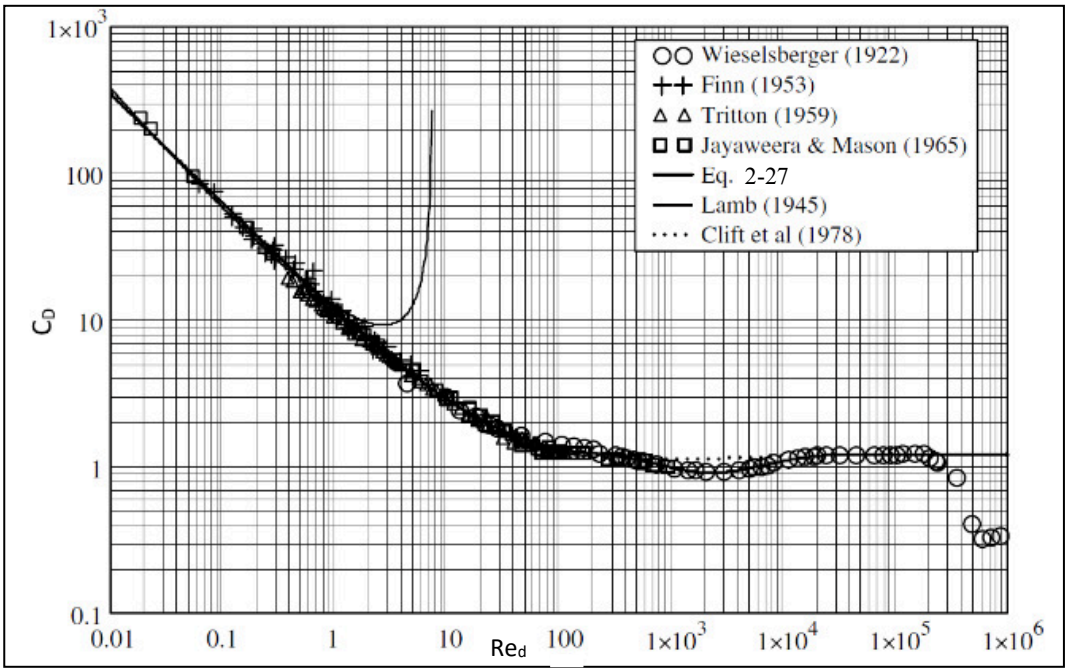

Figure 2-16: Variation of drag coefficient with cylinder Reynolds number for a single isolated cylinder in open channel flow (Cheng, 2013).

Figure 2-18 shows the variation of C_D with cylinder Reynolds number and areal cylinder densities, λ. The plotted curves show the considerable effect of increasing cylinder concentrations on the drag coefficient especially at low cylinder Reynolds numbers. The curves correctly approach the curve for a single cylinder (solid bold line) with decreasing λ. The curves follow the trends of the experimental data well as can be seen for the data of Tanino and Nepf (2008) whose experiments were carried out for λ = 0.15 - 0.35, the curves of λ = 0.1 and λ = 0.4 confine Tanino and Nepf (2008) data points well.

Cheng (2013) presented a generalized drag coefficient equation (equation 2-32) and Reynolds number equation (equation 2-31) for flow through arrays of circular cylinders with various concentrations, these equations can be applied in the same manner as equation (2-28) is applied for isolated cylinders

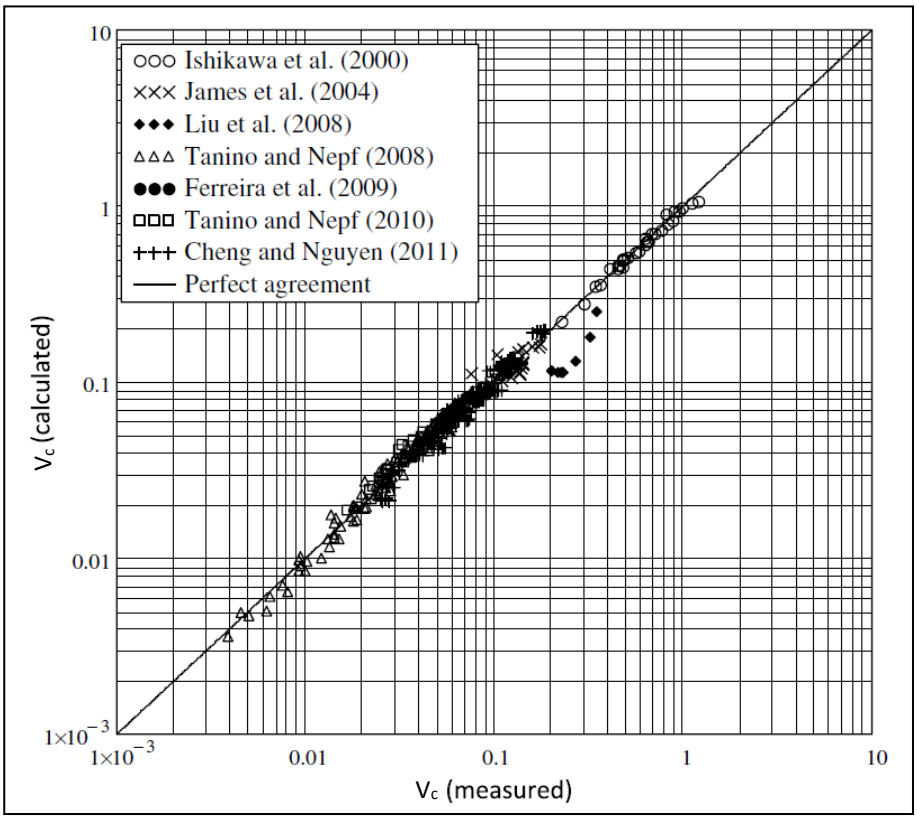

Figure 2-17: Comparison of calculated and measured average velocities through cylindrical stems (Cheng, 2013).

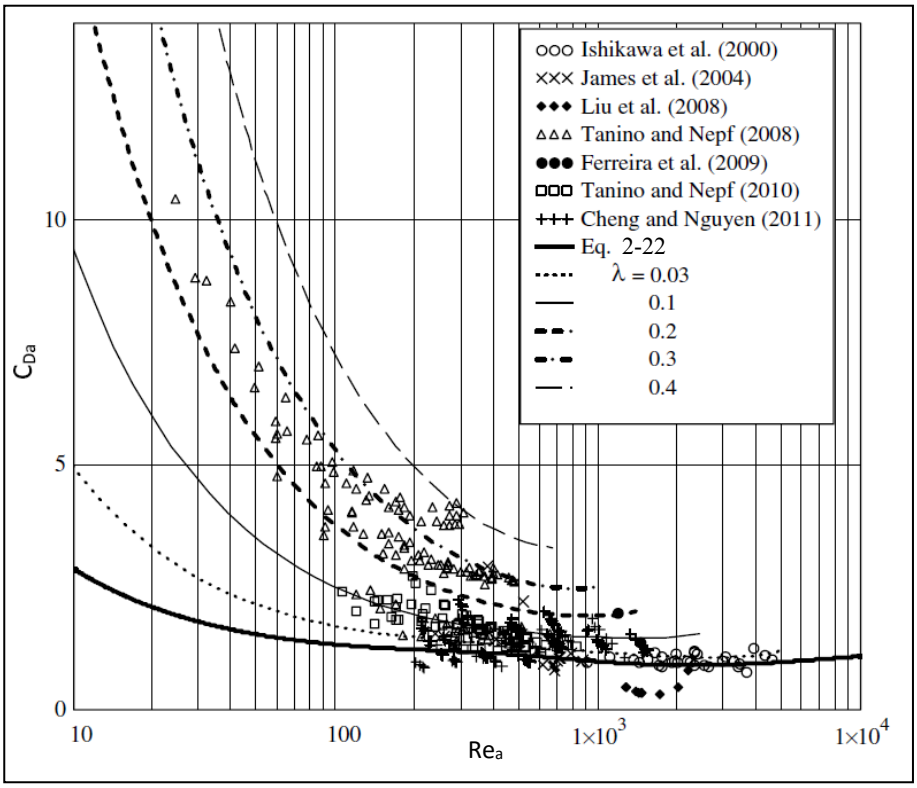

Figure 2-18: Variations of drag coefficient with Reynolds number and cylinder concentrations (Cheng, 2013).

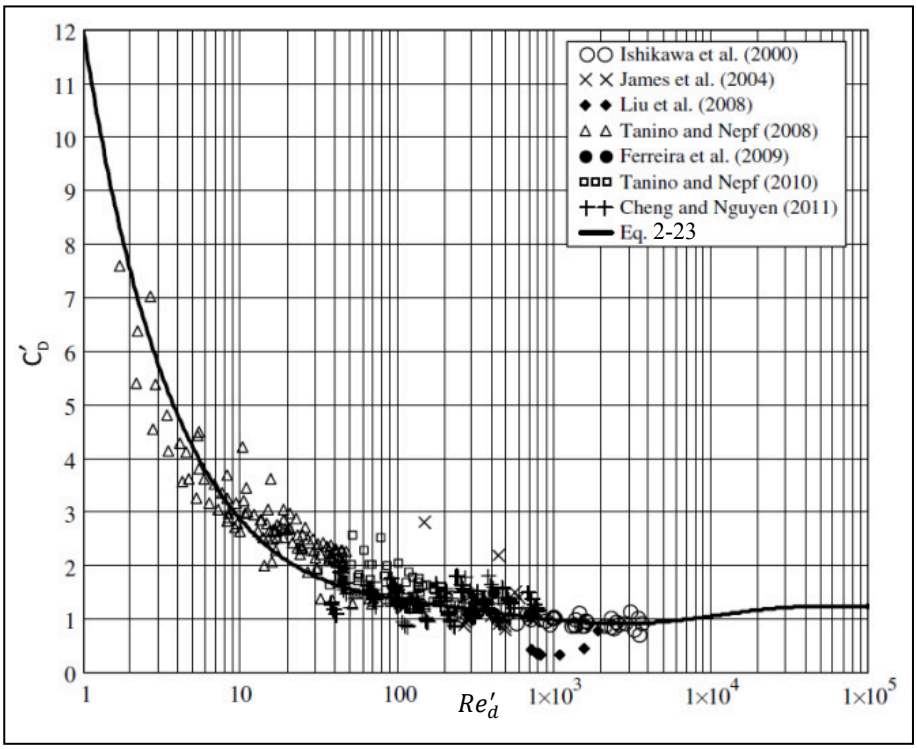

Figure 2-19: Generalized relationship between drag coefficient and Reynolds number for different cylinder configurations (Cheng, 2013).

$$Re_d' = \frac{1+S}{1+80\lambda} Re_a \tag{2-31}$$

where $Re_a = \frac{V_c\, d}{\nu}$

$$C_D' = 11Re_d'^{-0.75} + 0.9\left[1 - exp\left(-\frac{1000}{Re_d'}\right)\right] + 1.2\left[1 - exp\left(-\left(\frac{Re_d'}{4500}\right)^{0.7}\right)\right] \tag{2-32}$$

$$C_{Da} = \frac{1+S}{1-\lambda} C_D' \tag{2-33}$$

where C_{Da} = drag coefficient for a cylinder array

Figure 2-19 illustrates the distribution of the data points plotted according to the pseudofluid model, the data points are no longer grouped according to cylinder concentration, as in Figure 2-18, and can be represented by a single curve (solid line) given by equation (2-32). This curve applies to both single and multiple cylinder scenarios. The calculation of the drag coefficient for a cylinder array is given as follows:

1. Calculate Re'_d using equation 2-31.
2. Calculate C'_D using equation 2-32.
3. Calculate C_{Da} using equation 2-33.

3 EXPERIMENTAL INVESTIGATION

3.1 Introduction

The experimental investigations were conducted in the hydraulics laboratory of the School of Civil and Environmental Engineering, University of the Witwatersrand.

The experiments were carried out in a single laboratory flume (Figure 3-1) under controlled and idealized conditions with the objective of determining the magnitude of the drag force exerted on a cylinder of known dimensions. The experimental programme involved suspending an object a negligible distance above the flume floor and subjecting it to various discharges at varying velocities by means of adjusting the flow depth. The flow depth was adjusted by means of a downstream sluice gate. Circular, square and a diamond shape cylinders were investigated. Lastly experiments using multiple cylinders were carried out



Figure 3-1: Flume A. School of Civil and Environmental Engineering Hydraulics Laboratory.

Three different apparatus configurations were used as difficulties arose with the first two configurations.

3.2 Apparatus

The major obstacle during this investigation was finding a consistent and repeatable way to measure the drag force exerted onto the object. Different methods of measuring the drag force have been used by different researchers. Kothyari *et al*. (2009) connected a cylinder to a load cell (Figure 3-2) to measure the moment acting on the cylinder which was then related to the drag force. Ishikawa *et al*. (2000) attached strain gauges to an acrylic plate which was then connected to the cylinder on one side and a stationary mount on the opposite end, the acrylic plate would then flex in proportion to the applied drag force and the magnitude of flexure was calibrated to the drag force. Thompson *et al*. (2003) and Madhi and Bismilla (2014) used similar apparatus in that they both connected a cylinder to a linear motion slide which was in turn connected to a load cell which was mounted to a structure that was attached to the sidewalls of the flume allowing for direct measurement of the drag force.



Figure 3-2: Lorenz Messtechnik K-1107 10 Newton tension force sensor photograph. (Lorenz Messtechnik GmbH, 2015)

The apparatus originally used by Madhi and Bismilla (2014) was available and it was therefore logical to begin experiments using this apparatus hereinafter labelled Configuration 1. The following two apparatus subsequently used are labelled Configuration 2 and Configuration 3 respectively.

3.2.1 Configuration 1

Originally the same apparatus used by Madhi and Bismilla (2014) was utilized as shown in Figure 3-3. The apparatus consisted of a frame which was supported by the flume walls. This frame in turn supported two drawer sliders which in turn supported a steel plate, the steel plate was used to suspend the cylinder by means of a steel rod (Figure 3-4). A Lorenz Messtechnik K-1107 10 Newton tension force sensor (Figure 3-2) was mounted by one of its ends to the sliding plate and the other end was connected to the frame. The force sensor is extremely sensitive and fragile and it was therefore necessary to remove the sensor from the apparatus after each laboratory session for safekeeping.

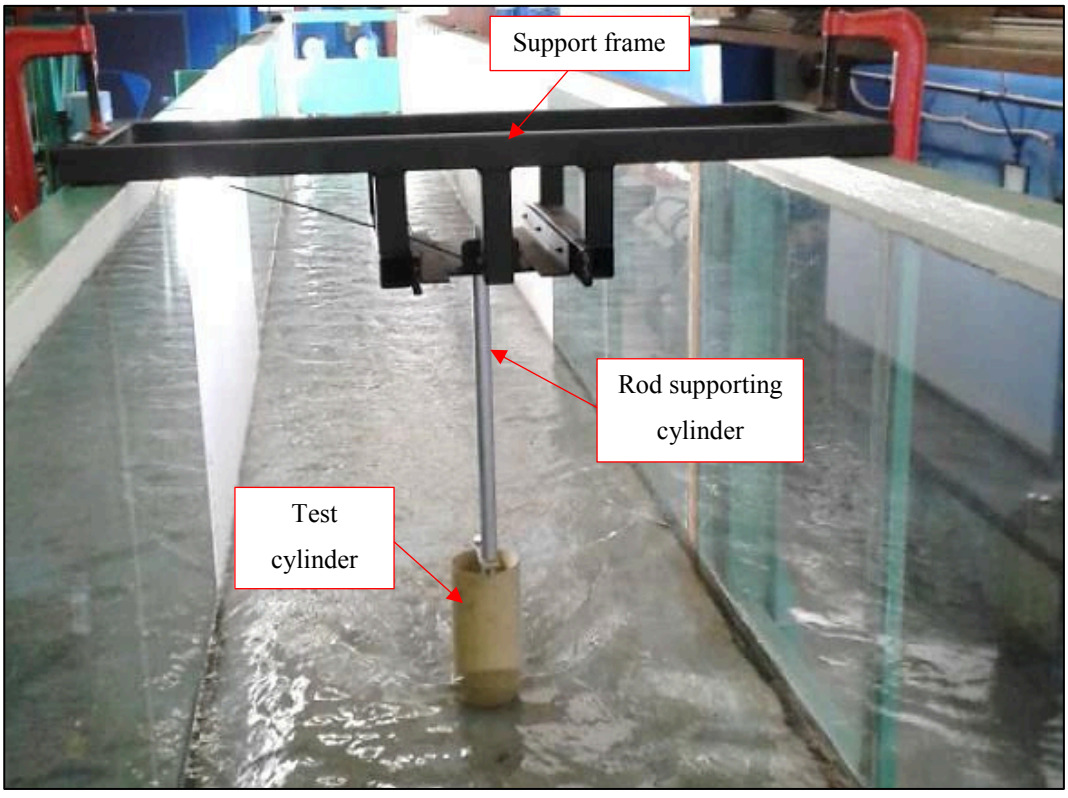

Figure 3-3: Configuration 1 apparatus set up. (Madhi & Bismilla, 2014)

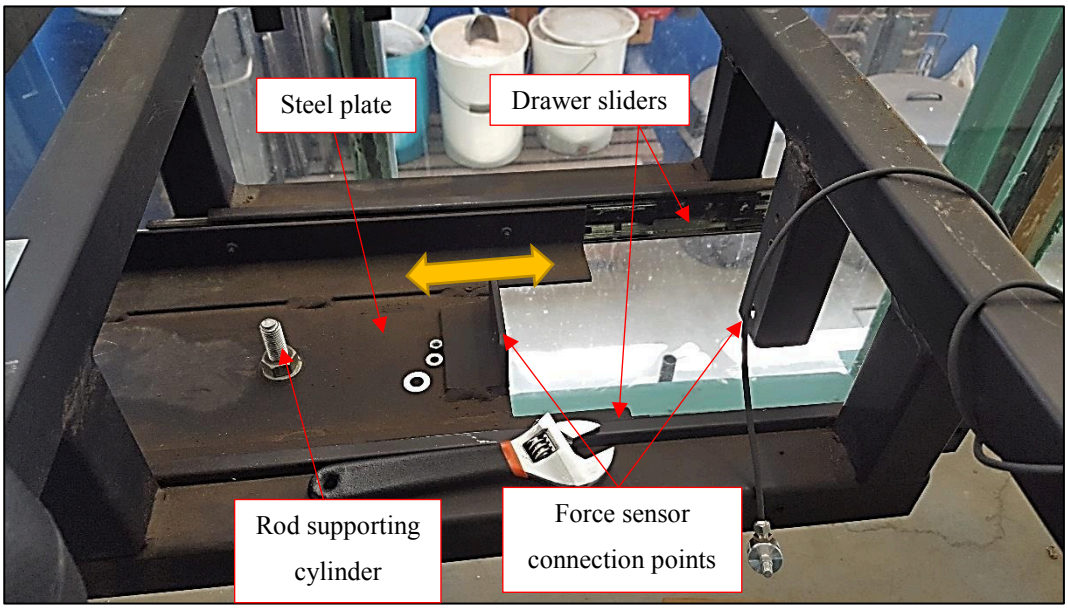

Figure 3-4: Configuration 1 sliding mechanism

The sliders were found to have a number of downfalls which include the following: -

1. The sliders had a variable magnitude of friction along their length. During calibration tests, it was found that in some locations the force required to move the sliding plate exceeded the load capacity of the force sensor. This did not mean that the force sensor would not register any load in this region, but the load cell reading would not be a true reflection of the actual load. Since the force sensor had to be removed after each laboratory session, the position of the slider during each consecutive session would not be guaranteed to be consistent and therefore it was not realistic to attempt to quantify the friction in the slider at one location and use this to calibrate the apparatus.
2. It was originally proposed that the reason for the variable friction was due to the sliders sitting for a year and accumulating dust and dirt around the ball bearings. The sliders were thoroughly cleaned with paraffin and re-lubricated. Although this did reduce the friction substantially, the magnitude of friction remained variable.
3. Each slider consists of an arm which can move in a linear direction relative to a stationary support by means of a ball bearing track on the top and bottom of the arm (Figure 3-5). This track is however exposed to the environment and dust

and dirt can easily access the track. This means that with time the friction of the sliders will increase.

It was for the abovementioned reasons that the decision was made to discontinue the use of the apparatus

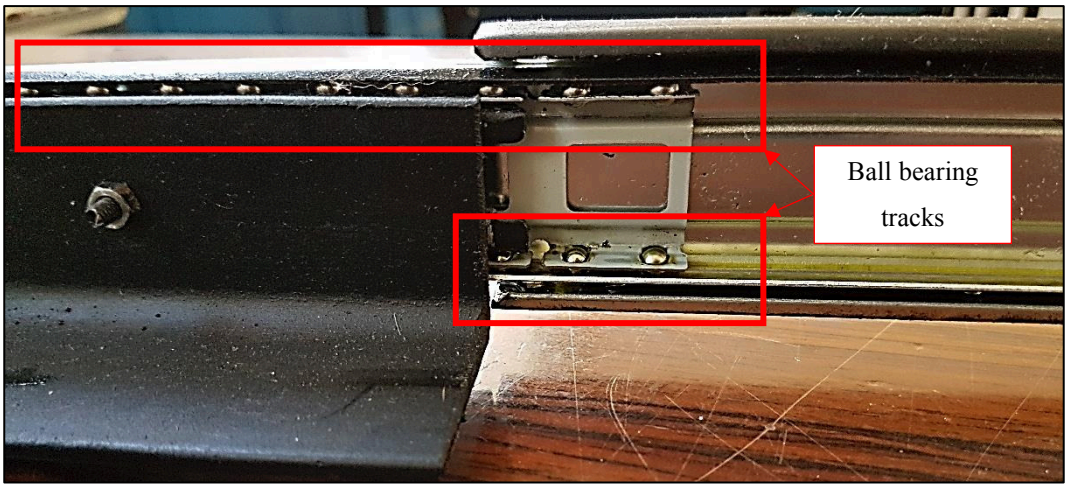

Figure 3-5: Close-up of ball bearing tracks.

3.2.2 Configuration 2

Problems with variable friction in Configuration 1 required a new apparatus to be designed. The same concept as Configuration 1 was adopted, however, the drawer sliders were removed and the sliding plate was brought closer to the flume floor to reduce the mass being suspended below it.

The frame was composed of 50 mm square hollow tubing welded together. As with Configuration 1, the mounting frame was supported by the sides of the flume (Figure 3-6). A secondary frame was welded to the mounting frame. This secondary frame consisted of a rectangular frame, in plan, which was suspended at each of its corners by tubes which connected to the mounting frame. Four 9 mm outside diameter shielded ball bearings were mounted within the rectangular frame such that the top surfaces of the bearings were all level. The ball bearings allowed a 5 mm thick steel plate to move laterally with very low friction (Figure 3-7). The steel plate was machined, surface-ground and polished to ensure smooth, low friction movement. In the centre of the plate an 8 mm diameter hole was drilled. The hole

was necessary to secure a threaded rod to the plate and this threaded rod was fixed on the other end to the cylinder. The cylinder consisted of a 110 mm diameter PVC pipe which was 250 mm in length, at the bottom of the cylinder a piece of acrylic plate was stuck to the cylinder in order for the threaded rod to be centrally mounted about the cylinder. Several holes were drilled into the acrylic plate to allow water into the cylinder to prevent excessive buoyancy.

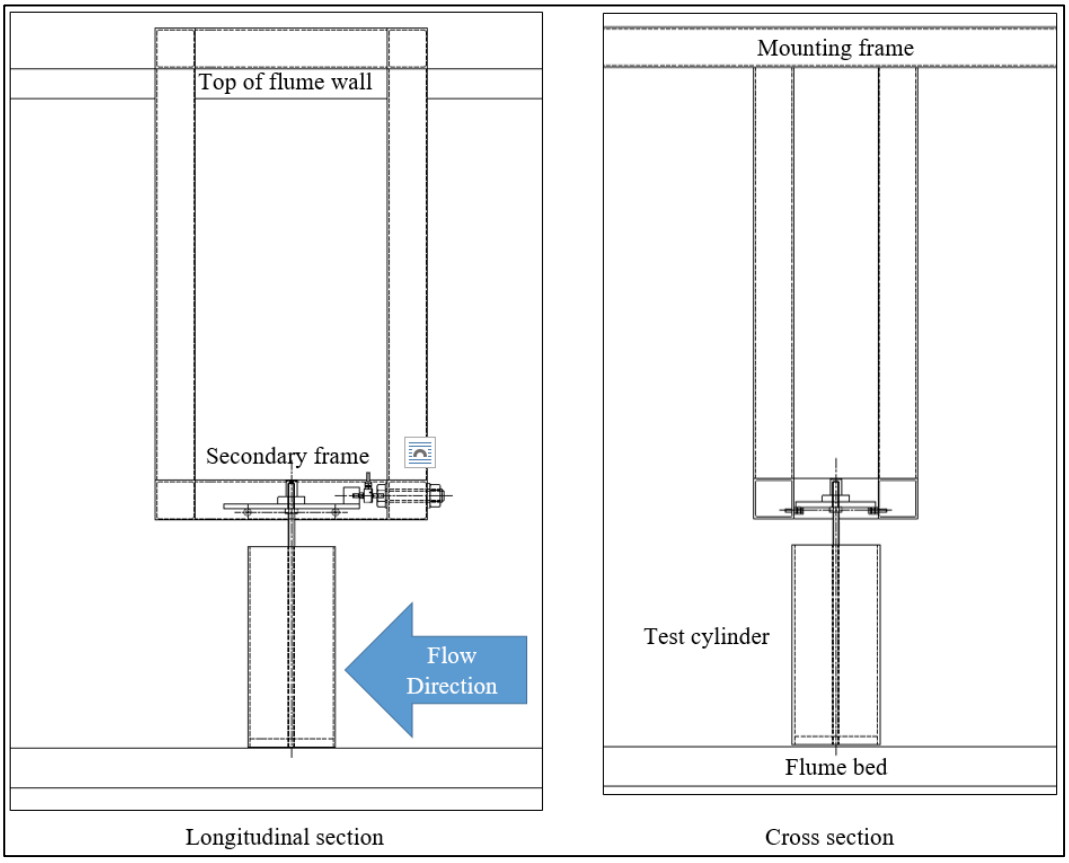

Figure 3-6: Configuration 2 schematic. Longitudinal and cross sections.

A 20 mm x 40 mm steel tab 3 mm thick was welded to the steel plate and in the centre of the tab a 6 mm diameter hole was drilled through, allowing the load cell to be connected to the plate with a single M5 nut. An 18 mm diameter hole was drilled through the rectangular frame such that an M16 bolt could be secured to the frame. At the top end of the bolt a hole was drilled partially into the centre of the bolt's shaft and the hole was then tapped to accommodate the M5 thread of the load cell.

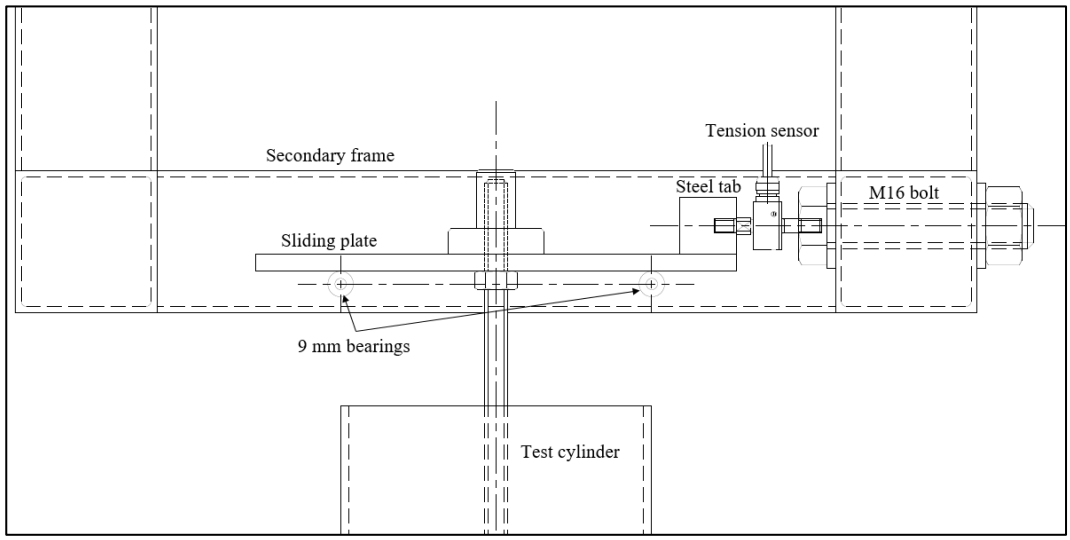

Figure 3-7: Close-up of configuration 2 sliding mechanism.

During initial tests, it was found that the cylinder (and consequently the plate) showed a tendency to lift in the front due to the water's drag force and at higher velocities the cylinder would oscillate rhythmically in a lateral direction due to the vortex shedding. These mechanisms weren't ideal as they made the drag force graph very inconsistent and it also increased the risk of damage to the load cell. It was therefore decided to add another ball bearing to the system. A 30 mm x 3 mm wide groove was milled into the top face of the sliding plate about 1 mm deep. The new ball bearing was then mounted to the top of the rectangular frame such that the 2.5 mm wide bearing was positioned within the groove. This bearing prevented the plate from lifting and confined the lateral oscillations (Figure 3-8).

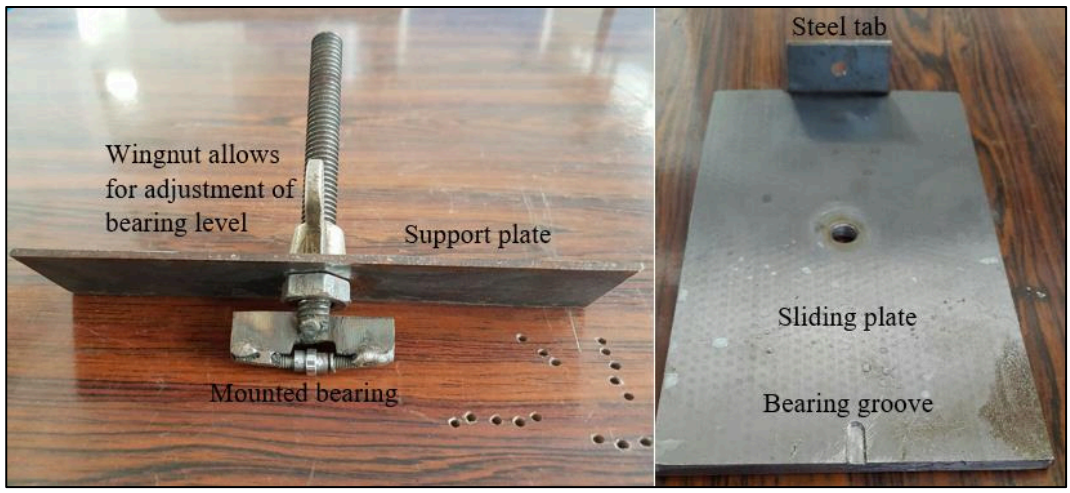

Figure 3-8: Stabilizing mechanism.

The apparatus produced consistent and low friction results during calibration and it was deemed suitable for experimentation. A large number of data points were collected using this apparatus, however a few drawbacks were encountered whilst using this apparatus including the following: -

1. The steel plate was susceptible to rust and therefore required cleaning before, and oil application after, each laboratory session;
2. Even though the internal friction within the system was very low, at low velocities the drag force measured by the load cell was of the same order of magnitude as the load cell's lower bound accuracy and thus the readings were unreliable. This limited the range of Reynolds numbers that could be achieved with the apparatus;
3. The dimensions of the frames limited the height of cylinder that could be used and thus limited the flow depths and the corresponding Reynolds number range.

To expand on the Reynolds number range it was decided to use a longer cylinder of 450 mm. The frame was lifted by using two 200 mm high spacers in the form of 300 mm rolled I-sections. The modification did increase the sample range but it was incapable of taking readings near the lower bound of the target range. It was therefore decided that a new design was required to achieve this objective; this resulted in the design of Configuration 3.

3.2.3 Configuration 3

Configuration 1 and 2 were not sensitive enough to produce reliable readings at low velocities and a deep flow and therefore insufficiently sensitive to cover the predetermined target range. At low velocities, the range of drag forces being measured was within the lower bound of the tension sensor's capacity and in some cases the load was too low for the sensor to accurately register. To overcome this problem there were two possible modifications that could be made; changes to the cylinder itself or alternatively to the apparatus. The length of the cylinder was already close to the maximum flow depth achievable in the flume and it was therefore decided that extending the cylinder any further would be a futile task. This

meant that the remaining option was to modify or design new apparatus. It was conceived that the way to improve Configuration 2 would be to attempt to reduce the rolling friction of the sliding plate, which would have increased the sensitivity of the system. However, the sliding friction was already low and only marginal, if any, improvements could be made in this regard. The rolling surface of the sliding plate was well polished and the ball bearings utilized were of the lowest rolling resistance on the market. It was thus concluded that a new design would be required.

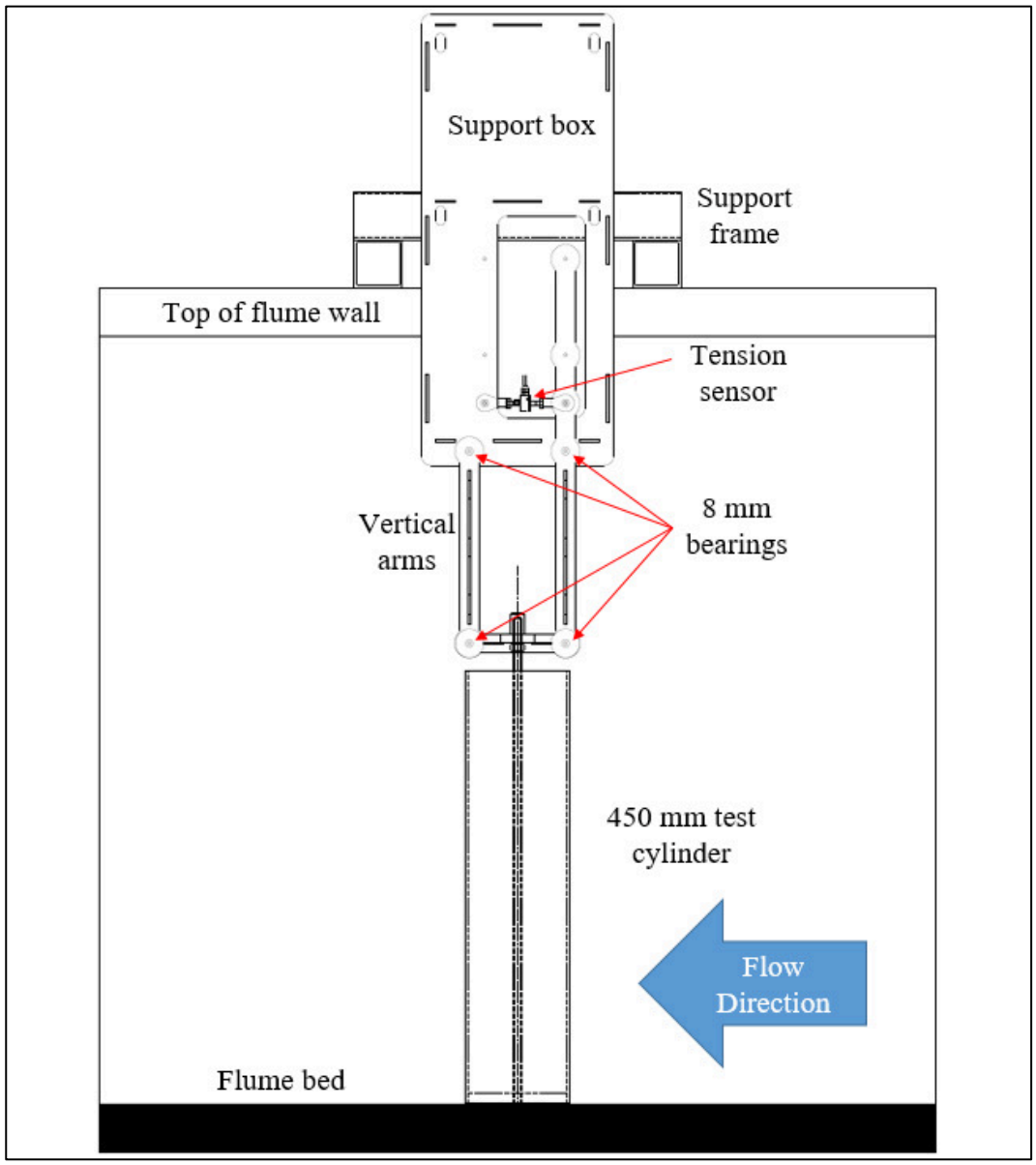

Figure 3-9: Configuration 3 schematic.

The primary objective of the new apparatus would be to amplify the tensile force being exerted onto the sensor such that even the very low forces would register well within the sensor's low bound range. Several configurations were initially considered from which the better configurations were identified and refined until a design was settled on.

The design (Figure 3-9) consists of a box which is mounted to a frame which is supported by the side walls of the flume similar to the frames used in Configuration 1 and 2. The box was designed in such a way that multiple sized cylinders, namely a 250 mm and a 450 mm high cylinder, could be attached when the box was mounted in various positions. At the bottom of the box two 4 mm diameter threaded rods were secured horizontally through the box. The threaded rods supported two arms which extended vertically; the arms were seated on the rods via 8 mm outside diameter ball bearings on either side of the arms and the bearings were epoxied into holes drilled through the arms. The other ends of the arms were connected to a horizontal plate and again threaded rods were slotted into bearings which were secured in hole through the arms. To prevent the arms from slipping off the threaded rods, M4 nuts were used. These nuts were bigger than the bearings and had to be ground down to ensure the bearings could rotate freely. The horizontal plate had a centrally located 8 mm diameter hole through which an 8 mm threaded rod was secured, which in turn supported the cylinder as in Configuration 1 and 2.

Two arms were used to ensure that the horizontal plate remained level when moving and they also added stability to the system. One of the arms, on each side, was longer and extended past the top pivot point and on this section of the arm three holes were drilled at varying distances from the pivot point (Figure 3-10). The largest distance was equal to the dimension from the pivot point at the box to the pivot point at the horizontal plate, the next distance was half and the smallest distance was a quarter of the dimension. Holes were drilled through the box such that the holes in the arm and the box were level with each other. Threaded rods, 5 mm in diameter, were secured into the sets of holes using M5 nuts. The threaded rods allowed the tension sensor to be attached to the system by means of two female M5 rose joints screwed onto either end of the sensor. The rose joint bearings were

then slid onto the threaded rods and clamped in place with nuts. The rose joints were adjusted in such a way that the arms hung vertically and freely without any force being exerted on the load cell while at rest.

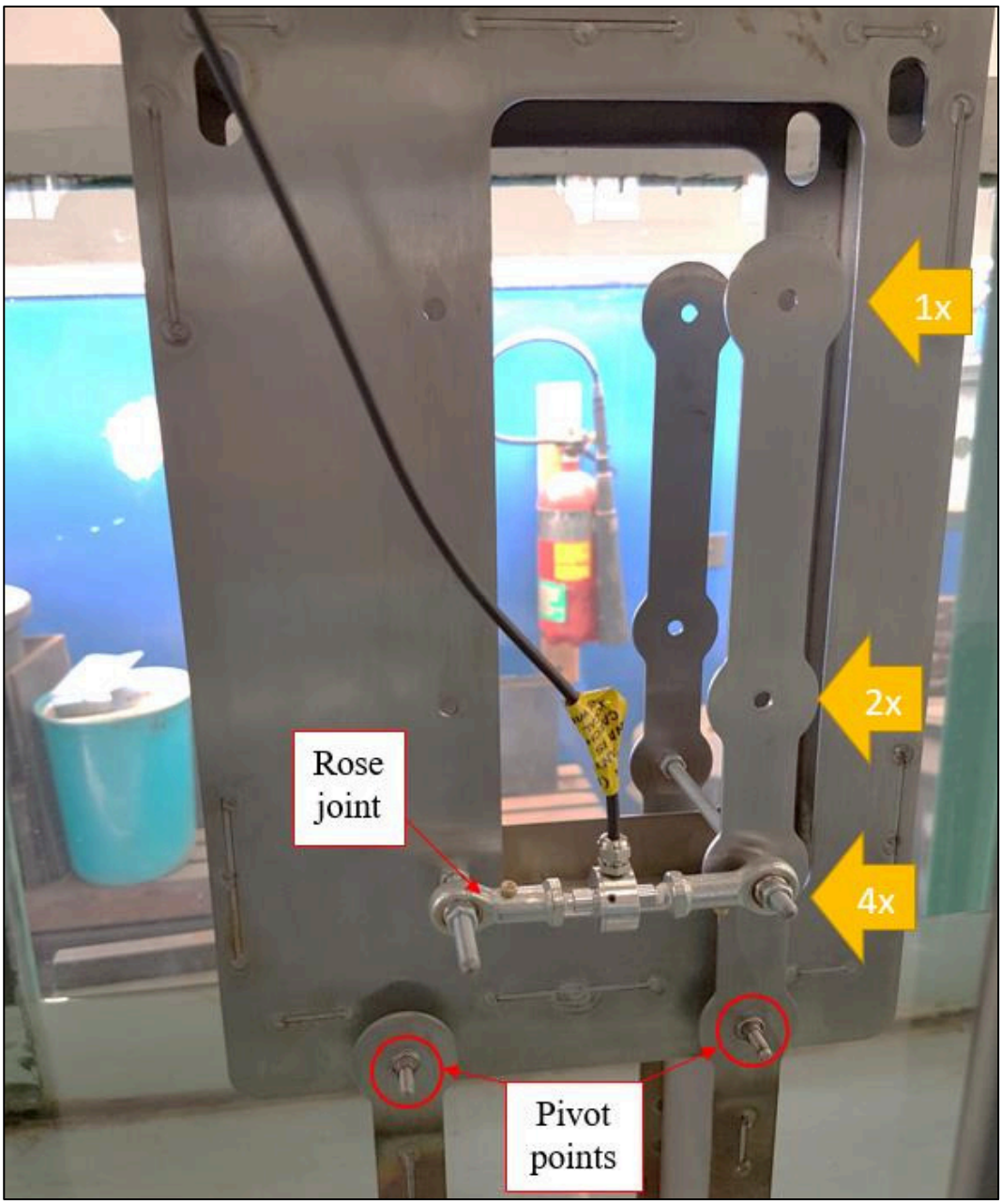

Figure 3-10: Tension tensor mechanism.

When the flowing water pushed against the cylinder it caused a moment about the pivot points at the box. To prevent rotation and maintain static equilibrium this moment had to be balanced by an equal and opposite moment; this moment was provided by the tension sensor resisting the rotation. The distance the sensor was

placed away from the pivot point determined the magnitude that the drag force was amplified. For low discharges and low velocities, the sensor was placed close to the pivot point for maximum amplification. For high discharges and high velocities, the sensor was placed further away from the pivot point.

The final design of the apparatus was done in AutoCAD and the components were laser cut from 2 mm thick stainless steel. The components were joined together with tongue and groove joints and secured with TIG spot welds.

The cylinder tended to lift as the arm rotates and this would result in a weight component causing a moment in the opposite direction to that of the drag force. The outcome of this would be a drag force reading less than the actual drag force, however, the rotation is confined by the tension sensor which deflects a negligible distance and therefore the error in the force reading would be negligible.

The apparatus performed its function effectively and loads were reliably registered at low discharges and velocities. The following drawbacks were identified during experimentation: -

1. Adjusting the rose joints to ensure there was no preload in the sensor and to ensure the cylinder hung perfectly vertical was a time consuming task. Plumbers tape was wrapped around the threads of the sensor to create a tight fit between the rose joint and sensor and this meant the sensor could be stored with the rose joints attached after each laboratory session without the rose joint moving. This saved a lot of time in setting up;
2. The amplification of the load that is applied to the sensor is as high as 4 times the load at the cylinder, therefore a small knock or a pressure spike to the cylinder could have overloaded the sensor. Extreme care had to be exercised when working near the apparatus. The flume had to be gradually filled and emptied at the beginning and end of a run and the downstream sluice gate had to be raised and lowered in very gradual increments to prevent surging and resulting pressure spikes.

3.3 Calibration

The calibration of the apparatus was necessary to determine the deviation of the load readings from the actual force being applied. Each configuration was individually calibrated, as well as the tension sensor itself. Refer to appendix A for the experimental data and pictures of the setup.

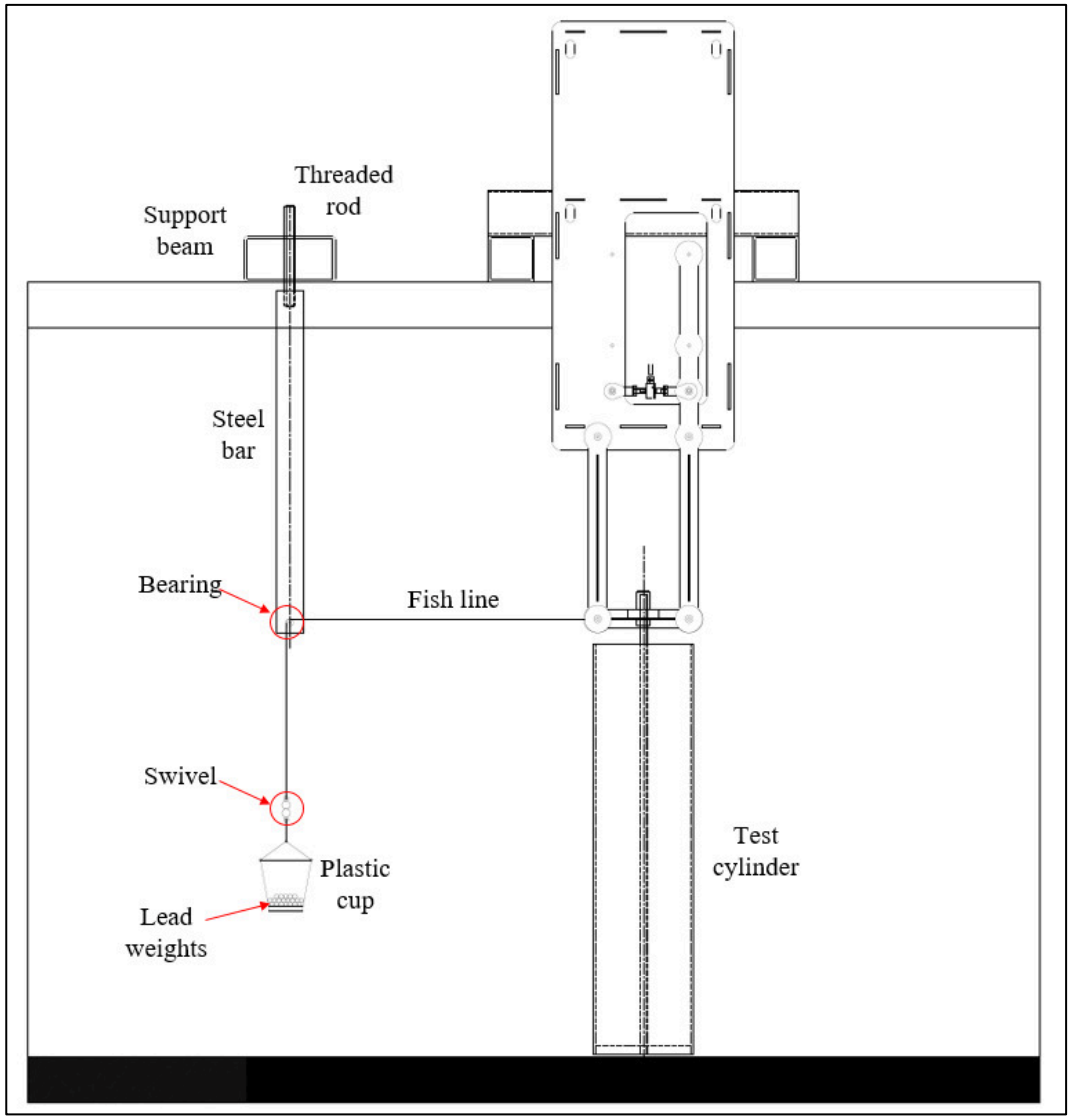

Figure 3-11: Calibration set-up

Equipment was designed and built to carry out the calibration tests (Figure 3-11). The equipment consisted of a steel beam which spanned the width of the flume and was clamped to the flume side walls with g-clamps. In the centre of the beam a 10 mm diameter hole was drilled through to accommodate a M10 threaded rod with a

wing nut on the top and bottom. The threaded rod was in turn welded to a square steel bar which hung vertically into the flume. On the end of the bar a small ball bearing was mounted and the ball bearing performed as a pulley.

The wingnuts allowed for easy adjustment of the height of the ball bearing above the flume floor. The height of the ball bearing was adjusted for each apparatus configuration such that the top of the ball bearing was level with the cylinder support plates. In the centre of the front edge of each support plate, a 1.5 mm diameter hole was drilled and through which a piece of 0.22 mm 8 lb fishing line could be secured. The fishing line was chosen because it is extremely strong and light. The line was then placed on top of the bearing with the end hanging vertically. A string line pocket spirit level was hung on the horizontal part of the line to ensure the line was level (and therefore the top of the bearing and plates were level).

A light plastic cup was hung from the fishing line and lead fishing sinkers were placed into the cup in 10 gram increments. The mass of the cup and sinkers was measured with a pocket scale, which is accurate to 0,01 grams. These measurements were recorded after each additional weight increment was applied. It was found that the cup would rotate back and forth whilst hanging from the line and this made the readings unstable. A fishing swivel was then added between the cup and the line to prevent the rotations and consequently stabilised the readings.

In each calibration test performed on the three respective configurations the apparatus was set up identically to the set up for the experiments to ensure accuracy. The mass range was between 20 and 700 grams. It was not necessary to go all the way to the tension sensor's capacity as the maximum drag forces expected were no more than 4 Newtons (≈ 400 grams).

The tension tensor itself was calibrated in a similar manner. A small bolt was tapped through the top such that it could be screwed onto the one end of the sensor and the other end of the bolt had a small hole drilled through it so that the fishing line could be tied to it. The other end of the sensor was connected, using another bolt, to the stationary frame. Loads were then applied as for the other calibration tests.

To determine the magnitude of friction imparted by the pulley, the load cell was hung vertically and increasing weights were then incrementally hung from the load cell. The resulting difference between the two calibration tests could then be attributed to the pulley and therefore accounted for in the calibration tests done on the other apparatus.

The respective configurations and the tension sensor were each calibrated once. An additional calibration was carried out on configuration 2 to determine what influence dynamic conditions would have on the results, as opposed to the static conditions being utilised. The dynamic tests were carried out in an identical manner, however, after each consecutive load increment the sliding plate was disturbed by moving it off the nut attached to the tension sensor and then releasing it again so that it could return to its original position. This was repeated 3 times before the load was captured.

3.4 Verification tests

Once the calibration tests were completed it was important to carry out verification tests to determine whether the data being collected was realistic. It was decided that the most appropriate method of verifying the results would be to compare the measured results to the well-researched relationship between the drag coefficient and cylinder Reynolds number of an infinitely long cylinder. Infinitely long is a relative concept. Jayaweera and Mason (1965) described a long thin cylinder as one in which the cylinder aspect ratio (L/D) was greater than 100. The challenge with these experiments was selecting a cylinder diameter which was small enough to be considered ‘thin’ but thick enough to register reliable drag forces subject to the range of possible flow conditions possible in the flume. It was decided that the most accommodating diameter in satisfying these requirements would be 20 mm which gave a cylinder aspect ratio of 45.

The verification tests were carried out with the Configuration 2 apparatus. Initially a 20 mm PVC pipe was supported by two vertical 4 mm diameter threaded rods which in turn were connected to a shorter section of the same PVC pipe. An 8 mm

threaded rod was connected to the middle of this shorter section and this threaded rod was then bolted to the centre of the sliding plate. The set up was flexible and the single threaded rod was unable to prevent the set-up from rotating. Substantial vibrations occurred during initial tests, the vibrations had made the readings unreliable and it was therefore necessary to change the set up.



Figure 3-12: Verification test set-up.

The new set up (Figure 3-12 and Figure 3-13) required more rigidity and a method to dampen out any vibrations as they occurred. A new solid acrylic 20 mm diameter rod was used. The rod was supported by a galvanised steel sheet frame. The frame was designed using AutoCAD software and the design was then drawn on a flat 0.6 mm thick sheet of galvanised steel. This was then cut from the sheet and bent into shape. Tabs on the edges were strategically placed such that spot welds could be made to secure the edges together. The spot welds did not sufficiently hold in certain locations and it was necessary to add rivets. The frame was stiffened with additional sections of steel plate which were riveted near the support point. The acrylic rod was mounted to the frame by cutting slits into the rod and gluing the protruding tabs of the frame into the slits. To minimise the drag induced by the part of the frame in contact the water, the protruding tabs were orientated in such a way that the plane of the tabs was parallel to the flow of the water and only the 0.6 mm thickness of the sheet was perpendicular to the flow. Two threaded rods were used

to connect the set-up to the sliding plate instead of just one, to prevent rotation of the set-up. The threaded rods were secured to the steel stiffener plates with lock nuts and were connected to the sliding plate using wing nuts. The wing nuts allowed for easy height adjustment of the acrylic rod. The top of the galvanised frame was flat and made it possible to add weights which were applied to stop vibrations when they were observed. The set up worked as intended and several data points were captured. Refer to appendix B for the experimental data and pictures of the setup.

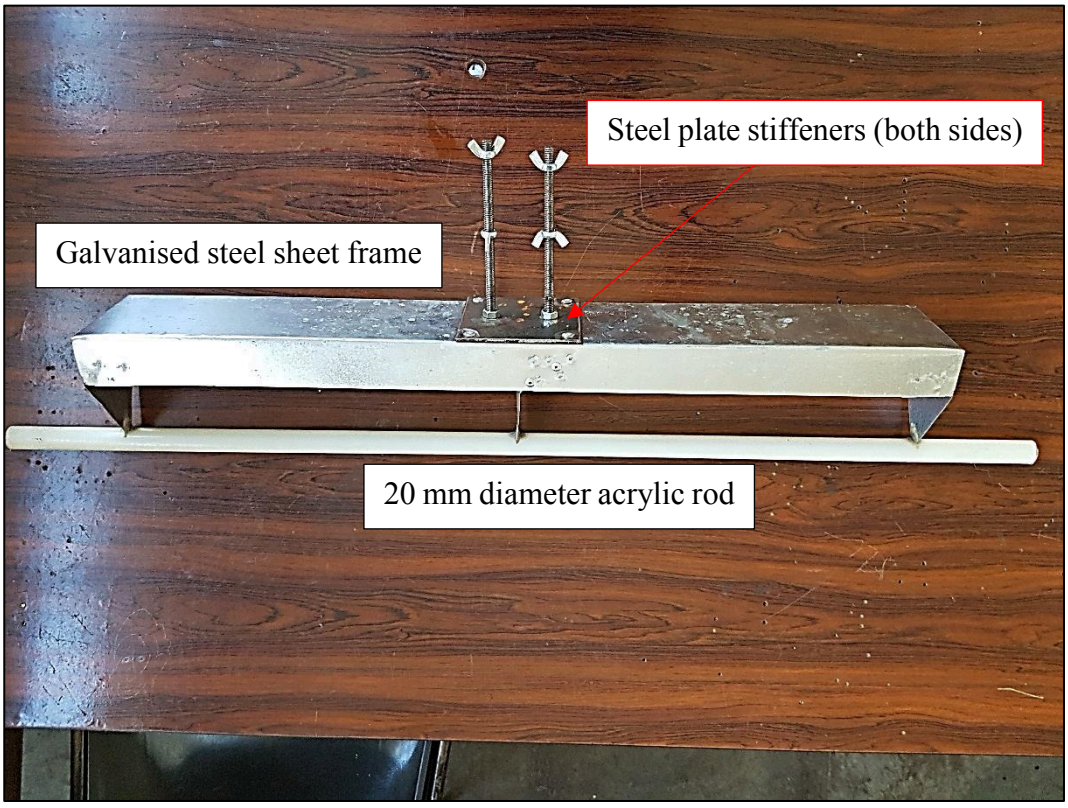

Figure 3-13: Horizontal cylinder support

The following procedure was adopted when carrying out the verification tests: -

1. The horizontal cylinder set up was first connected to the sliding plate. Using the wing nuts, the height of the cylinder off the floor of the flume was adjusted to until was at approximately the target height.
2. The apparatus was then levelled by placing the frame on top of the flume side walls and then putting the sliding plate on top of the bearings. A digital point gauge was then placed on top of the frame and a trough of water placed directly underneath the frame. Once the water had settled, the height from the water

surface to the top of the sliding plate on both ends (parallel to the flow) was measured and compared. Using 0.5 mm packing plates between the frame and the top of the flume side walls, the frame was tilted until the heights were equal and the sliding plate was therefore level.

3. The horizontal cylinder was then levelled in a similar manner to the abovementioned method. A trough of water was placed underneath the cylinder so that it spanned the length of the cylinder. Using the point gauge, the height from the water surface to the top of the cylinder was measured on either ends and compared. The heights were then adjusted by differentially manipulating the position of the wing nuts on the two threaded rods connected to the sliding plate. In this way the horizontal cylinder was levelled.
4. The tension sensor was then connected to the apparatus. A bolt was screwed onto the sensor on one end bolted to the frame on the other so that the opposite end of the sensor lined up with the hole in the tab of the sliding plate. This was the most time consuming task as it was difficult to get the sensor to line up, and keep it, lined up whilst tightening the nut without it touching the sides of the hole.
5. Once the sensor was correctly lined up, the sliding plate was placed on the bearings and slid into place so that the sensor could be connected to the tab by means of a nut.
6. The device housing the top bearing was then placed on top of the rectangular frame such that the bearing sat within the groove on top of the sliding plate. The device was then clamped to the frame using two g-clamps. The bearing could then be adjusted by means of a wing nut so that the bearing just touched the floor of the groove.
7. The tension sensor software was launched on the laptop and the sensor was plugged into the laptop via a USB port. The software detects the sensor and displays a graph and digital readout for the sensor.
8. The software allows the user to set several sensor variables such as the sampling rate, number of decimal places and units required.
9. The sliding plate was moved in such a way that the tab was not pressing against the nut and therefore not exerting any preload through the sensor. The sensor

was zeroed by starting and stopping the measurements a few times until the sensor remained stable on zero.

10. The pump was started and the constant head tank started filling up until water started to spill over the series of weirs in the tank.
11. The valves leading to the flume were opened and the digital flow meter gauge was switched on.
12. With the tailgate fully open, the final valve leading into the flume was gradually opened in increments until the target discharge reading was displayed and remained stable on the flow meter.
13. The tailgate was incrementally raised until the target flow depth at the cylinder was reached. The gate had to be raised in such a way that water was flowing over the gate continuously. If it was raised too fast and the flow was choked then large surface waves would travel back to the cylinder and cause violent pressure spikes on the cylinder placing the tension sensor at risk of being disturbed from its zero point and rendering the measurements invalid, or in the worst case over-loaded.
14. Once the approximate water level had been achieved, the flow was left for between 5 and 10 minutes to stabilize. The flow was accepted as stable when the graph levelled out and remained between an approximate minimum and maximum value.
15. The discharge was read off the digital flow meter and recorded on an Excel spreadsheet.
16. The drag force was estimated from the graphical output of the tension sensor's software. This was recorded in the Excel spreadsheet. After the completion of the run the graph, as well as the measured values, were recorded. The measured values were stored in a CSV file. Using this file together with the graph, to identify at what time the drag force was stable, the measured values were averaged to obtain a more accurate drag force which then replaced the initial estimate.
17. The flow depth was determined using a digital point gauge. The point gauge was clamped to the frame to take measurements at a consistent location. The point of the gauge was located 150 mm to the side of the centre of the cylinder

and in line with the front of the cylinder. For each measurement, the point was lowered to the flume floor and zeroed and then raised to the water surface where measurements accurate to 0.01 cm were taken. These measurements were recorded in the Excel spreadsheet.

18. Using a digital water velocity meter, the local velocity was measured 15 cm upstream of the cylinder and along the centre line of the flume. The measured velocity was accurate to 0.01 m/s. This was later found to be insufficiently accurate and it was therefore decided to make use of a miniature propeller meter in conjunction with the velocity meter. The miniature propeller meter is accurate to ± 1.5% of the true velocity. The propeller meter produces a very erratic read out which warranted the need for the velocity meter to gauge roughly what the flow rate was expected to be.
19. The Excel spreadsheet was set up such that new data points were immediately input into several graphs illustrating different relationships. The graphs were the relationship between the drag coefficient and cylinder Reynolds number (local and average velocity), the drag force versus cylinder Reynolds number and drag force versus velocity squared from these graphs. The collected data could be compared to established relationships for "infinitely long" cylinders. Outliers that did not conform to these relationships could be picked up and more data points could then be collected in these areas to determine whether the points were errors.
20. Data points were captured over the Reynolds number range achievable with the apparatus and flume flow range. This range was 1279 to 7105.

3.5 Single cylinder experiments

Once the calibration and verification tests were completed and the apparatus was performing satisfactorily, the experimental investigation commenced. The first investigation was carried out on a single vertical circular cylinder followed by the investigations of square and diamond shaped cylinders to investigate the influence of the cylinder shape on the results.

The circular cylinder was a 110 mm diameter PVC pipe which was 250 mm high. The cylinders were all supported by threaded rods through their centres by means of plastic plates bonded to their cross-sectional ends. The length of the circular cylinder was later increased to 450 mm to cover a larger range of flow conditions, namely larger flow depths and low velocities (and therefore Reynolds numbers). The range of possible values was then further expanded by using a 25 mm diameter PVC pipe, 450 mm long.

Originally the square cylinder was made from 76 mm square hollow steel tubing with a 6 mm plate welded to the top of it where the threaded rod was attached to. The cylinder was, however, heavy and not responsive at low discharges and velocities. The mass of the steel cylinder increased the rolling resistance of the bearings. A new cylinder was therefore required. The second attempt consisted of a 100 mm by 100 mm by 450 mm box made using 4 mm thick Perspex sheeting and bonded together with methylene chloride. This method ensured the corners were sharp. The cylinder was orientated such that one of the sides was perpendicular to the flow direction.

The diamond cylinder made use of the same square cylinder by rotating it through 45 degrees in plan.

Configuration 2 produced many data points which proved satisfactory. The apparatus suffered mechanical damage during the setup for the multiple cylinder experiments. An attempt was made to repair the apparatus but was deemed unsatisfactory and it was decided that it would be best to design a new apparatus and to improve on the limitations of Configuration 2. This resulted in Configuration 3 which is described in section 3.2.3 above.

Configuration 3 widened the range of Reynolds numbers that could be read and therefore the singe cylinder tests were continued to obtain data points for lower Reynolds numbers. There was overlapping of the data points from both configurations. The data points were in close agreement with each other which gave credibility to the results of both sets of equipment.

Table 3-1 is a summary of the experimental conditions for the single cylinder experiments. Refer to appendix C for the experimental data and pictures of the cylinders used.

Table 3-1: Single cylinder experimental conditions

Test No.	Cylinder Shape	Number of runs	Cylinder Diameter (mm)	Cylinder length (mm)	Discharge range (l/s)	Flow depth range (mm)	Reynolds number range
1	Circular	26	110	250	3,44 - 59,06	67,15 - 251,94	1160 - 50265
2		2	110	450	21,70 - 91,50	407,94 - 424,64	1260 - 5112
3		4	40	450	40,30 - 90,00	236,62 - 248,57	1399 - 3200
4	Square	18	100	450	5,17 - 52,75	93,93 - 428,93	1047 - 43532
5	Diamond	10	100 (side lengths)	450	5,58 - 45,50	247,61 - 430,60	1065 - 14268

The following procedure was adopted when carrying out a run for either configuration. The procedure for configuration 2 is slightly different to configuration 3. For brevity, the one procedure is presented below. The normal test applies to both configurations, the bold text applies to configuration 2 only and the underlined text applies to configuration 3 only.

1. The cylinder was first connected to the horizontal plate. A 2 mm thick spacer plate was placed between the flume floor and cylinder. Using the wing nuts, the height of the cylinder off the floor of the flume was adjusted until it came to rest on the plate. The plate was then removed leaving a 2 mm gap.
2. **The apparatus was levelled by placing the frame on top of the flume side walls and then putting the sliding plate on top of the bearings. A digital point gauge was placed on top of the frame and a trough of water was placed directly under the frame. Once the water had settled, the height from the water surface to the top of the sliding plate was measured and compared on both ends (parallel to the flow). Using 0.5 mm packing plates between the frame and the top of the flume side walls, the frame was tilted until the heights were equal and the sliding plate was therefore level.**

3. **The tension sensor was connected to the apparatus. A bolt was screwed onto the sensor on one end and bolted to the frame on the other so that the opposite end of the sensor lined up with the hole in the tab of the sliding plate. This was the most time consuming task as it was difficult to get the sensor to line up, and keep it lined up, whilst tightening the nut without it touching the sides of the hole.**
4. **Once the sensor was correctly lined up, the sliding plate was placed on the bearings and slid into place so that the sensor could be connected to the tab by means of a nut.**
5. **The device housing the top bearing was then placed on top of the rectangular frame such that the bearing sat within the groove on top of the sliding plate. The device was then clamped to the frame using two g-clamps. The bearing could then be adjusted by means of a wing nut so that the bearing just touched the floor of the groove.**
6. The apparatus was then adjusted so that the vertical arms hung perfectly vertical. A spirit level was placed against the sides of the vertical arms and then using 0.5 mm packing plates between the frame and the top of the flume side walls, the frame was tilted until the bubble of the spirit level came to rest in the centre of the tube.
7. The tension sensor was connected to the apparatus. Two rose joints were connected to either side of the tension sensor. Plumbers tape was wrapped around the threads of the sensor to ensure a tight fit between the sensor and the rose joints.
8. The rose joint bearings were slid onto the threaded rods and clamped in place with nuts. The rose joints were adjusted by rotating them in or out such that the vertical arms hung vertically and freely without any force exerted on the load cell at rest. The position of the load cell was predetermined by estimating the magnitude of forces expected. The lower the expected loads, the lower the load cell was placed on the vertical arms to multiply the load.
9. The tension sensor software was launched on the laptop and the sensor was plugged into the laptop via a USB port. The software detects the sensor and displays a graph and digital readout for the sensor.

10. The software allows the user to set several sensor variables such as the sampling rate, number of decimal places and units required.
11. **The sliding plate was moved in such a way that the tab was not pressing against the nut and therefore not exerting any preload through the sensor.**
12. The sensor was zeroed by starting and stopping the measurements a few times until the sensor remained stable on zero.
13. The pump was started and the constant head tank started filling up until water started to spill over the series of weirs in the tank.
14. The valves leading to the flume were opened and the digital flow meter gauge was switched on.
15. With the tailgate fully open, the final valve leading into the flume was gradually opened in increments until the target discharge reading was displayed and remained stable on the flow meter.
16. The tailgate was incrementally raised until the target flow depth at the cylinder was reached. The gate had to be raised in such a way that water was flowing over the gate continuously. If it was raised too fast and the flow was choked then large surface waves would travel back to the cylinder and cause violent pressure spikes on the cylinder, placing the tension sensor at risk of being disturbed from its zero point and rendering the measurements invalid or in the worst case over-loaded.
17. Once the approximate water level had been achieved, the flow was left for between 5 and 10 minutes to stabilize. The flow was accepted as stable when the graph levelled out and remained between an approximate minimum and maximum value.
18. The discharge was read off the digital flow meter and recorded on an Excel spreadsheet.
19. The drag force was estimated from the graphical output of the tension sensor's software. This was recorded in the Excel spreadsheet. After the completion of the run the graph, as well as the measured values were recorded. The measured values were stored in a CSV file. Using this file together with the graph to identify at what point the drag force stabilised, the measured data was averaged to obtain a more accurate drag force which replaced the initial estimate.

20. The flow depth was determined using a digital point gauge. The point gauge was clamped to the frame to take measurements at a consistent location. The point of the gauge was located 150 mm to the side of the centre of the cylinder and in line with the front of the cylinder. For each measurement, the point was lowered to the flume floor and zeroed and then raised to the water surface where measurements accurate to 0.01 cm were taken. These measurements were recorded in the Excel spreadsheet.
21. The discharge and flow depth was used to calculate the velocity.
22. The Excel spreadsheet was set up so that new data points were immediately input into several graphs illustrating different relationships. From these graphs, any outliers or unusual trends could be identified and more data points could then be collected in these areas.
23. The procedure for obtaining data points involved capturing a data point at the lowest point of the target Reynolds number range and then a data point at the highest point of the target range. Data points were then collected by bisecting this range and continuing to bisect the ranges created by the previous bisection. If an obvious trend (linear or binomial) developed, the number of data points collected was enough to confirm the trend. If outliers or unusual trends developed, data points would be collected in that vicinity until the trend could be sufficiently determined.

3.6 Multiple cylinder experiments

Upon conclusion of the single cylinder experiments, the multiple cylinder experiments were carried out. The 110 mm circular cylinder was used in these experiments. The setup for the multiple cylinder experiments was identical to the single cylinder tests, the only difference being the arrangement of stationary cylinders placed upstream and downstream of the test cylinder. The cylinders consisted of 250 mm long sections of PVC pipe which were filled with concrete. A total of four different areal densities were tested, the spacing of the cylinders perpendicular to the flow was kept constant whilst the spacing of the cylinders parallel to the flow was varied. The same procedure adopted in the single cylinder experiments for Configuration 3 was implemented.

The process of setting up the multiple cylinders in their correct locations was a time consuming task and therefore hardboard templates were made to speed up the task whilst simultaneously making it accurate. 4 mm thick hardboard was cut to the width of the flume and in 1.2 m lengths, the position of each of the cylinders for the given arrangement was then marked out and using a 111 mm hole saw, the holes were cut to accommodate the cylinders. Threaded rods were used to support the boards off the flume floor. The reason for this was to keep the boards dry and prevent them from swelling, it also made the boards easier to remove after placing the cylinders. One board was made for each arrangement and after each section of cylinders were placed, the board was lifted and moved to the end of the section and more cylinders were then placed until it was deemed that there was a sufficient number of cylinders. Approximately 6 m of cylinders were placed upstream of the test cylinder and approximately 4 m of cylinders in the downstream direction. This ensured that the flow at the test cylinder was fully established and consistent.

Table 3-2 is a summary of the experimental conditions for the single cylinder experiments. Refer to appendix D for the experimental data.

Table 3-2: Multiple cylinder experimental conditions

Combination	Number of Runs	X	Y	λ (as defined by eq 2.1)	Discharge range (l/s)	Flow depth range (mm)
1	5	350	800	0.033	4,31 - 21,50	235,03 - 245,74
2	6	350	400	0.065	4,31 - 21,11	241,43 - 251,61
3	6	350	200	0.131	4,72 - 21,11	239,57 - 249,41
4	8	350	150	0.174	4,31 - 23,28	241,46 - 251,03

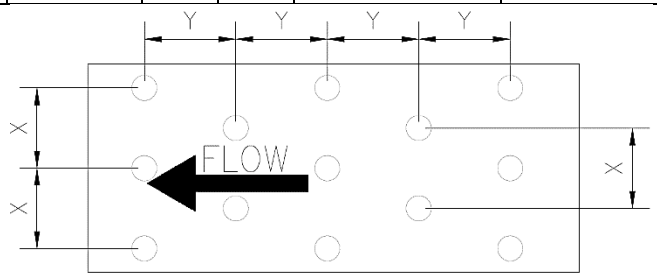

4 RESULTS

The results for the various tests carried out are broken up into sections corresponding to the methodology sections above. The results for the calibration and verification tests are briefly covered. The results for the various single and multiple cylinder experiments are comprehensively covered.

4.1 Calibration tests

A total of 5 calibration tests were carried out. Configuration 1, 3 and the tension sensor was calibrated once each. Configuration 2 was calibrated twice. The reason for carrying out a second calibration for Configuration 2 was to determine the difference between the results of a static and a dynamic test.

4.1.1 Tension sensor

It is apparent from the graph for the tension sensor (Figure 4-1) that the sensor is not accurately calibrated. The data points are expected to line up closer to the line of perfect agreement and the value for the slope of the straight trendline is expected to be slightly less than 1. In this case the slope is 0.8026. The reason for the inaccuracy could not be ascertained. A small percentage of the error can be attributed to the friction imparted by the pulley and possibly to the fish line not being perfectly level.

To determine the magnitude of friction being imparted by the pulley, a second test was carried out whereby the sensor was hung vertically from one end and weights were applied directly to the other end of the sensor. It was found that the resulting slope difference was less than 0.002 and therefore negligible.

The sensor was calibrated before leaving the factory in Germany and therefore the only plausible reason for the incorrect calibration can be attributed to the sensor being forced out of calibration during shipping and handling especially when the sensor was sent to be soldered to the USB-sensor interface. The sensor is extremely sensitive and a small load or shock can damage the device beyond repair.

The result of the test meant that the measured values from the experimental investigations would require adjustment to render them valid.

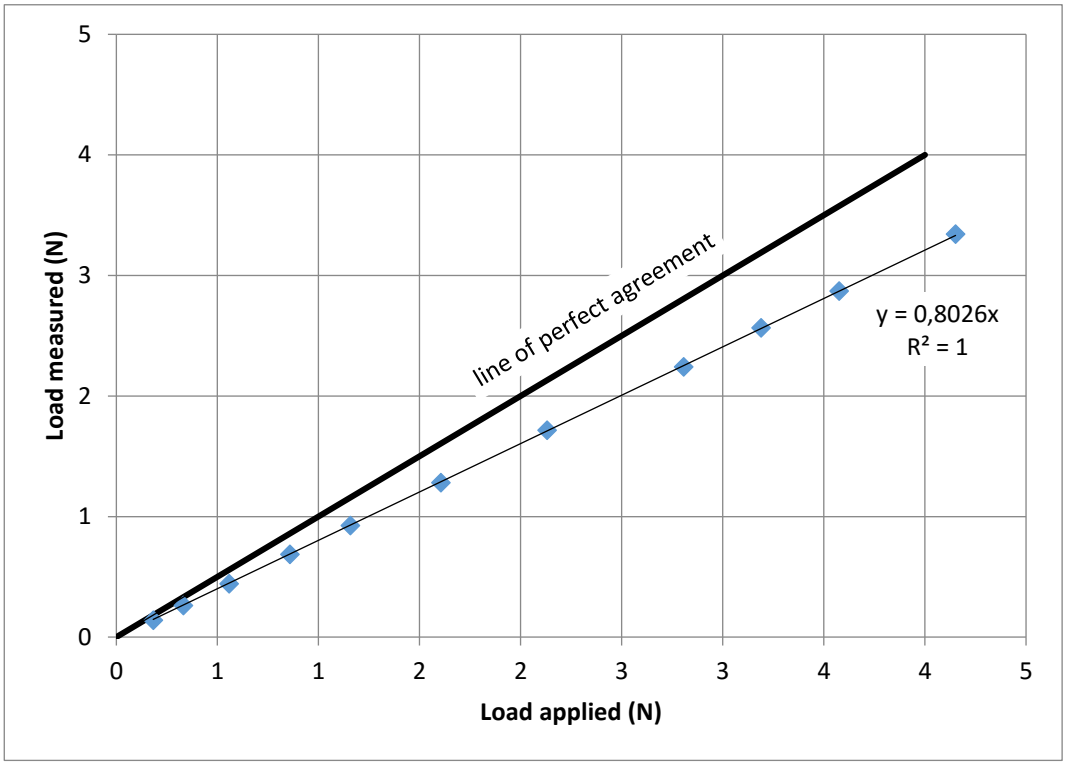

Figure 4-1: Load measured versus load applied for tension sensor.

4.1.2 Configuration 1, 2 and 3

It is clear from the calibration graphs for Configuration 1 to 3 (Figure 4-2 to Figure 4-5) that the data points are slightly further away from the line of perfect agreement than for the sensor alone. This is to be expected and is attributable to the internal friction of each system. In all three systems the friction is small.

It is interesting to note the significant difference obtained between the static (Figure 4-3) and dynamic test (Figure 4-4) results for Configuration 2, whereby the dynamic test results align closer to the line of perfect agreement. During the experimental investigation, the conditions would be dynamic due to the movement induced by vortex shedding and therefore the dynamic result would be more applicable.

During the experimental investigation, each data point was adjusted by dividing the measured value by the trendline slope for the appropriate apparatus.

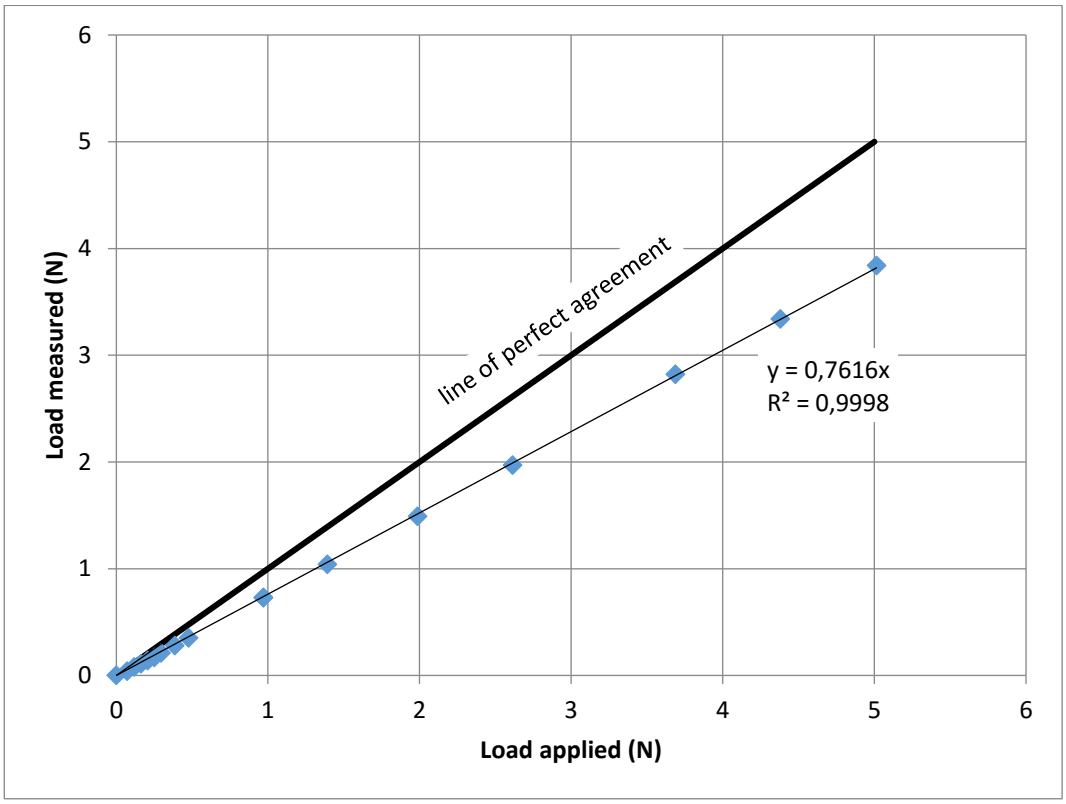

Figure 4-2: Load measured versus load applied for Configuration 1.

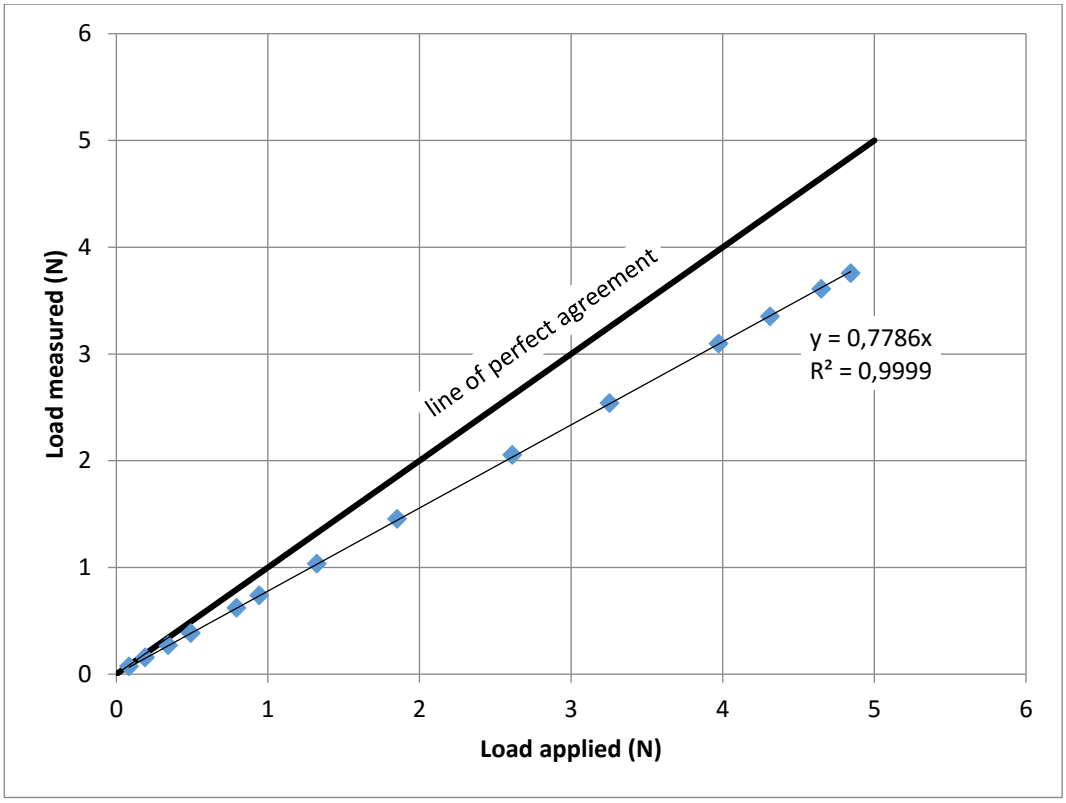

Figure 4-3: Load measured versus load applied for Configuration 2 (static).

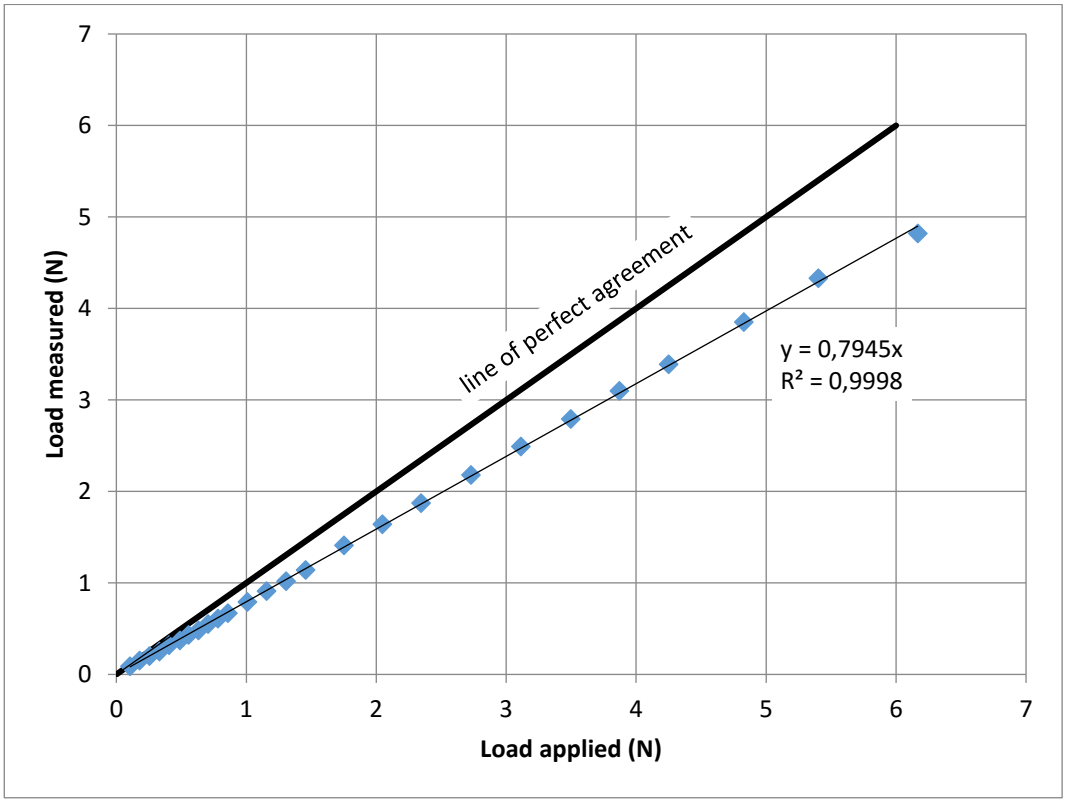

Figure 4-4: Load measured versus load applied for Configuration 2 (dynamic)

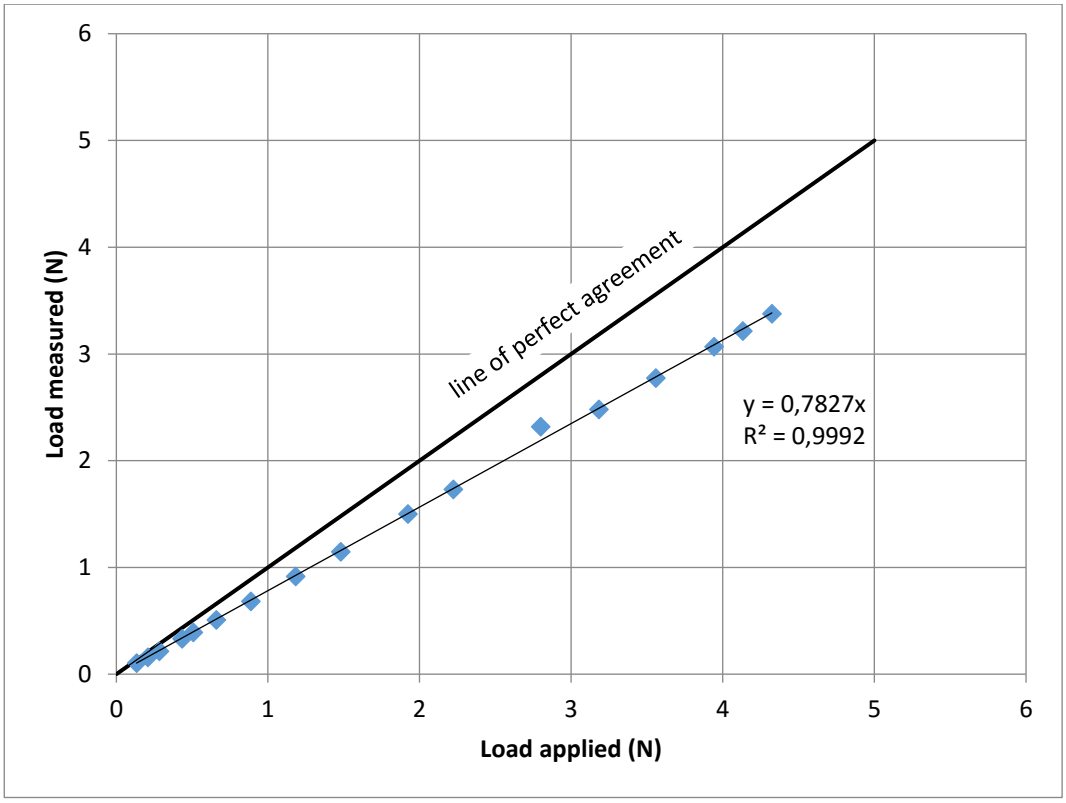

Figure 4-5: Load measured versus load applied for Configuration 3.

4.1.3 Conclusion

The tests conducted indicated that the apparatus has very little internal friction and the largest errors are because of the sensor being out of calibration. To overcome this, the measured values obtained in the experimental investigations require adjustment.

4.2 Verification tests

The verification tests were carried out to determine whether the experimental setup was producing realistic data. Therefore, experiments were conducted for a well-researched field and the data compared to a well-established relationship. The experiment was carried out for an infinitely long cylinder and the results were compared to the drag coefficient versus Reynolds number relationship.

4.2.1 Results

The graph for the drag coefficient versus Reynolds number (Figure 4-6) (which were both calculated using the local velocity) shows a good agreement between the measured values and equation (2-27) given by Cheng (2013). The graph for the drag coefficient versus Reynolds number for the case of average velocity (Figure 4-7) produces considerably higher drag coefficients, which is to be expected. The drag coefficient is inversely proportional to the velocity (equation (2-2)) and the average velocity is less than the local velocity (cylinder is far from the bed), therefore, when this lower velocity is substituted into the general drag equation a higher drag coefficient is output.

The data points are on average slightly higher than the existing relationship which can be attributed to several uncertainties, these include: -

1. The concept of an infinitely long cylinder is relative and no guidance is given as to what length to diameter ratio defines this classification. In this test the ratio is approximately 45 which is probably lower than the values used by the researchers who established the given relationship, if one considers that their experiments were carried out using a wire in a wind

tunnel (Wieselsberger, 1922 and Finn, 1953). This lower ratio may contribute to slightly higher drag forces;

2. The cylinder support frame was built from 0.5 mm thick steel sheet which was orientated with the long edge parallel to the flow to ensure the magnitude of drag it induced was negligible. Despite these efforts, the frame in contact with the flow would have had a minor contribution to the drag exerted on the cylinder and induce a slightly higher reading.
3. The length of the cylinder was sized to be as close to the side walls as possible (±2 mm gap), however the small gap permits flow and the end effects may increase the measured drag force marginally.

The degree of scatter of the data can be ascribed to the accuracy of the velocity meter that was used. The digital water velocity meter can measure the flow velocity to an accuracy of 0.01 m/s. This is relatively inaccurate and through observation, changing a velocity value by 0.01 m/s can change the drag coefficient by between ± 0.030 – 0.185 and change the Reynolds number by ± 140. This can result is a high degree of scatter and significant inaccuracies and therefore a miniature propeller meter was used in conjunction with the digital water velocity meter to more accurately determine the local velocity.

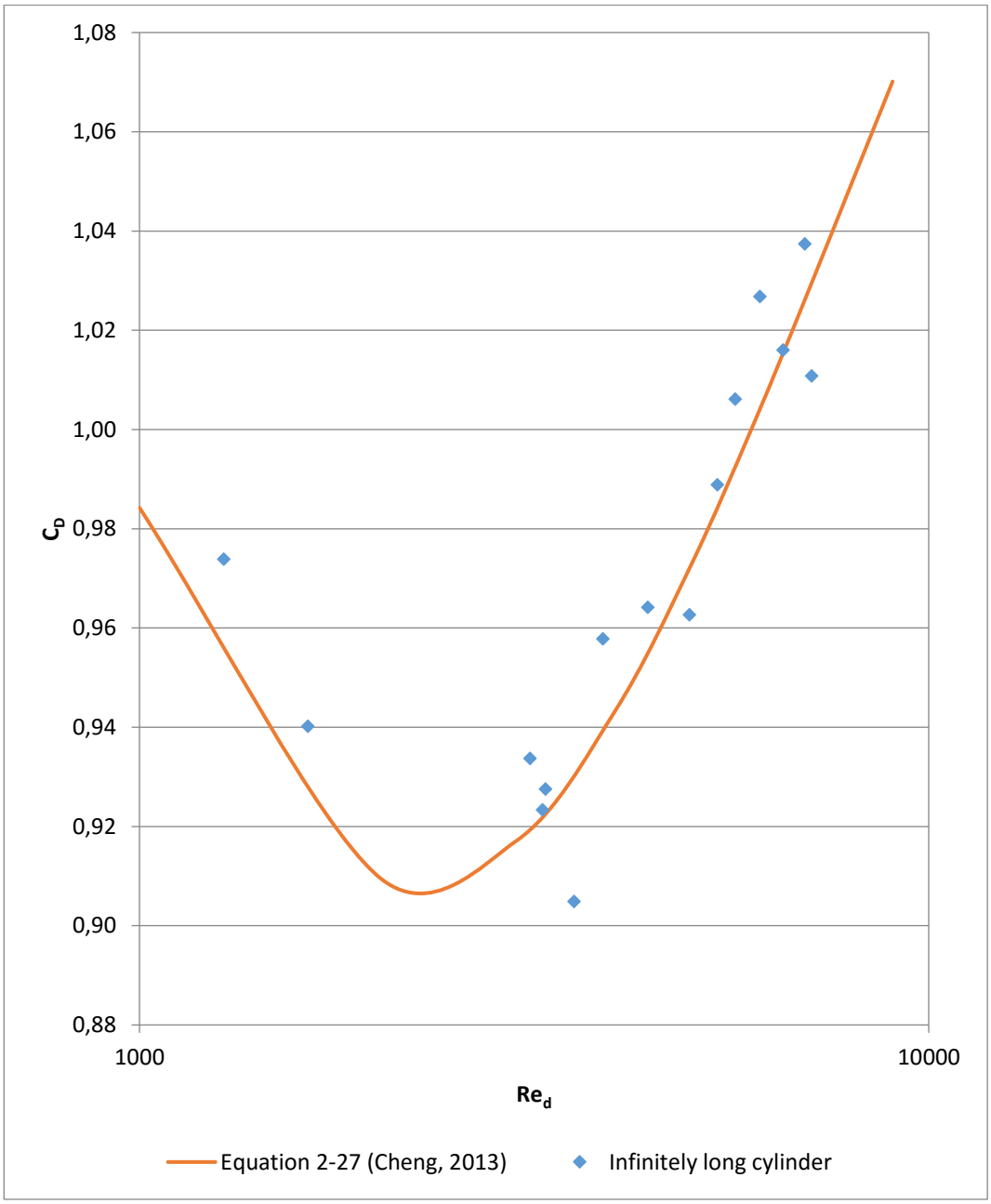

Figure 4-6: Drag coefficient vs Reynolds number for infinitely long cylinder (local velocity)

From Figure 4-8 it can be seen that the relationship between drag force and velocity squared correctly agrees with the drag equation. The relationship between drag force and Reynolds number is clearly defined in Figure 4-9.

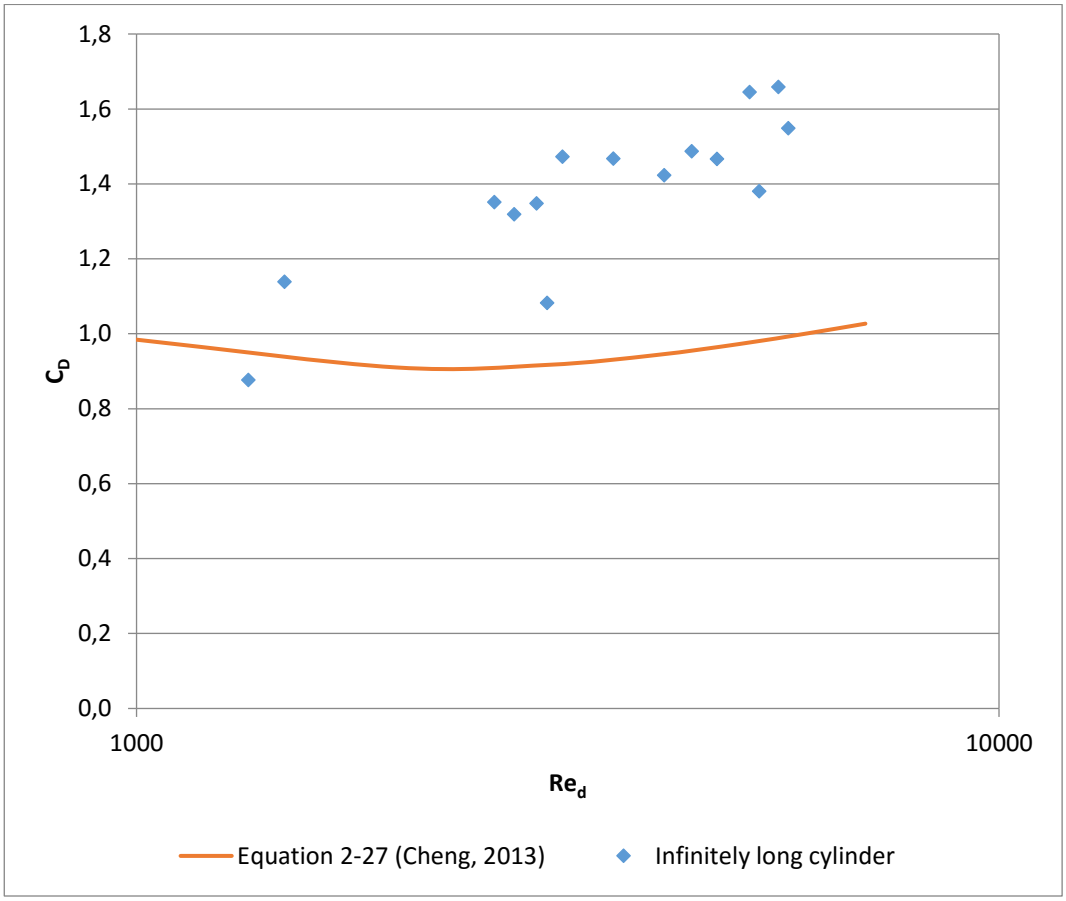

Figure 4-7: Drag coefficient vs Reynolds number for infinitely long cylinder (average velocity)

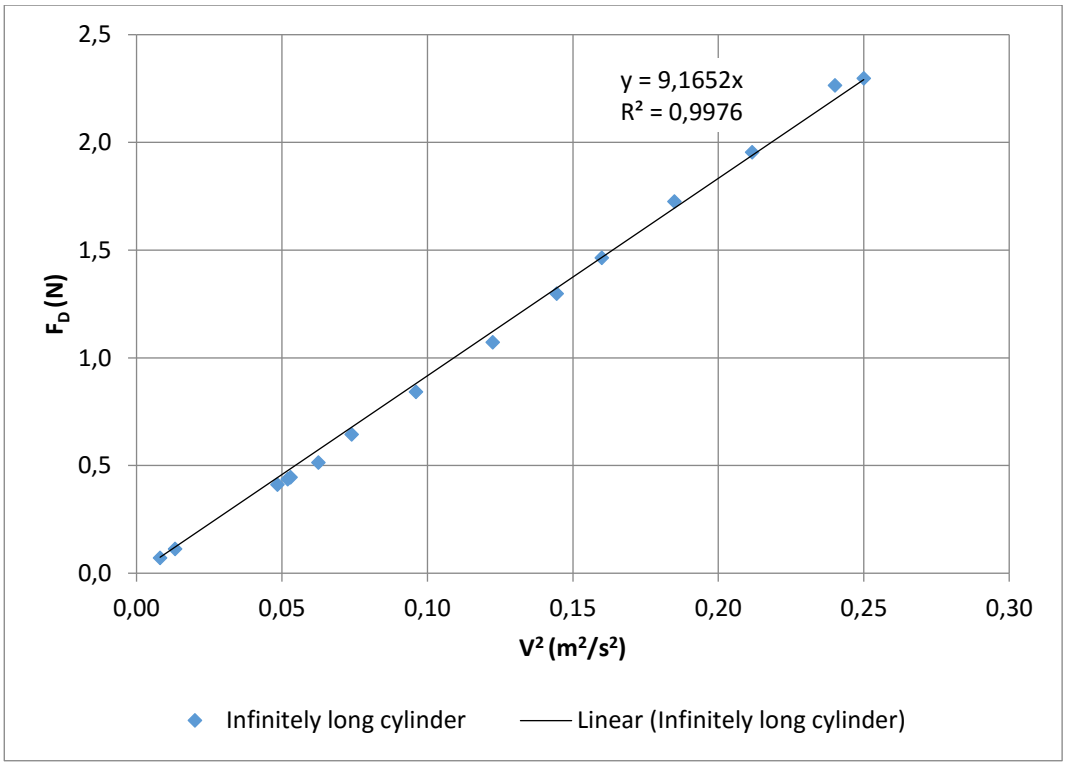

Figure 4-8: Drag force vs local velocity^2 for infinitely long cylinder

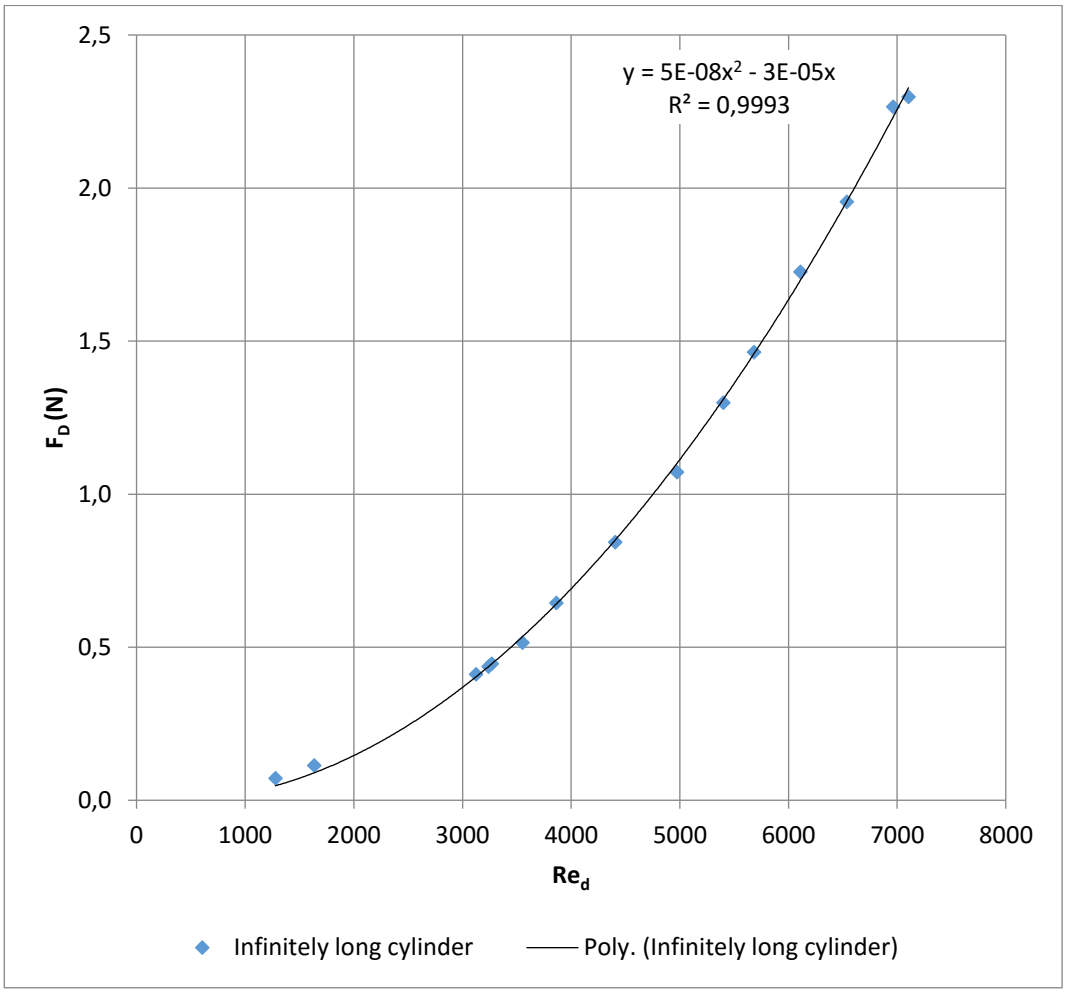

Figure 4-9: Drag force vs cylinder Reynolds number for an infinitely long cylinder

4.2.2 Conclusion

The experimental results are sufficiently accurate and provide substantial evidence that the apparatus is providing realistic readings and will therefore be suitable for determining the drag forces exerted on a given cylinder during the experimental investigations outlined in the research project.

4.3 Single circular cylinder experimental investigation

The flow around an emergent cylinder resting on the bed of a channel is complex and characterised by the occurrence of wake vortices directly downstream of the cylinder (von Kármán vortex street, Figure 4-10), horseshoe vortices at the base of the cylinder (Figure 4-11) on the upstream face and a surface roller (bow wave) at the water surface on the upstream face of the cylinder. Scant research could be

found dealing with cylinders with a low aspect ratio. In this context, this refers to cylinders where the flow depth is less than 10 times the cylinder diameter. In this experimental investigation, an attempt is made to elucidate the behaviour of an emergent circular cylinder with a low aspect ratio.



Figure 4-10:Photograph of von Kármán vortex street behind test cylinder

4.3.1 Results

The relationship between the drag coefficient and Reynolds number for a single emergent cylinder (Figure 4-12) confirms a generally good agreement to that of an infinitely long cylinder. Below a Reynolds number of ± 15 000 and above a Reynolds number of ± 30 000 the trend can be seen to deviate from the established relationship. The drag coefficients have been calculated using the general drag equation (equation (2-2)), the velocity used throughout all the calculations was the average velocity which is determined using the discharge and the full cross sectional flow area (Q/A). The reason why average velocity is used instead of local velocity (which shows better agreement) is because it would be more applicable

practically as it would be a lot more difficult and resource consuming to measure local velocities in practice.

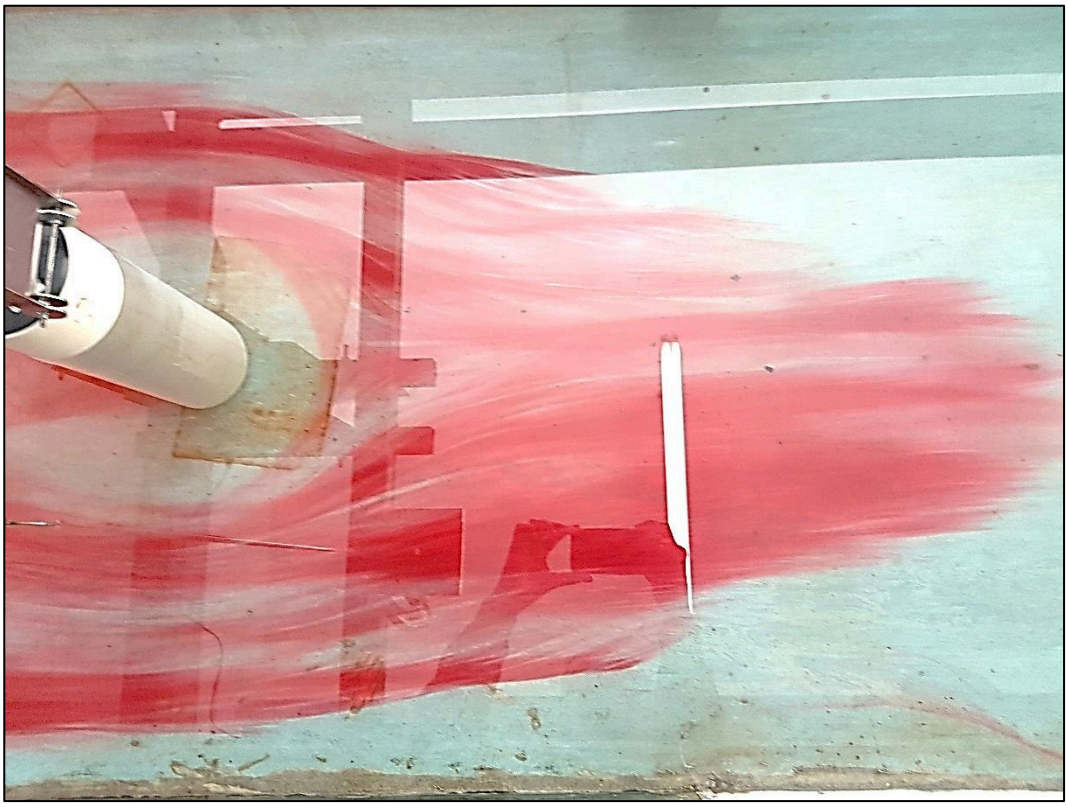

Figure 4-11: Photograph of dye being displaced in front and at the base of the cylinder by the horseshoe vortices.

As can be seen on Figure 4-12, for Reynolds numbers in excess of ± 30 000 the drag coefficient departs from the relationship defining an infinitely long cylinder. The likely reason for this departure is due to the significant local rise of the water surface on the upstream face of the cylinder as the flow velocity (and therefore Reynolds number) increases. The effect of the local water level changes suggests that the Froude number at the cylinder may influence the drag coefficient. There is also a considerable local drop in the water level on the downstream side of the cylinder. This local rise and drop in water level on the upstream and downstream sides respectively results in a substantially imbalanced hydrostatic force which then contributes to the conventional drag force in the downstream direction. The magnitude this imbalanced hydrostatic force is dependent on the flow velocity. The higher the velocity, the higher the additional force will be. The local rise of the water surface also increases the area over which the flowing water acts and further

contributes to the conventional drag force. The determination of the local rise in water surface level is complex and Fenton (2008) states “the details of such backwater problems are too complicated to be solved by conventional hydraulics or even by computational fluid mechanics in this age. It seems that the best solution is, in apparent opposition to modern tendencies, to use experiments to solve practical problems”.

From Figure 4-12, for Reynolds numbers less than ± 15 000 the trend again departs from the infinitely long cylinder relationship. For the range 6 000 to 14 000 the trend of the data points falls below that of the infinitely long cylinder. Nothing out of the ordinary was physically observed, however, the von Kármán vortex street was very apparent in this range. Many data points were collected in this range to ensure that the readings were accurate. These attempts, as shown on Figure 4-12, served to verify the initial outlier. The drag coefficients increase sharply for Reynolds numbers lower than 6 000. It is not clear why this trend occurs as the form of the trend is similar to that of the infinite cylinder which increases rapidly due to the sudden and considerable contribution of viscous drag. It may be postulated that the “large” (in other words low aspect ratio) cylinder slows the flow around the cylinder such that the boundary layer becomes more prominent around the cylinder which results in viscous drag being more prominent. From Figure 4-13 it can be seen that although the trends of the various researchers are similar, but the locations of the data points are highly variable. The current data set and those of Tanino and Nepf (2008) and Kothyari *et al* (2009) best approximate the infinitely long cylinder relationship for Reynolds numbers below 6 000. This observation may indicate that the accuracy of the apparatus becomes questionable as measurements for Reynolds numbers below ± 2 000 are obtained. Having first-hand experience using the apparatus of Madhi and Bismilla (2014), it was apparent that the data points below ±25 000 were unreliable. On improving the apparatus, the data points followed the “infinite” cylinder relationship until substantially lower Reynolds numbers. Further improvement of the apparatus further verified this observation. Using Configuration 3, the infinitely long cylinder relationship was mirrored closer.

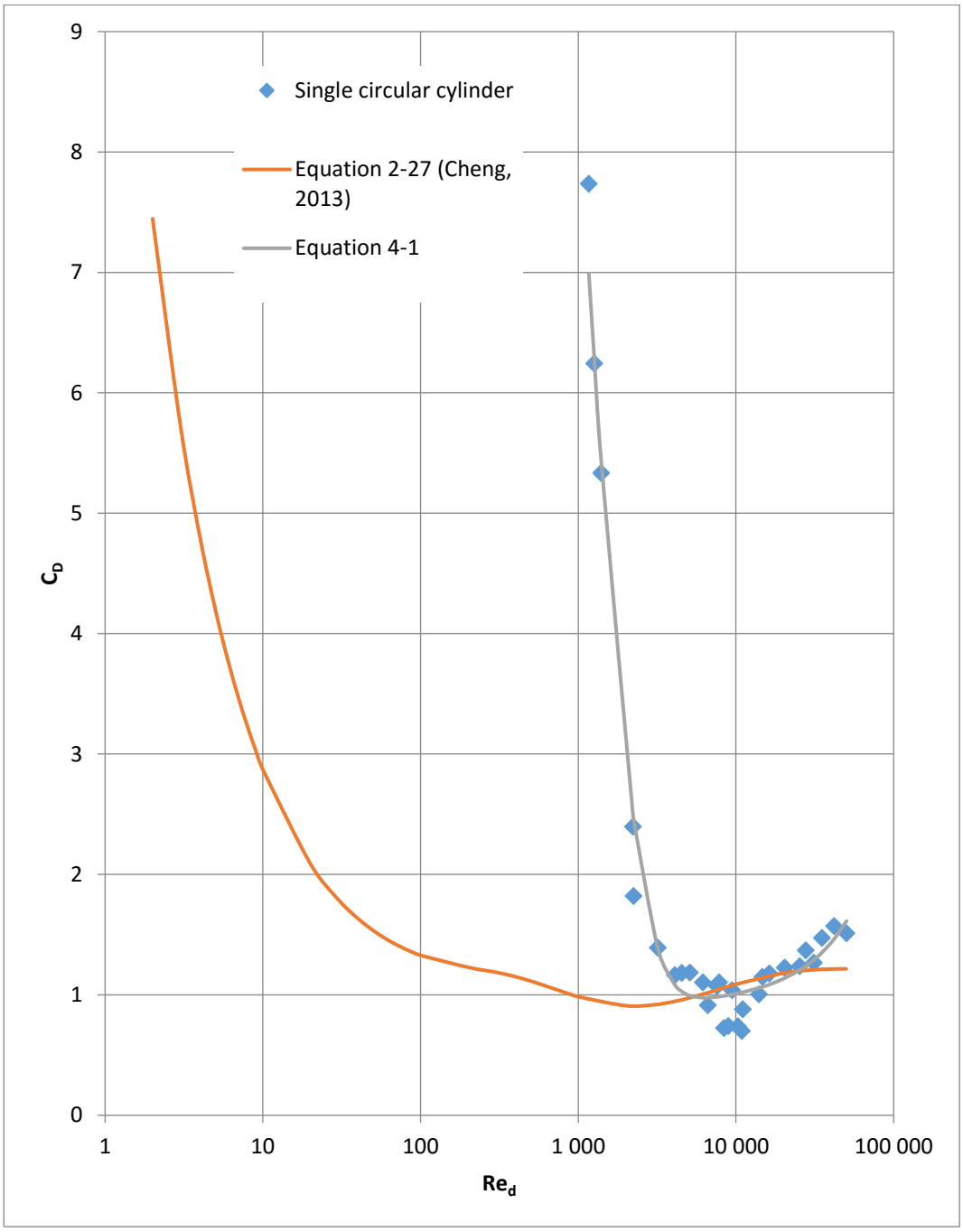

Figure 4-12:Relationship between drag coefficient and cylinder Reynolds number for a single emergent circular cylinder.

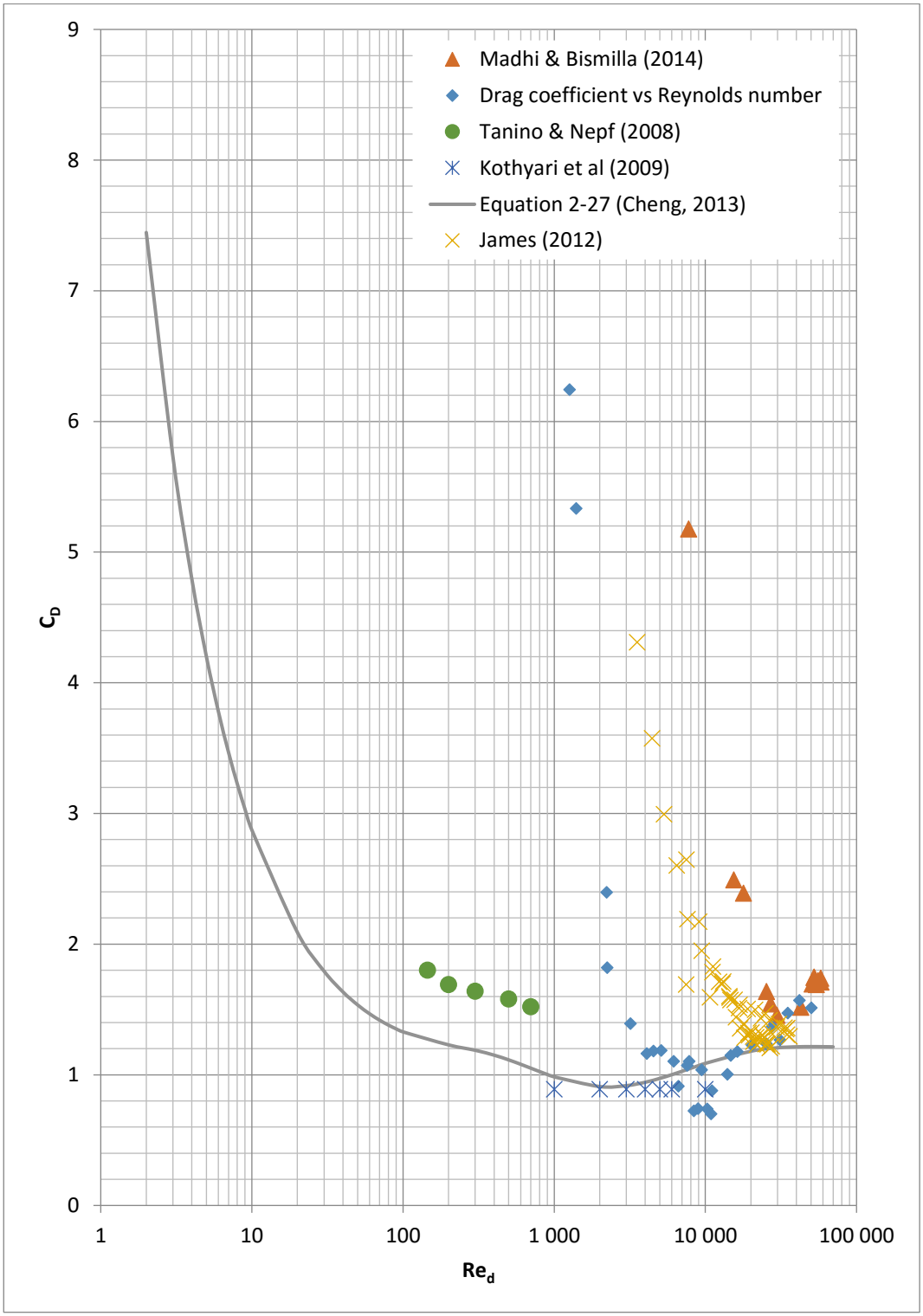

Figure 4-13: Comparison of various researchers reported data sets for drag coefficient versus cylinder Reynolds number

From Figure 4-14 the relationship between the drag force and the average velocity squared gives a reasonably good ($R^2 = 0.9345$) linear relationship which agrees with the general drag equation.

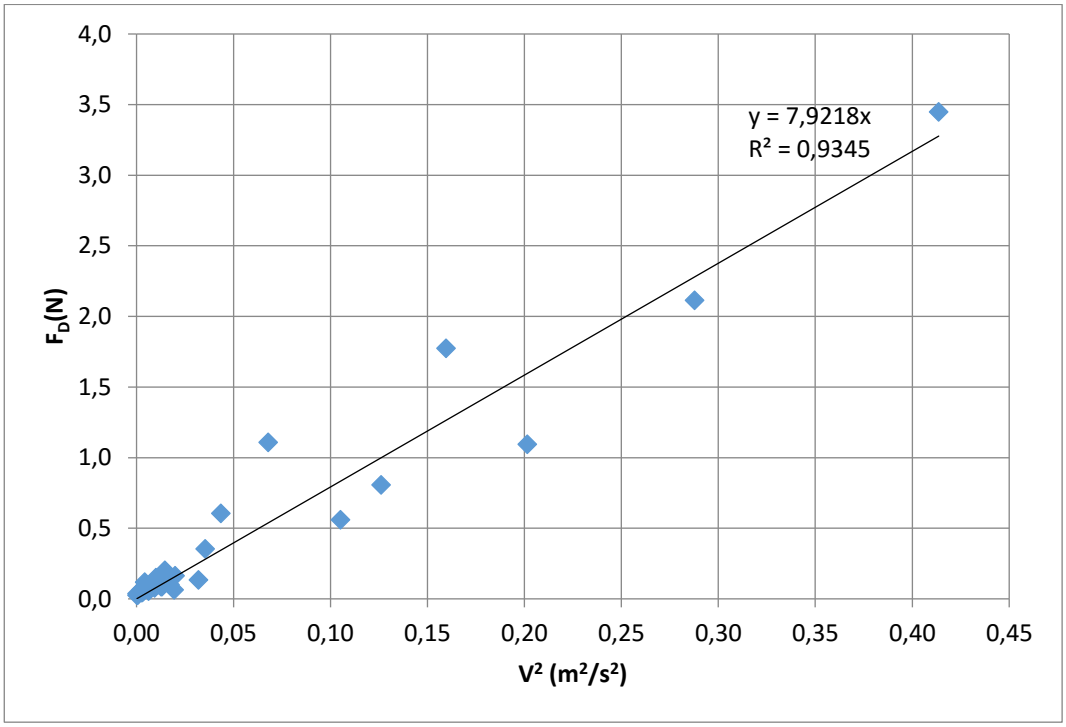

Figure 4-14: Relationship between drag force and velocity squared for a single emergent circular cylinder.

A regression analysis was performed on the data to fit an equation that could be used for practical purposes. The analysis was carried out using *MathWorks* MATLAB curve fitting toolbox analysis package. The analysis was performed for several regression functions. The function that gave the highest coefficient of correlation was then adopted.

Figure 4-15 illustrates the result of the curve fitting analysis. The curve for the data collected for this experimental investigation is described by equation 4-1, the orange line on Figure 4-15 represents this function and the coefficient of correlation is 0.9901. This curve is therefore a very good approximation of the data.

$$C_D = [9.3e^{-07}\ exp(-16.5\ x)] + [1.05\ exp(0.157\ x)] \qquad (4\text{-}1)$$

where

$$x = \frac{Re_d - \mu}{\sigma}$$

x is the normalised cylinder Reynolds number
μ is the mean of the data = 1.34e+04
σ is the standard deviation of the data = 1.29e+04

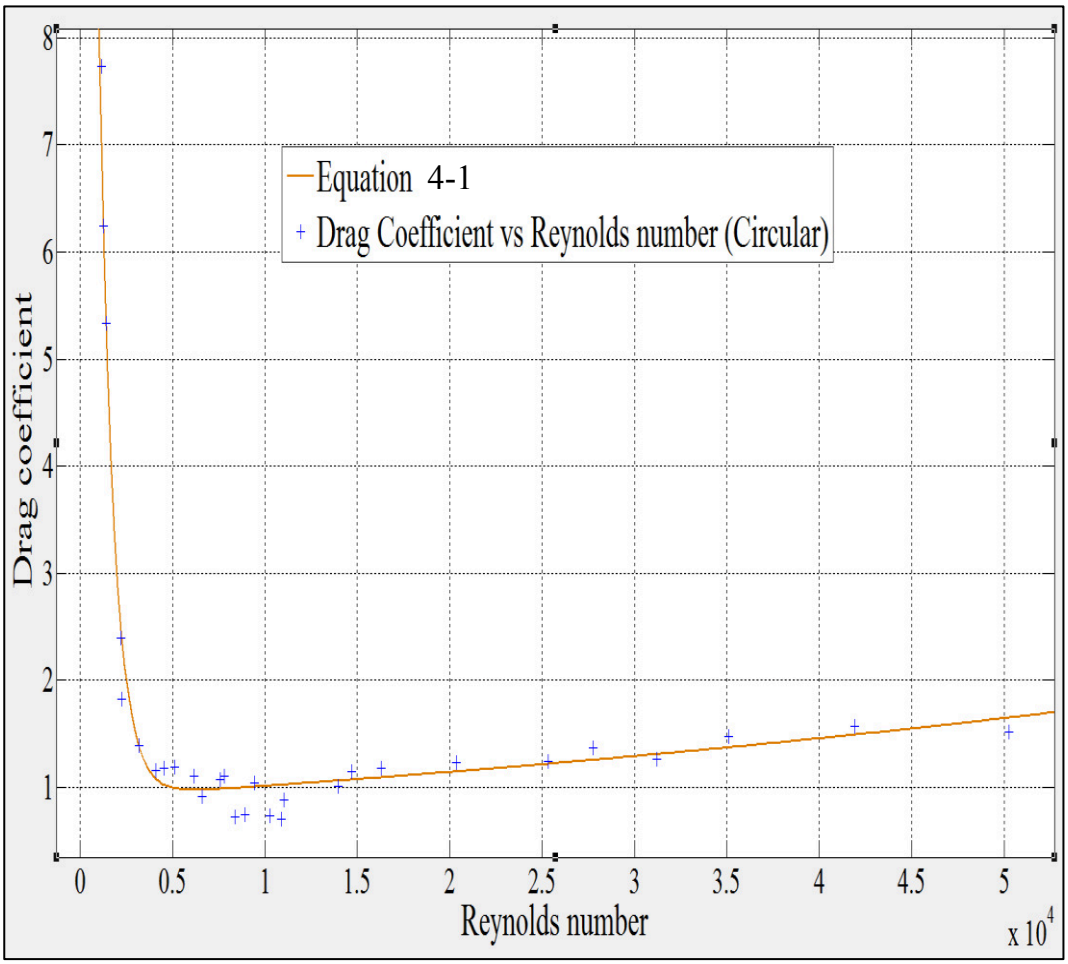

Figure 4-15: Single circular cylinder curve fitting.

4.3.2 Conclusion

The experimental investigation yielded a relationship between drag coefficient and Reynolds number which displays common features to that of an infinitely long cylinder. The new relationship departs from the "infinite" cylinder above a Reynolds number of ± 30 000 and this has been postulated to be as a result of local water surface distortions. These water distortions may suggest the Froude number at the cylinder may have an influence on the drag coefficient. The relationship also departs below Reynolds numbers of ± 6 000 and is proposed to be because of either the large frontal area slowing the local flow down sufficiently for the boundary layer to become more significant or it may be due to measurement errors which may have been brought about by taking readings close to the lower limit of the tension sensor's range.

4.4 Single square cylinder experimental investigation

Circular cylinders are common obstacles found in open channel flow. These are in the form of vegetation stems, trees, rounded rocks, piles and pillars to name a few. Square sharp edged objects are also found in water channels in the form of straight edged rocks, columns, piles and pillars. It is important to distinguish between the various shapes encountered to accurately determine the influence of the objects on the flow.

4.4.1 Results

From Figure 4-16 the data points are significantly higher than that of an infinitely long circular cylinder. This was expected. The flat faces and sharp edges of the square cylinder promote higher magnitudes of form drag due to the boundary layer rapidly dissipating and the substantial wake zone that is created downstream of the cylinder. During the experimental investigation it was observed that, in comparison to the circular cylinder, the square cylinder induced a more prominent local water level rise and drop on the upstream and downstream sides respectively. This contributed to the drag force through the same mechanism as discussed for circular cylinders, however, the contribution is greater in this case. For Reynolds numbers higher than ± 20 000, the drag force fluctuated greatly and inconsistently which made it difficult to determine a value for the drag force. For this reason, only a small number of data points were obtained in this region.

An interesting and unexpected result is observed in Figure 4-17 and Figure 4-18. The respective coefficients of determination suggest that better agreement is obtained with the relationship between drag force and average flow velocity (R^2 = 0.8886) than that which is obtained with the relationship between drag fore and average flow velocity squared (R^2 = 0.7535). This is contradictory to the general drag equation which states that the drag force is proportional to the velocity squared. Wilson *et al.* (2010) made a similar observation when conducting an experimental investigation for the drag coefficient of large trees. Although the difference isn't

very big, it is still an observation worth further investigation. More data needs to be collected, especially for velocities above 0.05 m/s to confirm this observation.

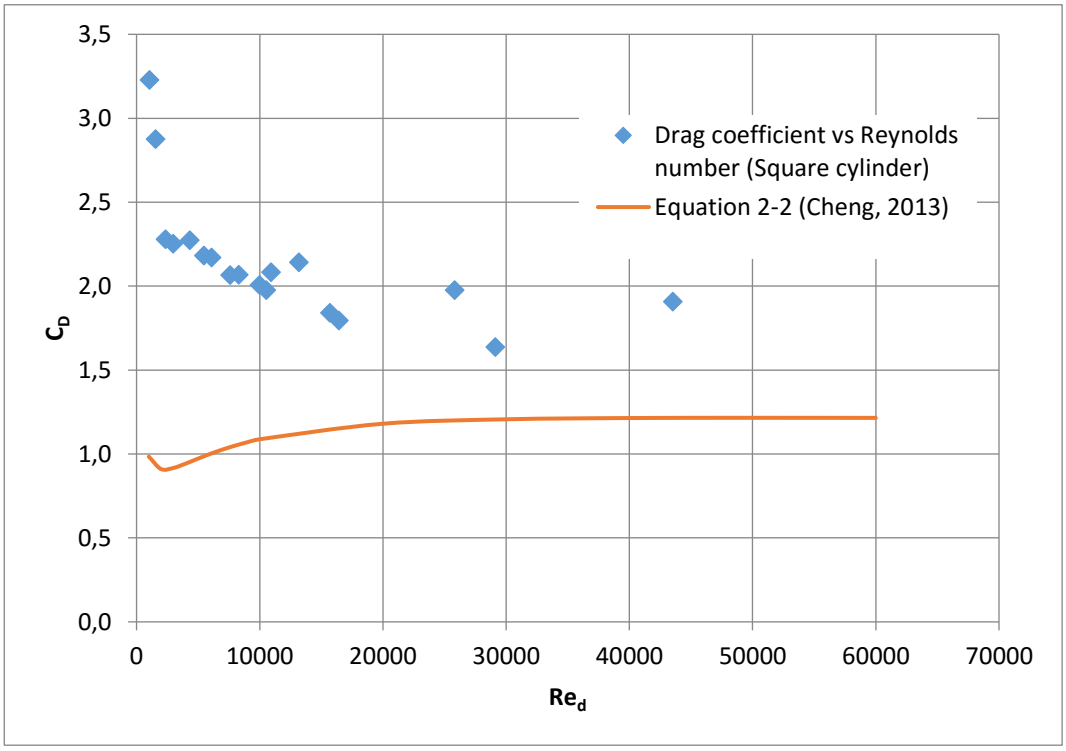

Figure 4-16: Relationship between drag coefficient and cylinder Reynolds number for a square cylinder.

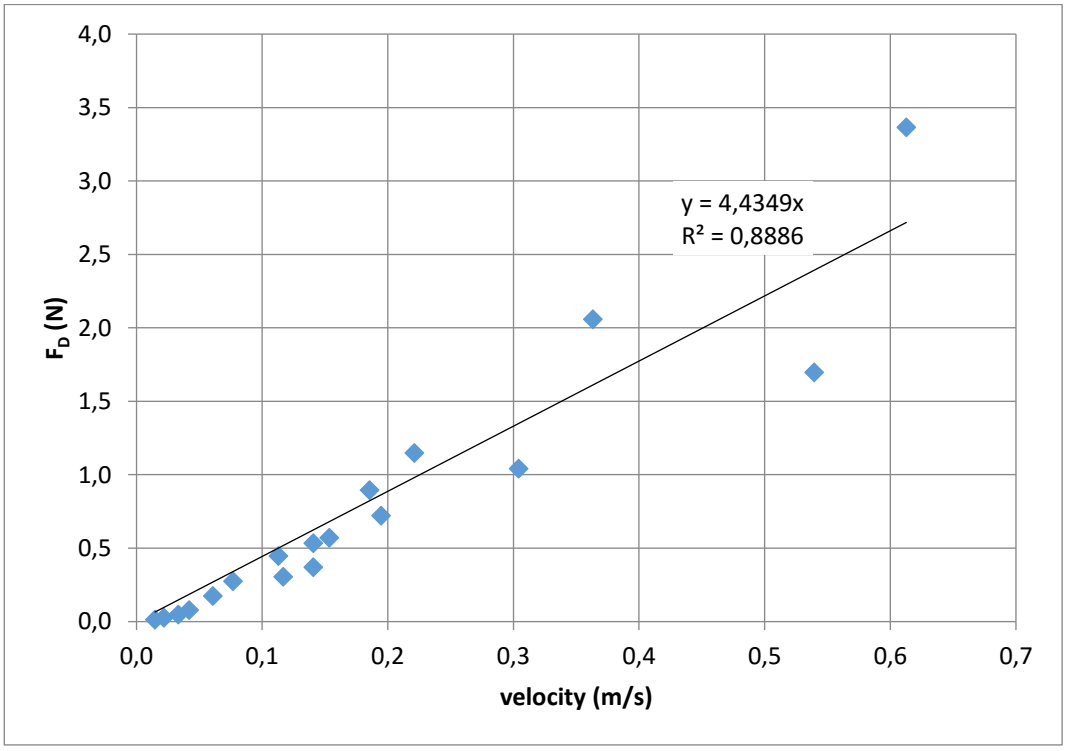

Figure 4-17: Relationship between drag force and average flow velocity for a square cylinder.

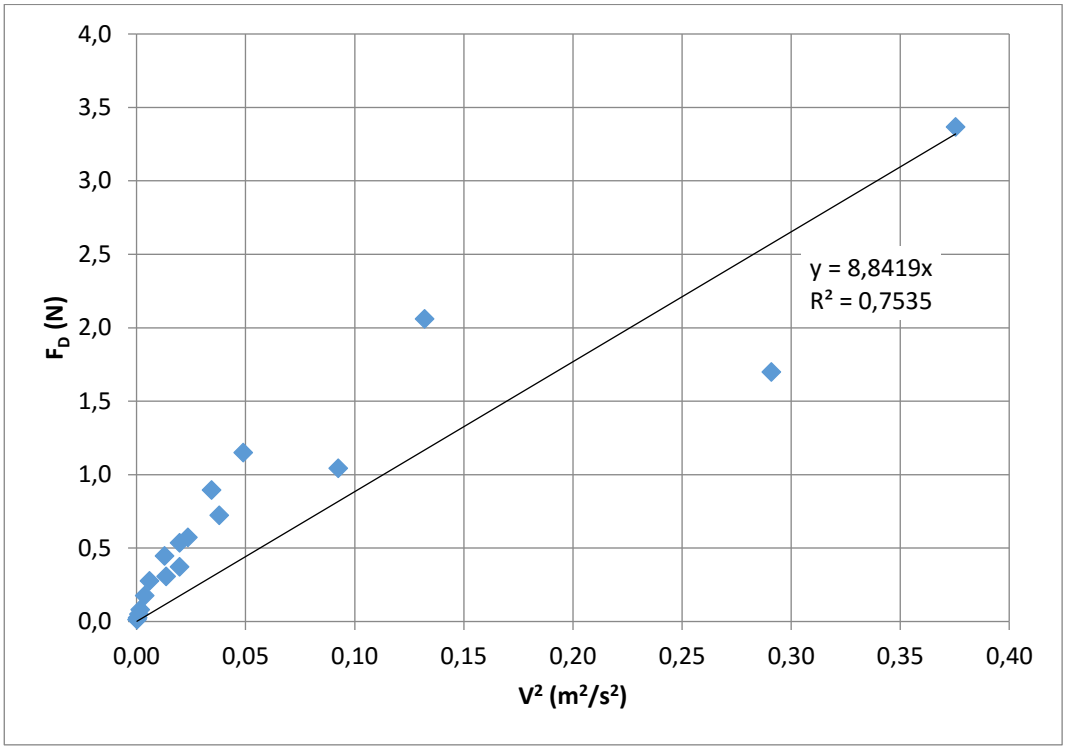

Figure 4-18: Relationship between drag force and average flow velocity squared for a square cylinder.

As before a regression analysis was carried out on the data. Figure 4-19 illustrates the result of the curve fitting analysis. The curve for the data collected for this experimental investigation is described by equation (4-2), the orange line on Figure 4-19 represents this function and the coefficient of correlation is 0.9233. This curve is therefore a very good approximation of the data. One of the data points (red dot) was deemed to be a distant outlier and was excluded from the regression analysis.

$$C_D = [3.23\ exp(-0.001\ Re_d)] + [2.12\ exp(-3.43e^{-06}\ Re_d)] \qquad (4\text{-}2)$$

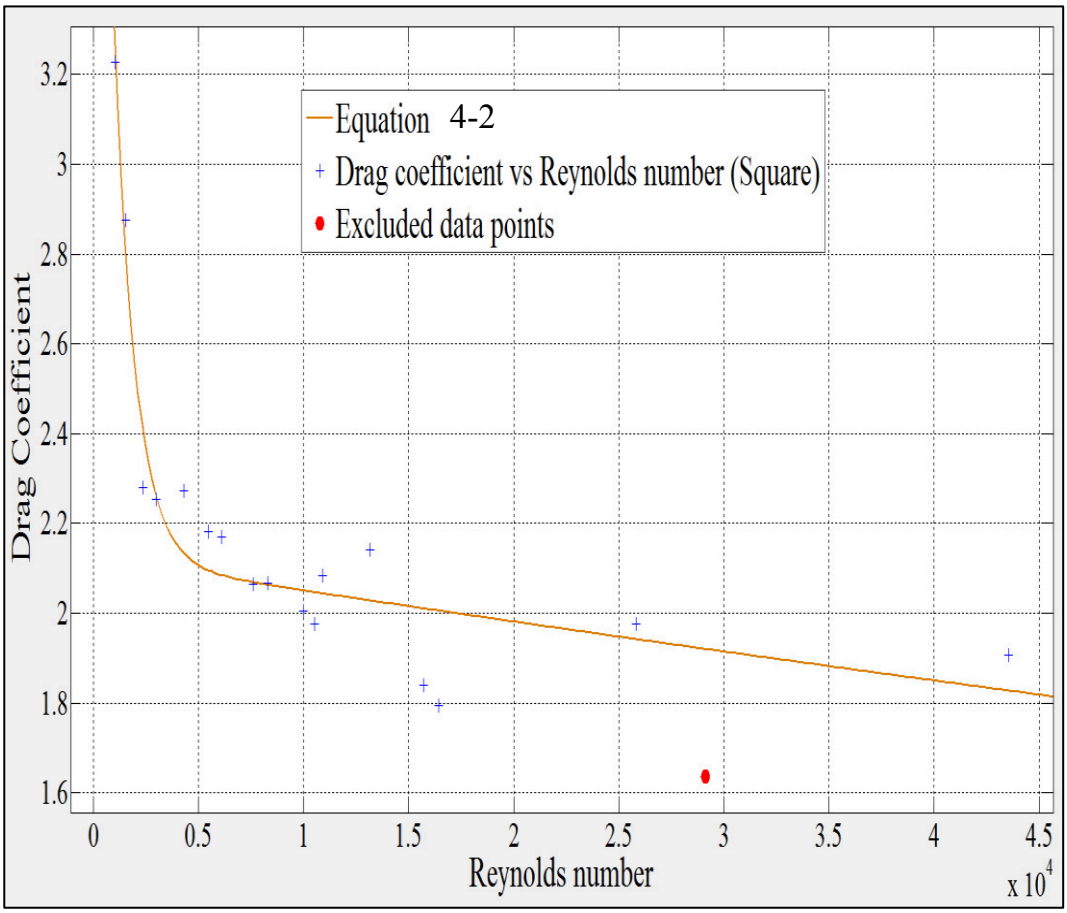

Figure 4-19: Single square cylinder curve fitting.

4.4.2 Conclusion

The experimental investigation illustrated the considerable difference between circular and square shaped obstacles in a channel. It proves that it is important to distinguish between different shapes when carrying out an analysis relating to the impact of the channel's physical attributes on the flow characteristics. As expected, the drag coefficients for square objects are substantially larger than those for circular objects. Interestingly the results suggest that for square cylinders it may be more accurate to remove the squared term from the velocity in the drag equation. This should be further investigated by obtaining more data points for higher flow velocities. The drag coefficients for circular cylinders exceed square cylinders for Reynolds numbers below ± 1 500 which most likely serves as further evidence that the low Reynolds number data points for the circular cylinder are inaccurate.

4.5 Single diamond cylinder experimental investigation

Diamond shaped obstacles as with square obstacles occur in the form of rocks, piles and pillars. The shape of the diamond may be similar or identical to the square, however the orientation with respect to the flow is what defines the shape. The orientation induces vastly different drag forces to the square and circular cylinders and therefore requires independent consideration.

4.5.1 Results

It is evident from Figure 4-20 that the trend of the data is significantly higher than that of an infinitely long circular cylinder. The sharp projecting edge of the diamond cylinder promote higher magnitudes of form drag due to the boundary layer rapidly dissipating and the widespread wake zone that is created downstream of the cylinder. During the experimental investigation it was observed that the diamond and square cylinders induced a similar local water level rise on the upstream side, however the diamond shape caused a larger drop in the local water surface on the downstream side. This contributes to the drag force through the same mechanism as discussed for circular cylinders, however, the contribution is far greater in this case. Figure 4-20 displays very scattered data which gives an indication of the highly unstable drag forces that were being measured. This instability is a result of the highly turbulent wake zone induced behind the cylinder. For Reynolds numbers higher than ± 10 000, the drag force fluctuated violently and inconsistently which made it difficult to determine a value for the drag force. For this reason, only a small number of data points were obtained in this region.

A similar observation to that made for the square cylinders is apparent for the diamond cylinders as illustrated by Figure 4-21 and Figure 4-22. The velocity rather than the velocity squared results in a better agreement.

Figure 4-24 illustrates the comparison between the circular, square and diamond shaped cylinders. The diamond cylinder trend roughly resembles the square

cylinder trend over the gathered range. The diamond drag coefficients are generally 80-100% larger than the square drag coefficients for the same Reynolds numbers.

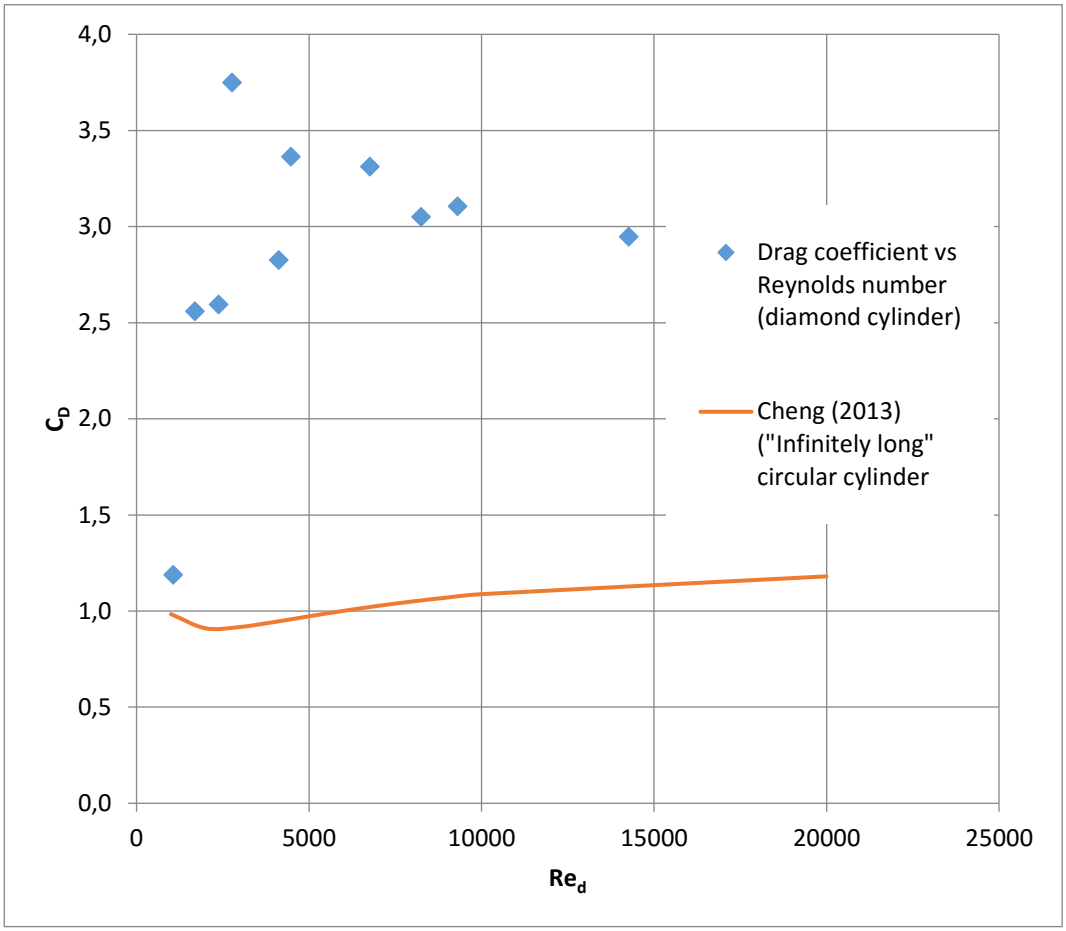

Figure 4-20: Relationship between drag coefficient and cylinder Reynolds number for a diamond cylinder.

As before a regression analysis was carried out on the data. Figure 4-23 illustrates the result of the curve fitting analysis. The curve for the data collected for this experimental investigation is described by equation (4-3), the orange line on Figure 4-23 represents this function and the coefficient of correlation is 0.9528. This curve is therefore a very good approximation of the data. Three of the data points (red dots) were deemed to be distant outliers and were excluded from the regression analysis.

$$C_D = [3.08\, exp(-0.00073\, Re_d)] + [3.44\, exp(-1.11e^{-05}\, Re_d)] \qquad (4\text{-}3)$$

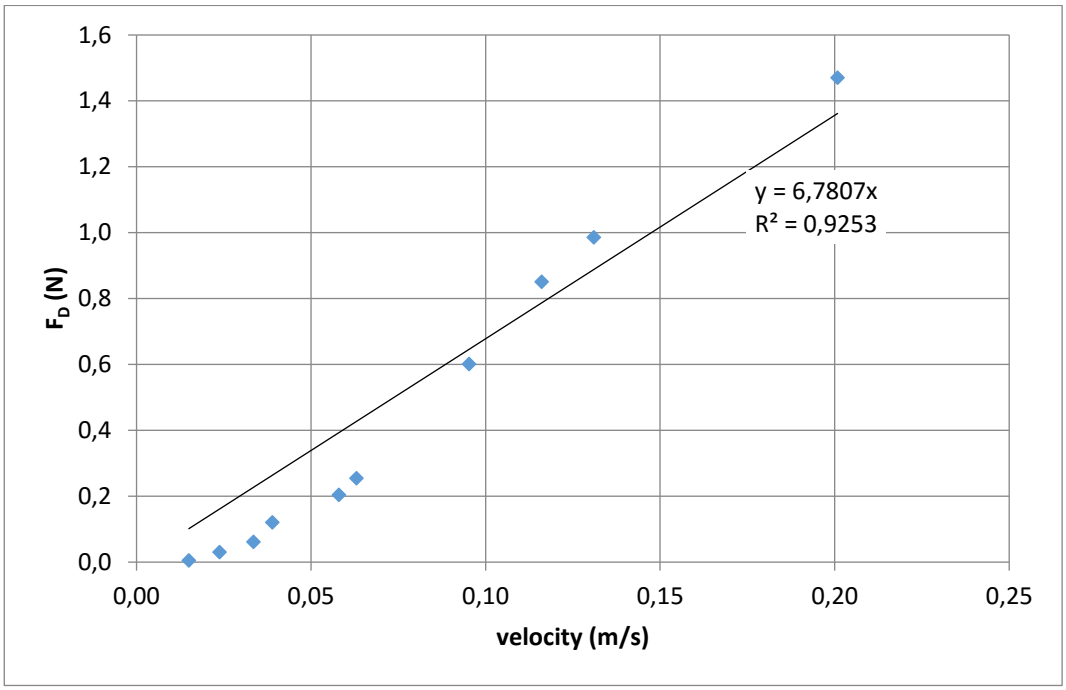

Figure 4-21: Relationship between drag force and average flow velocity for a diamond cylinder.

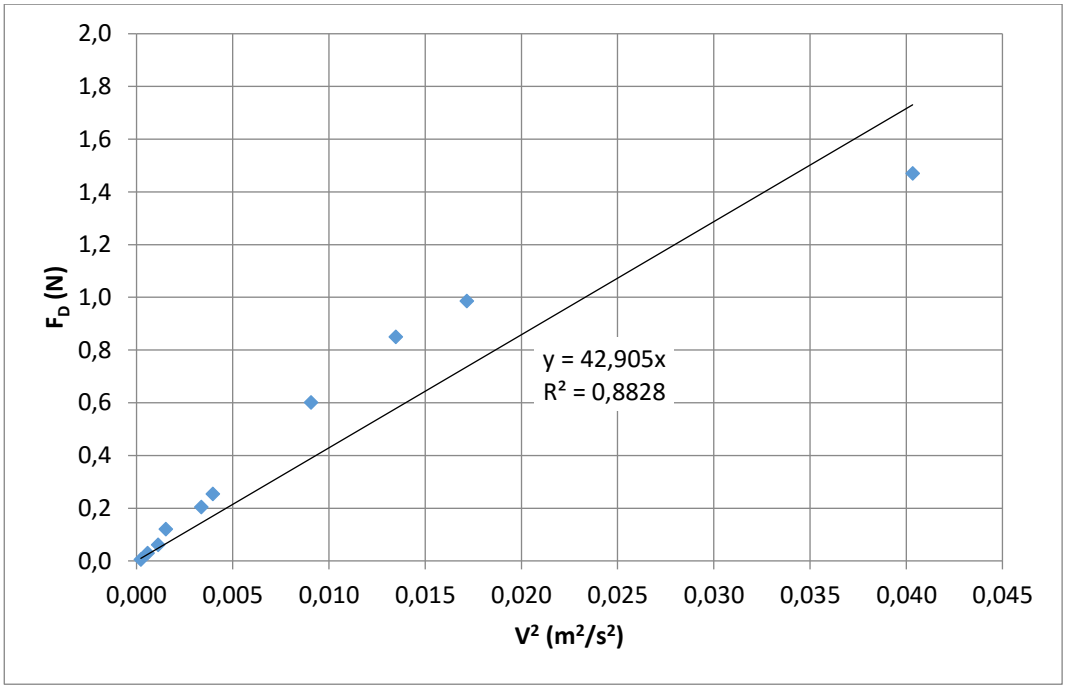

Figure 4-22: Relationship between drag force and average flow velocity squared for a diamond cylinder.

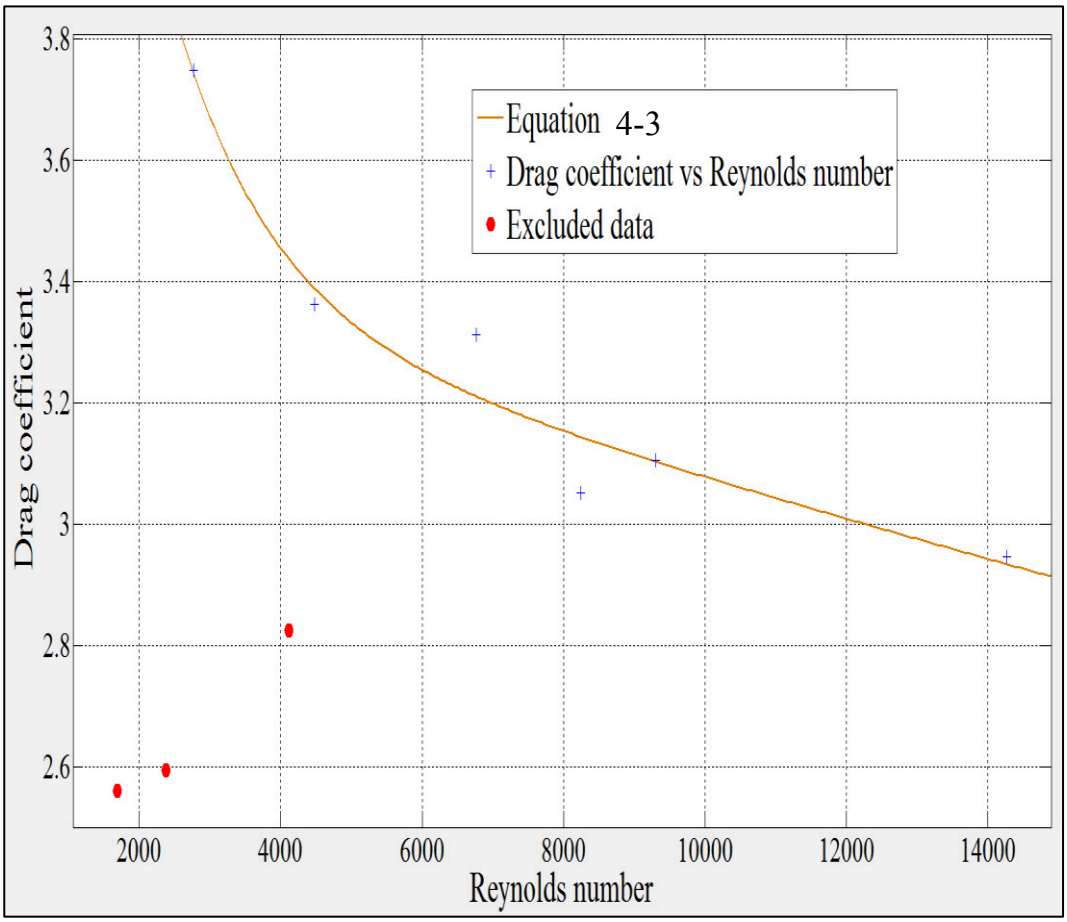

Figure 4-23: Single diamond cylinder curve fitting.

Figure 4-24 illustrates the comparison between the circular, square and diamond shaped cylinders. The square cylinder trend follows a similar form to that of the circular cylinders. The greatest difference between the circular and square drag coefficients occurs between Reynolds numbers of ± 1 500 and ± 15 000 where the magnitude of the square drag coefficients is between 20 – 110% larger than those of the circular cylinders for the same Reynolds number. Above ± 15 000 the difference between the magnitude of the coefficients becomes noticeably smaller. For Reynolds numbers below ± 1 500 the form of the trend increases rapidly in a similar manner to that of the circular cylinder. It is apparent from Figure 4-24 that below Reynolds numbers of ± 1 500 the drag coefficient for the circular cylinder begins to exceed the values of the square cylinder. It is not clear why this is the case and may once again suggest that the low Reynolds number data points for the circular cylinder are not accurate.

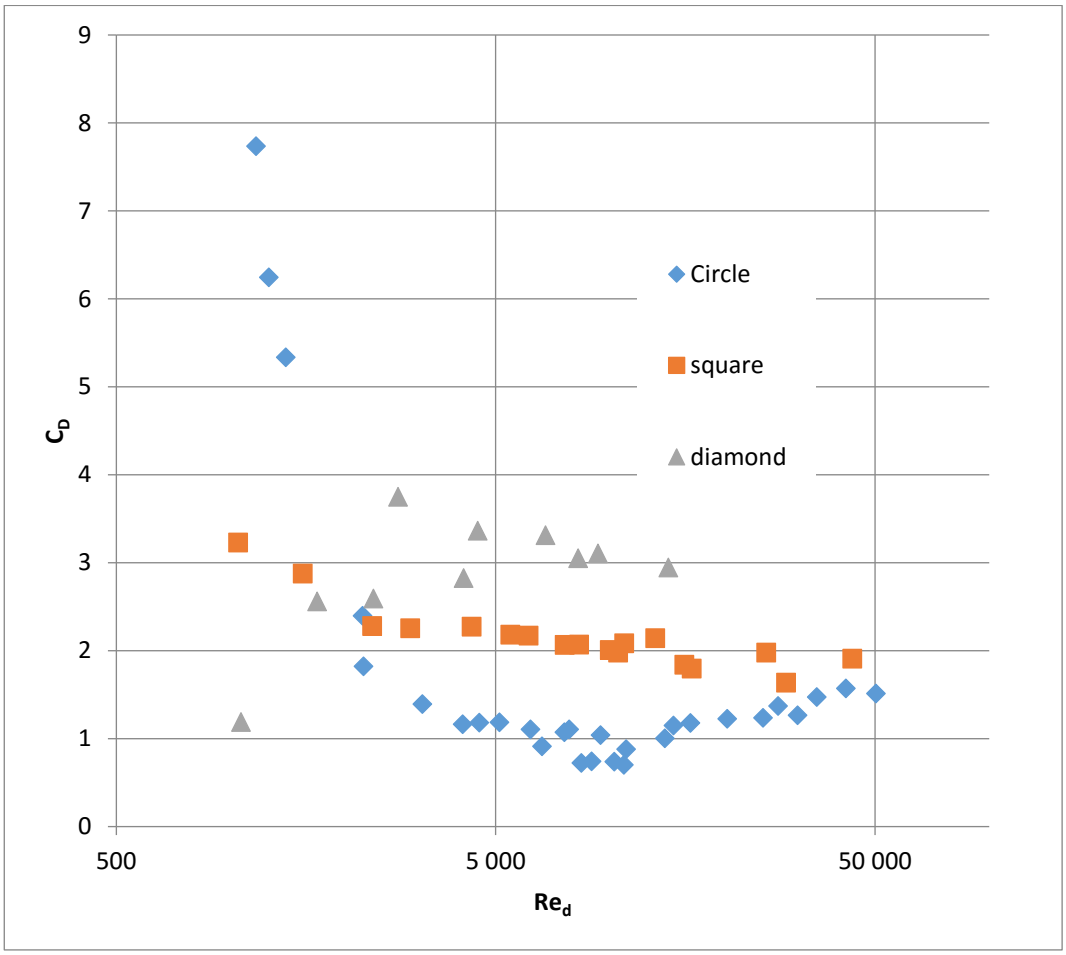

Figure 4-24: Comparison of drag coefficient vs cylinder Reynolds number relationships for circular, square and diamond shaped cylinders.

4.5.2 Conclusion

The experimental investigation illustrated the considerable difference between circular, square and diamond shaped obstacles in a channel. It proves that it is important to distinguish between different shapes when carrying out an analysis relating to the impact of the channels physical attributes on the flow characteristics. The drag coefficients for diamond shapes are substantially larger than those for square and circular objects. Interestingly the results suggest that for diamond cylinders, as with square cylinders, it may be more accurate to remove the squared term from the velocity in the drag equation. This should be further investigated by obtaining more data points for higher flow velocities.

4.6 Multiple circular cylinder experimental investigation

The analysis of single obstacles in isolation would typically apply to cases where the characteristics of the local impacts of the object on the flow are required or in cases where the size of the obstacle is large relative to the channel and will therefore have a considerable influence on the flow characteristics for long distances. It is however more common to find multiple obstacles in a channel. The obstacles are usually vegetation, trees, rocks, piers and columns etc. Several researchers (Cheng 2013, Kothyari *et al*. 2009, Ishikawa *et al*. 2000, James *et al*. 2004, Tanino and Nepf 2008) have carried out numerous experimental investigations in an attempt to quantify the drag exerted on a single cylinder surrounded by multiple cylinders. The different researchers had varying degrees of success and each have developed unique methods for addressing the subject. Most the research has focussed on determining the drag characteristics of vegetation, where the diameter of the stems is substantially smaller than the flow depth. Little attention has been afforded multiple cylinders where the flow depth is less than 10 times the cylinder diameter.

The objective of this experimental investigation is to study the influence of multiple cylinders surrounding a single cylinder in terms of the drag force. This was done by placing cylinder configurations with varying areal densities around the single cylinder and measuring the drag force on the cylinder under varying flow conditions. The pattern used in the investigation was kept constant, as was the cylinder spacing perpendicular to the flow direction.

4.6.1 Results

As illustrated in Figure 4-25, Figure 4-28, Figure 4-31 and Figure 4-34 the drag coefficients are larger in magnitude than those for an infinitely long cylinder for the same Reynolds numbers over the experimental range. The drag coefficients and Reynolds numbers were both calculated using the average flow velocity (discharge / total flow area) which gives higher drag coefficients than that which would be obtained if the actual velocity (calculated by considering the reduced flow volume due to the volume occupied by the cylinders) was used. Average flow velocity is used as it would have more practical relevance when being used in the field.

It is unclear what physical mechanism causes the increased drag force for the multiple cylinder condition. The results are in contradiction to the results of Nepf (1999) who stated that the cylinder surrounded by other cylinders would attain a lower drag coefficient than that of the isolated cylinder due to the "sheltering" effect described by Raupach (1992). The explanation provided by Nepf for the lower drag coefficient is due to two properties of the wake created by the upstream cylinders. The two properties are: -

1. The cylinder under consideration will experience a lower impact velocity due to the velocity reduction in the wake;
2. The turbulence induced by the wake delays the point of separation at the cylinder under consideration. This induces a lower pressure differential between the upstream and downstream side of the cylinder and therefore less drag.

4.6.1.1 Combination 1 (λ = 0.033)

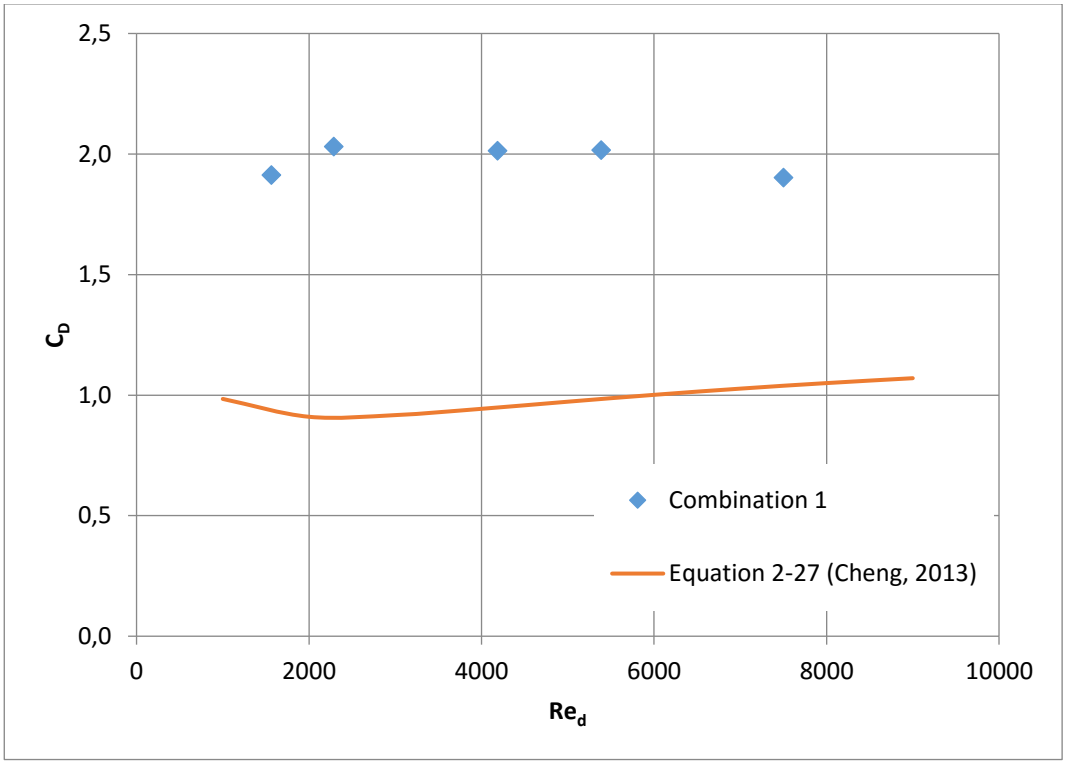

Figure 4-25: Relationship between drag coefficient and cylinder Reynolds number for Combination 1

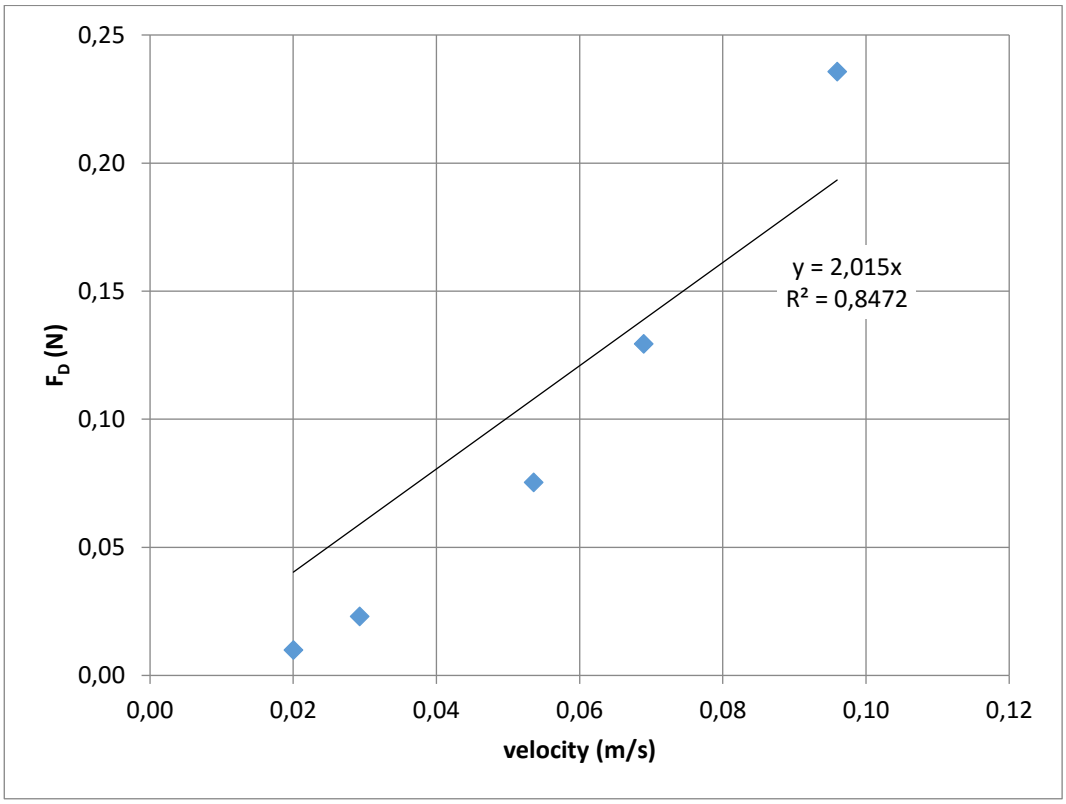

Figure 4-26: Relationship between drag force and average flow velocity for Combination 1

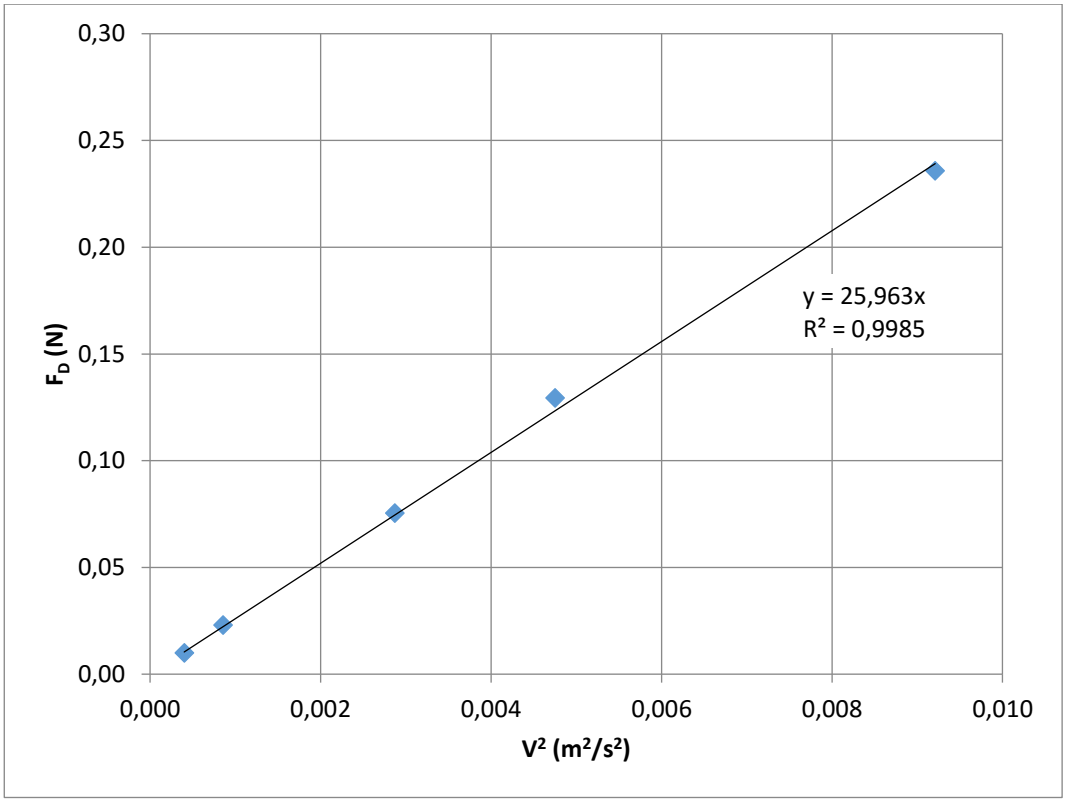

Figure 4-27: Relationship between drag force and average flow velocity squared for Combination 1

4.6.1.2 Combination 2 (λ = 0.065)

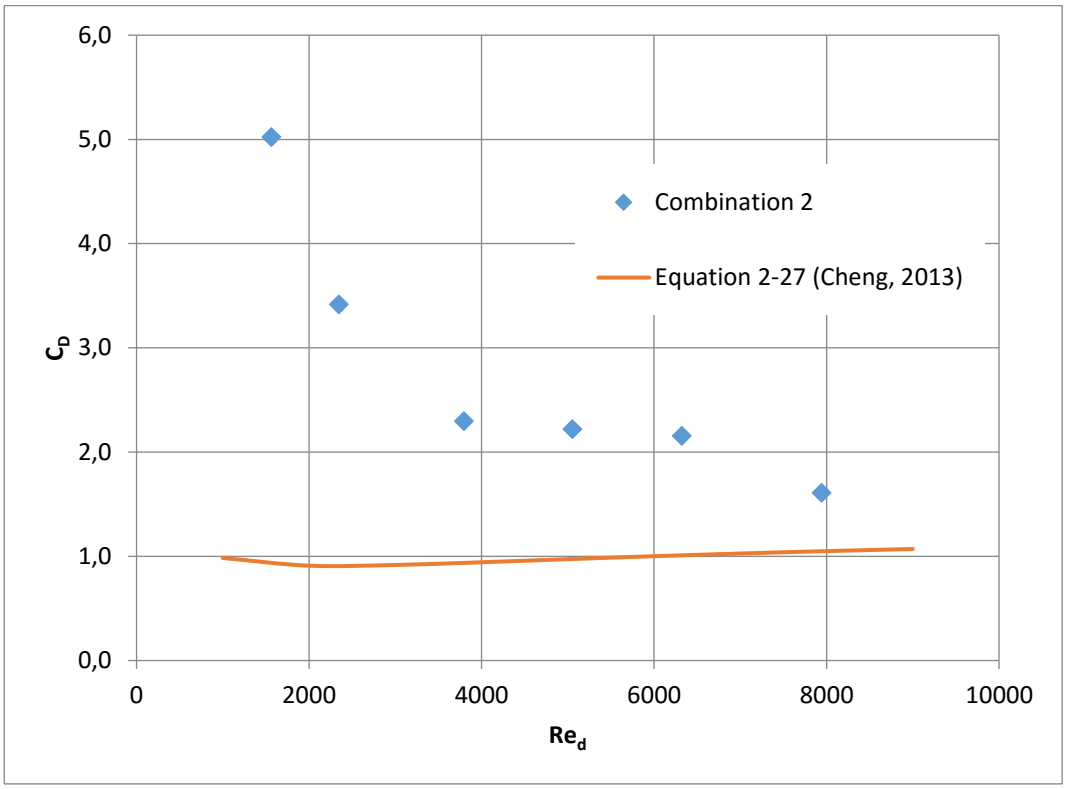

Figure 4-28: Relationship between drag coefficient and cylinder Reynolds number for Combination 2

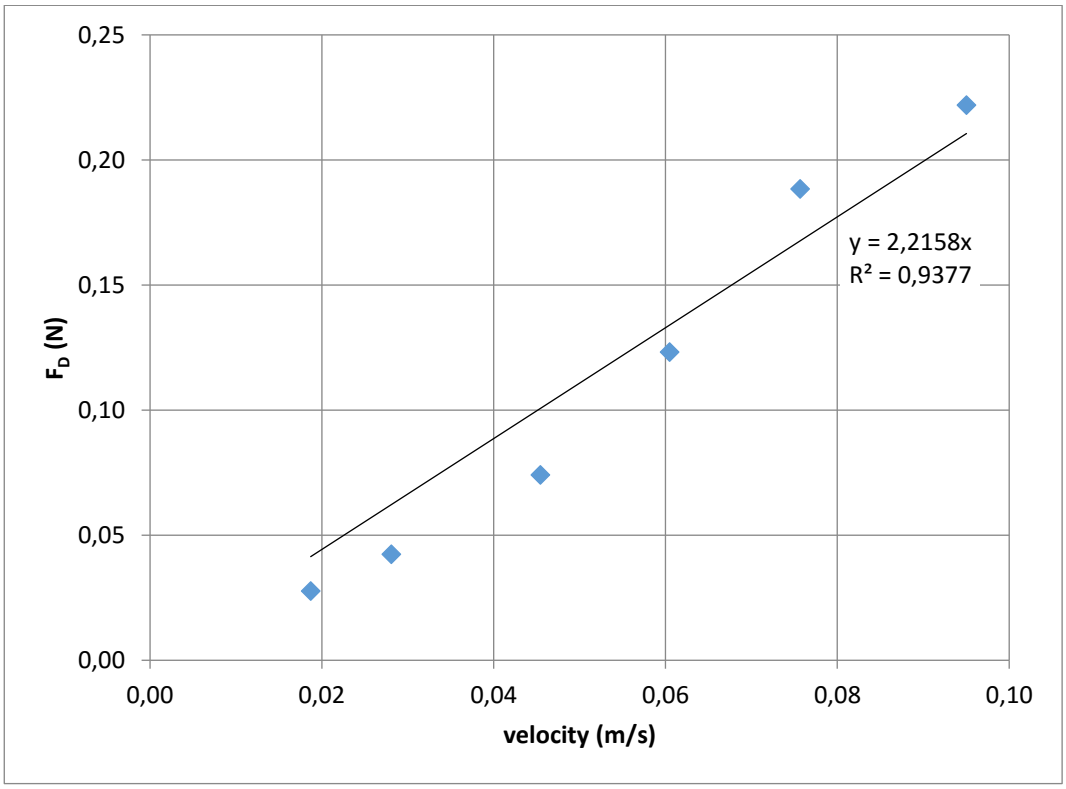

Figure 4-29: Relationship between drag force and average flow velocity for Combination 2

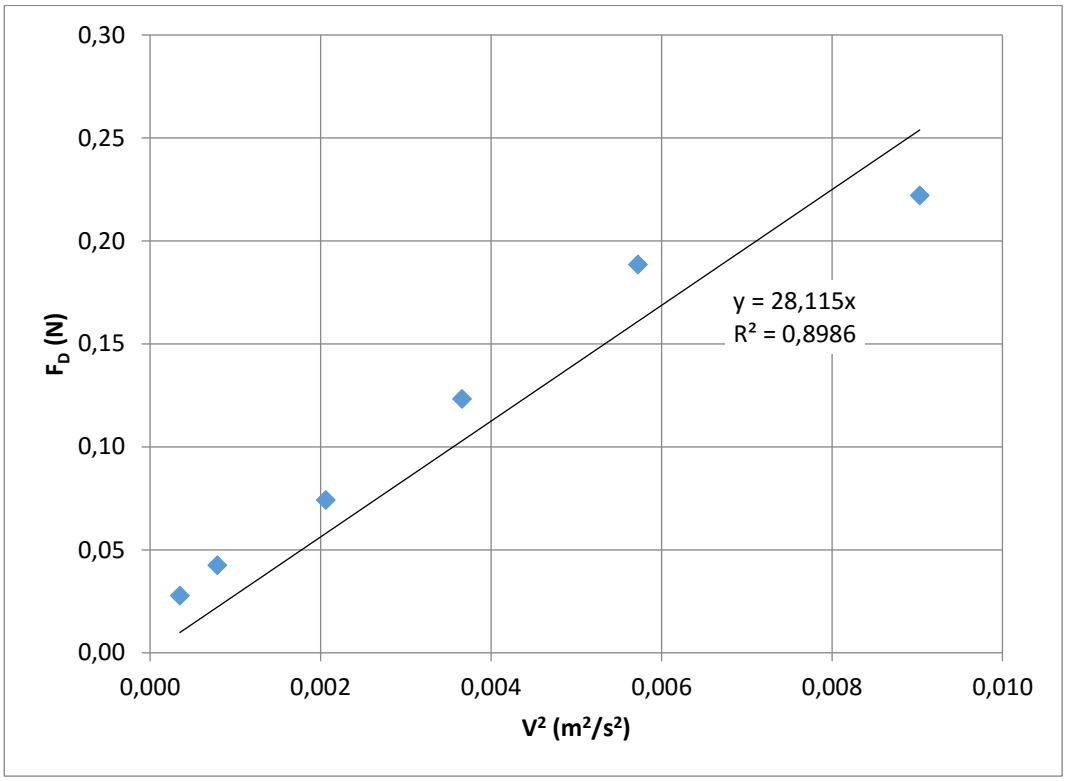

Figure 4-30: Relationship between drag force and average flow velocity squared for Combination 2

4.6.1.3 Combination 3 (λ = 0.131)

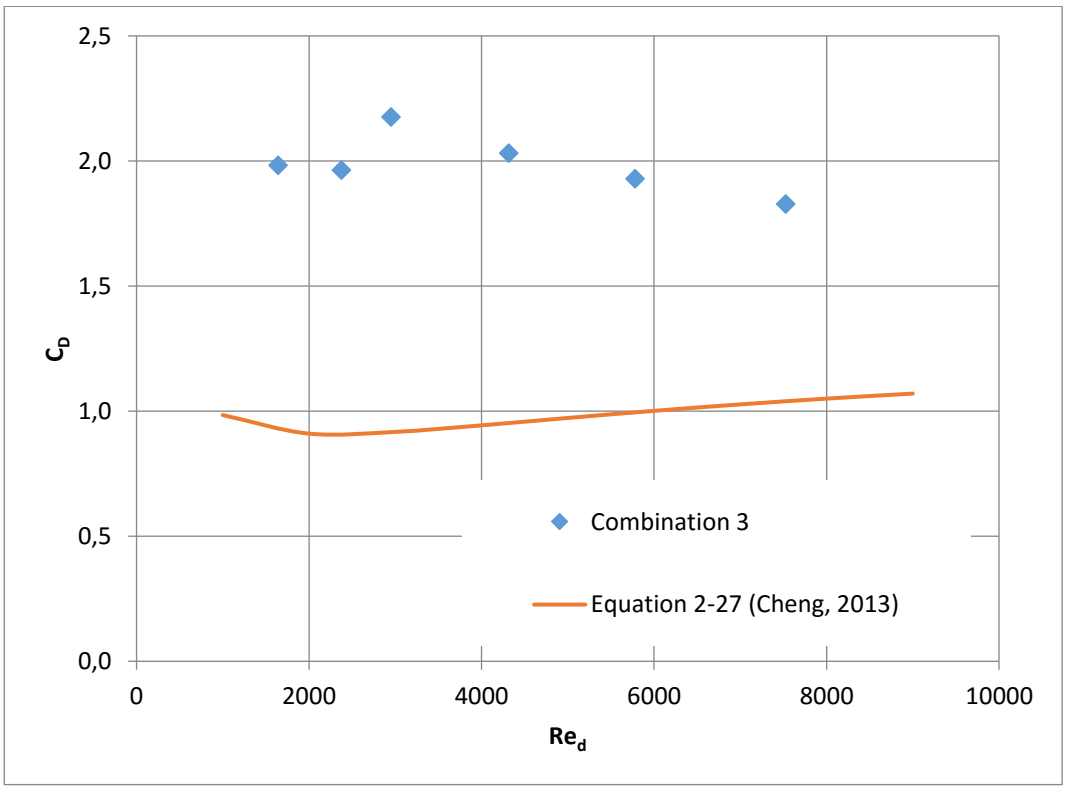

Figure 4-31: Relationship between drag coefficient and cylinder Reynolds number for Combination 3

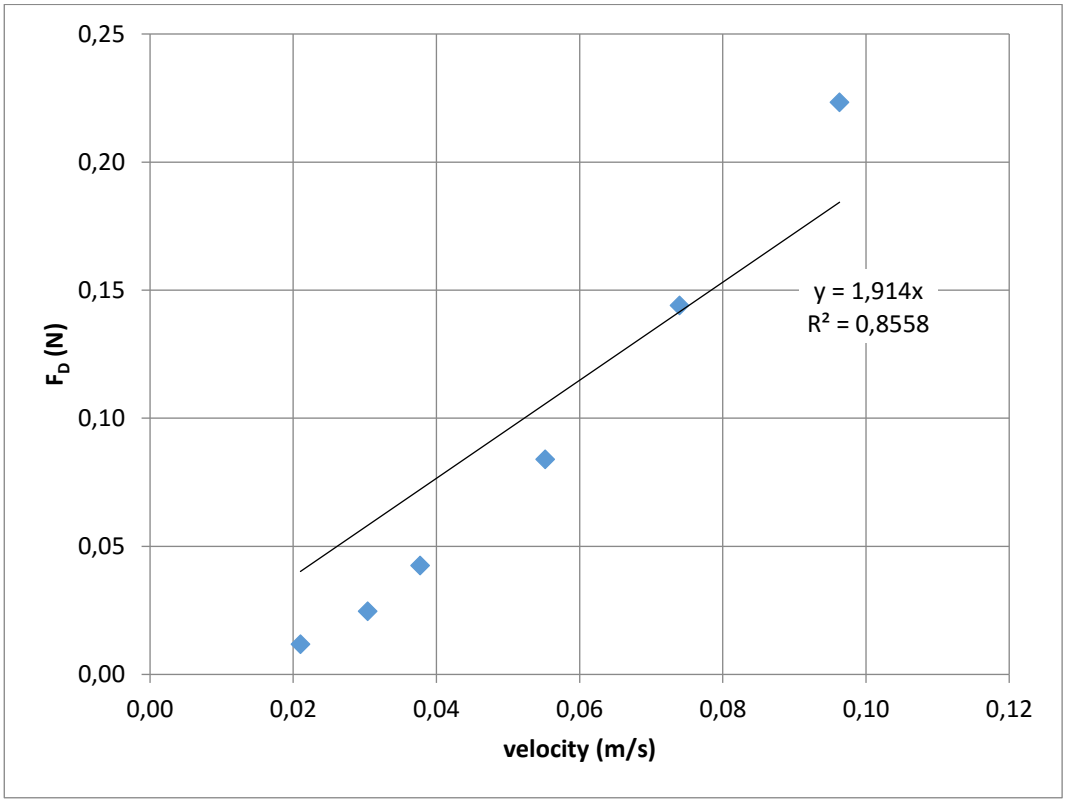

Figure 4-32: Relationship between drag force and average flow velocity for Combination 3

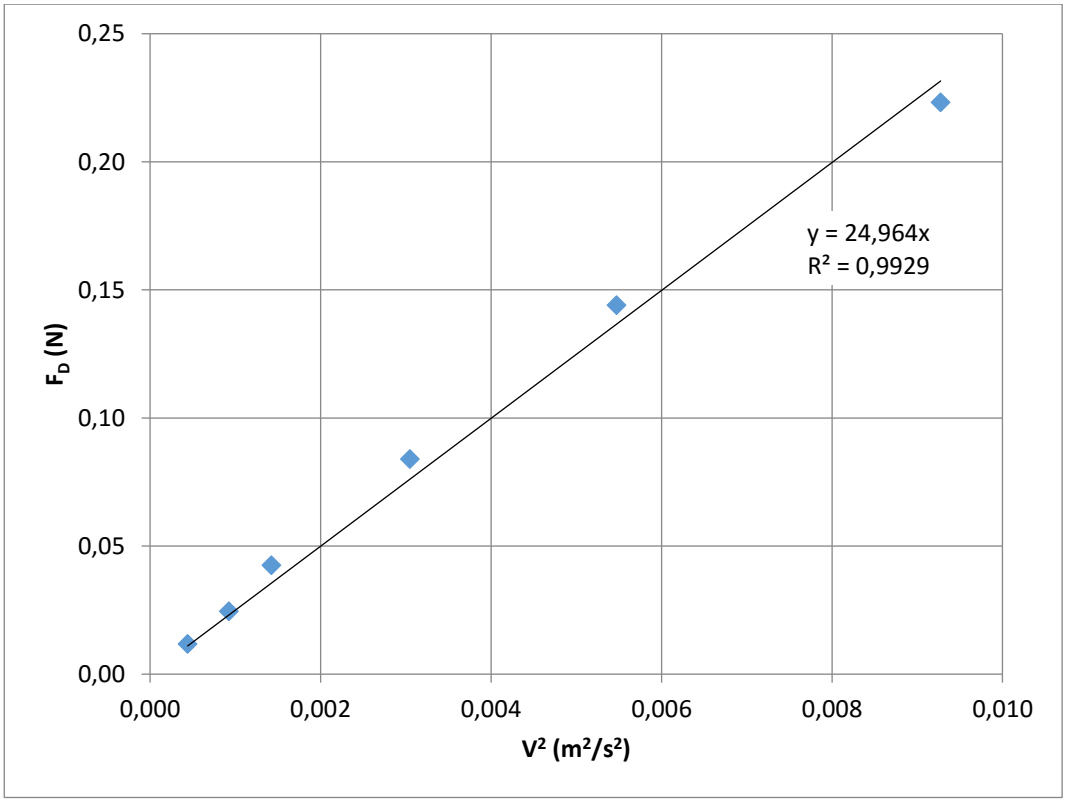

Figure 4-33: Relationship between drag force and average flow velocity squared for Combination 3

4.6.1.4 Combination 4 ($\lambda = 0.174$)

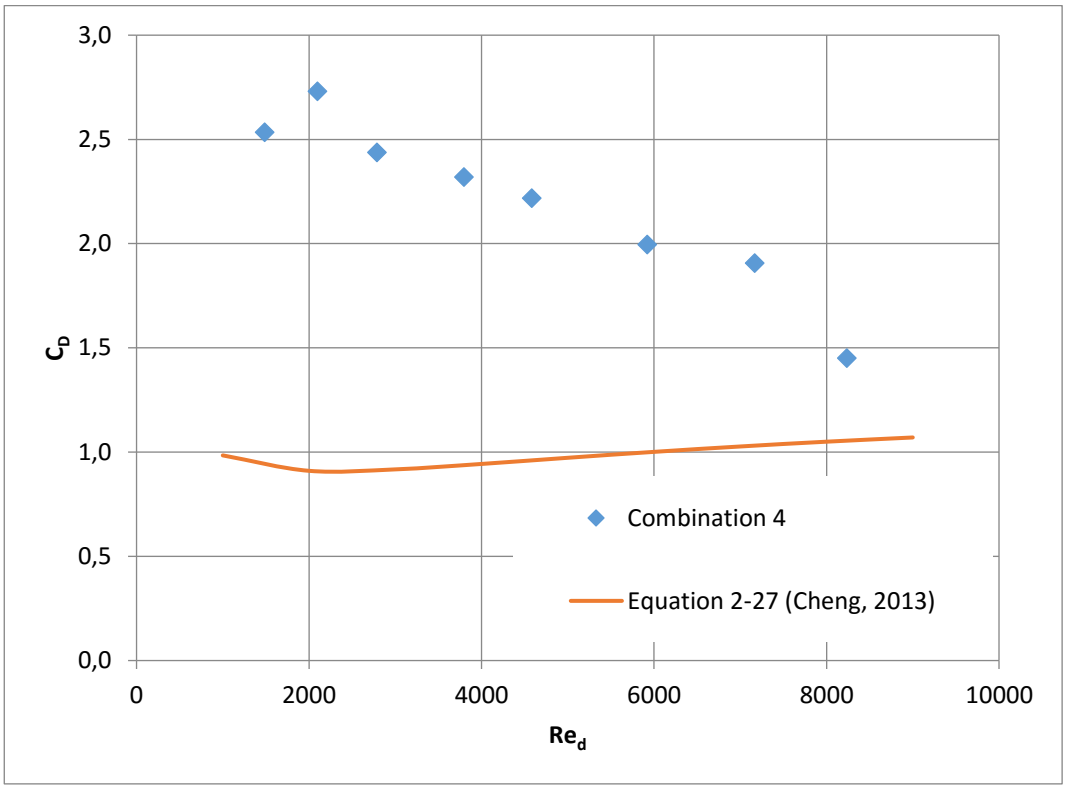

Figure 4-34: Relationship between drag coefficient and cylinder Reynolds number for Combination 4

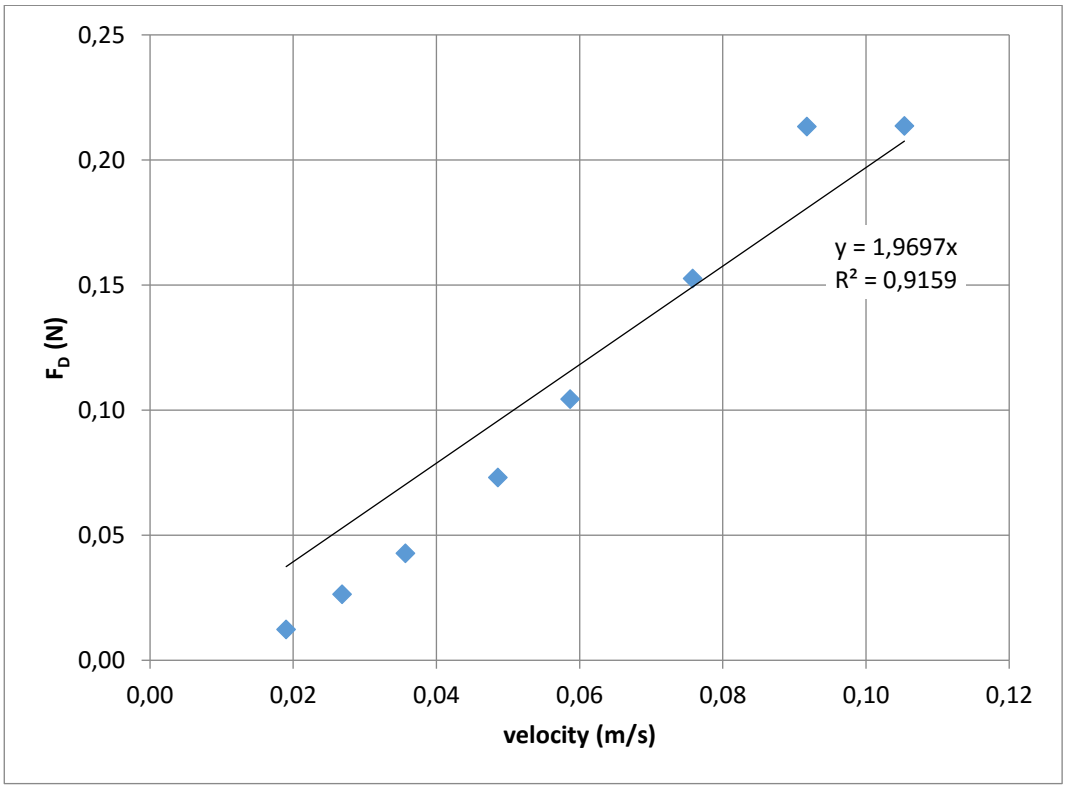

Figure 4-35: Relationship between drag force and average flow velocity for Combination 4

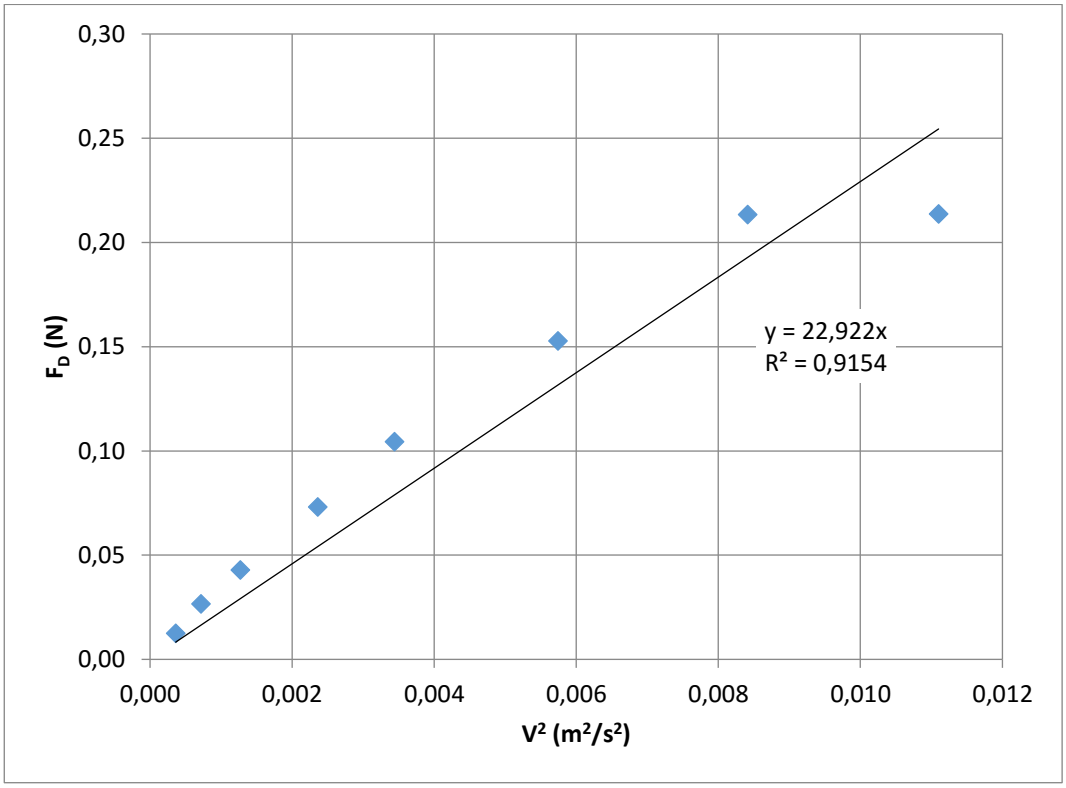

Figure 4-36: Relationship between drag force and average flow velocity squared for Combination 4

Although the results of the present study show that the drag coefficient of an isolated cylinder is increased by a grouping of cylinders, there is no clear relationship between cylinder density and drag coefficient (Figure 4-37). This is in partial disagreement with the results obtained by Kothyari *et al*. (2009), James *et al*. (2004), Ishikawa *et al*. (2000), Tanino and Nepf (2008) and Cheng (2013) who all found distinctive evidence that the drag coefficient increases with increasing cylinder density.

The reason for the present study deviating from the reported relationships for the previously mentioned researchers is unclear, it must however be highlighted that the experimental conditions are not strictly comparable. The experimental investigations carried out by the researchers all focussed on cylinders representing vegetation and therefore the cylinder diameters were small in relation to the flow depth which was not the case for the present research. The investigation carried out by Nepf (1999) only considered the influence of the lateral and longitudinal spacing of a single upstream cylinder on a cylinder downstream whereas the present study considers a grouping of cylinders upstream and downstream of the test cylinder.

The flow structure is complex and offering a valid and conclusive explanation for the experimental results would require an experimental investigation itself. However, it is conceivable that the wake zones of the two upstream cylinders may be acting to channel and accelerate the flow onto the test cylinder. This may explain why in Figure 4-37 it is not the highest density that attains the highest drag coefficient but perhaps the density which best channels the flow onto the test cylinder. The sudden sharp rise for the two lowest Reynolds number values may be attributed to ideal channelling conditions. The results are nevertheless similar in magnitude for the different densities, with Combination 2 attaining slightly higher drag coefficients than the other 3 densities.

4.6.1.5 Comparison

The results of combination 2 are very different in form and magnitude to those of Combinations 1, 3 and 4 as shown in Figure 4-37. The drag coefficients are higher than the other combinations and there is a sharp rise in the drag coefficient magnitude. It is unclear why this occurs, it is postulated that this density channels the flow onto the test cylinder the most effectively of the tested densities. The channelling of the flow causes higher velocities and therefore higher drag forces.

A regression analysis was performed on the data to fit an equation that could be used for practical purposes. Unlike the single cylinder regression analyses, the analysis yielded an unrealistic curve. On inspection of Figure 4-37, if the outliers of combination 2 are ignored, it is clear that a straight line would best approximate the data. It was therefore decided to perform a simple regression analysis in *Microsoft's* Excel software package. All the data except for a number of outliers (Figure 4-37) for combination 1 - 4 was used in the regression. The result is presented in Figure 4-38 and the curve is described by equation (4-4).

$$C_D = -2e(-05)Re_d + 2.0334 \qquad (4\text{-}4)$$

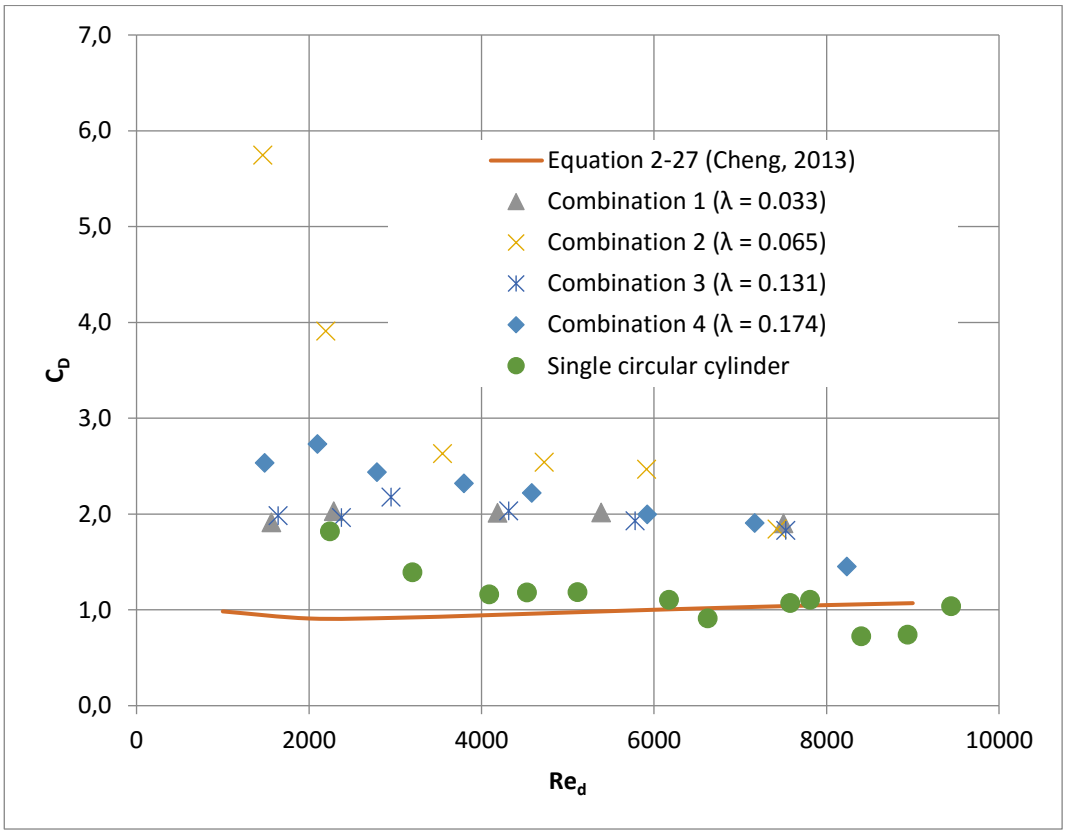

Figure 4-37: Comparison of drag coefficient vs cylinder Reynolds number relationships for the four Combinations.

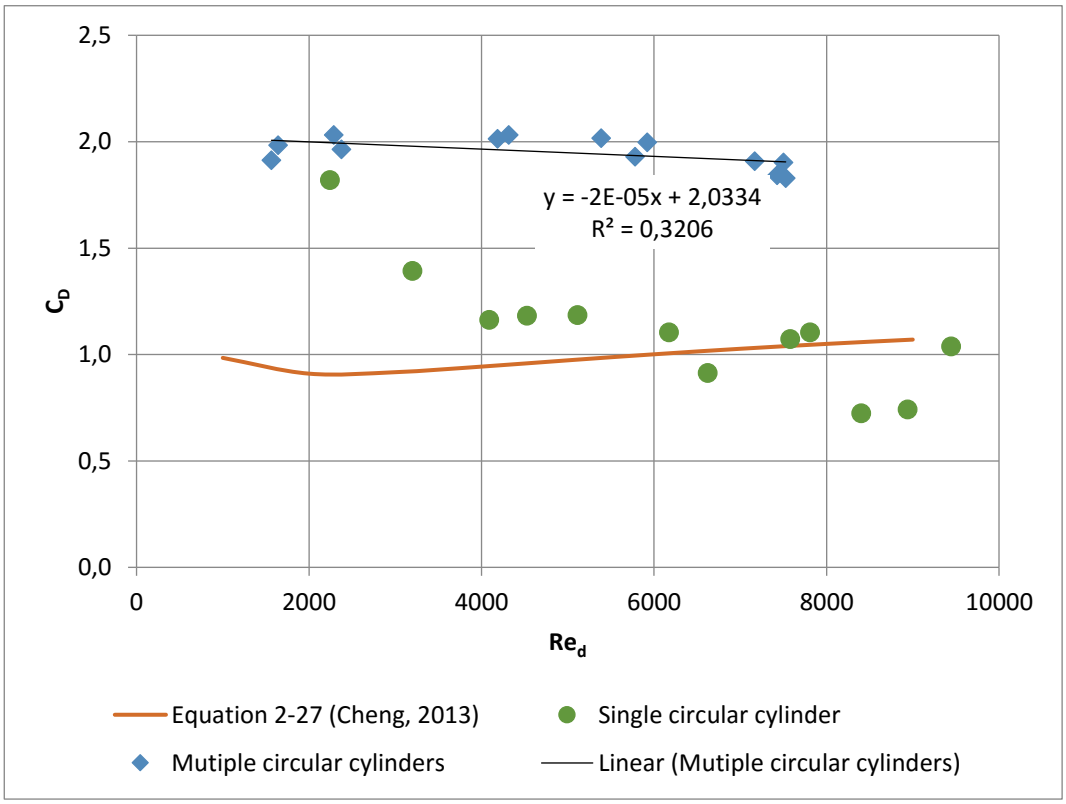

Figure 4-38: Multiple cylinder regression analysis

4.6.2 Conclusion

The experimental investigation produced unique results which partially agree and disagree with the results of previous researchers. The drag coefficient was found to be distinctly higher than that of an isolated cylinder, however, no distinct relationship was found between the drag coefficient and cylinder density as reported by previous researchers. It is proposed that the wake zones of the upstream cylinders channel and accelerate the conventional flow onto the test cylinder which results in higher drag forces. This would need to be confirmed by further research.

5 APPLICATION FOR RESISTANCE PREDICTION

In order to prove that the results obtained in the previous experimental investigations are valid and applicable to practical applications, confirmation tests were carried out. These tests made use of the drag coefficients obtained above to predict the discharge for given channel characteristics and given flow depth. The data used for confirmation was extracted from Heyneke *et al*. (2014) experimental data for circular cylinders only (Table 5-1). The experiments were conducted in a 10.66 m long, 1.00 m wide tilting flume. Three different cylinder areal densities were placed in the flume and subjected to varying discharges and flow depths. The cylinders were the same as used in the present experimental investigations. Figure 5-1 shows the cylinder layout for series A experiments. Series B and C patterns were created by removing cylinders from this pattern (these patterns are presented in appendix D). The cylinders remained in the emergent condition and the slope was kept constant at 0.0061 throughout the investigation. The discharge was set by a valve at the upstream side of the flume and uniform flow was achieved by adjusting a horizontal weir on the downstream side of the flume. The water level in the flume was measured using stilling pots spaced 1.10 m along the length of the flume and the weir was adjusted until the water surface matched the bed slope. The average of the flow depth measurements was used as the flow depth. A turbine meter in the supply line was used to measure the discharge, this was verified using a downstream v-notch weir. The layout of the cylinders can be found in appendix D.

Table 5-1: Heyneke et al. (2014) experimental conditions

Series	Pattern	Discharge (l/s)	Flow depth (mm)	λ
A	1	10.17 - 29.34	44.76 - 117.04	0.065
B	2	8.93 - 33.30	31.92 - 85.02	0.038
C	3	9.99 - 35.58	28.61 - 78.78	0.029

The prediction method used is similar to the synthesis method proposed by Petryk and Bosmjian (1975), Stone and Shen (2002) and James *et al* (2004, 2008) for flow through emergent vegetation. A full description of the method is beyond the scope of this report, thus a brief overview is given. The method accounts for surface

resistance and form resistance with equations appropriate to the type of resistance, and these equations are combined into a single equation. The Darcy-Weisbach equation is used to represent the bed shear and the general drag equation represents the form drag. The equations are combined which results in equation (5-1).

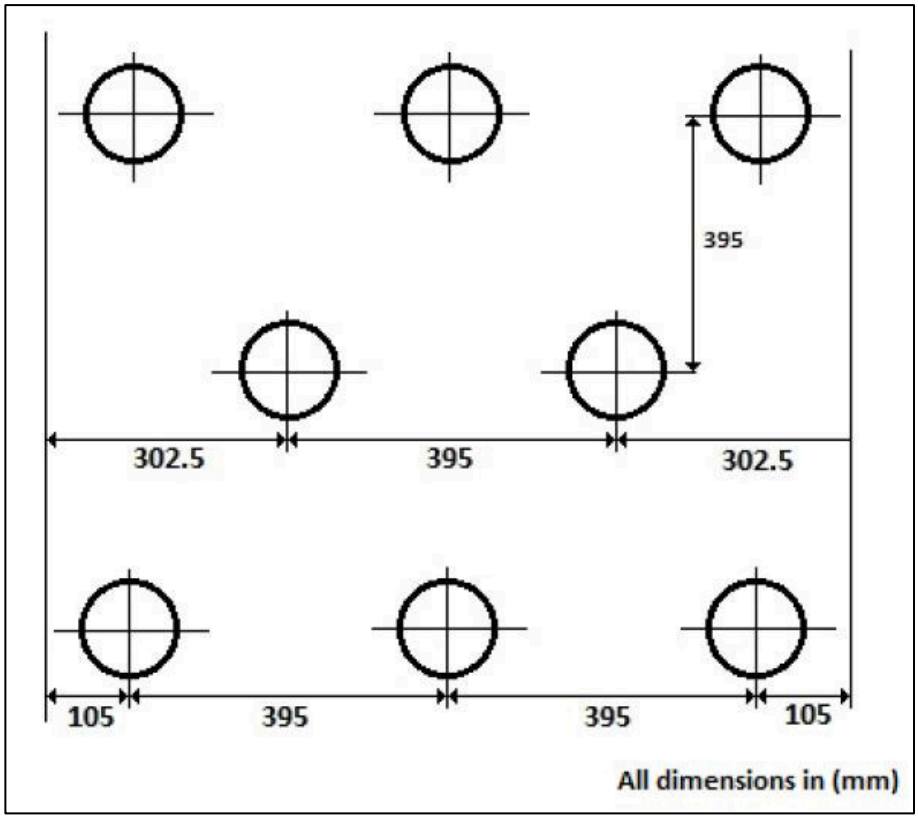

Figure 5-1: Cylinder spacing for series A experiments. Series B and C were created by removing cylinders from this pattern. (Heyneke, et al., 2014)

$$V = \sqrt{\frac{8\,g}{f_b + 4C_D\frac{A_b}{A_{bf}}}}\sqrt{\frac{Vol}{A_{bf}}\,S} \tag{5-1}$$

where

$$A_p = n\,D\,d \tag{5-2}$$

$$A_{bf} = 1 + \frac{2D}{W} - \alpha n\frac{\pi d^2}{4} \tag{5-3}$$

$$Vol = A_n\,D \tag{5-4}$$

$$A_n = 1 - n\frac{\pi d^2}{4} \tag{5-5}$$

where D is the flow depth, n is the number of cylinders per unit area, d is the cylinder diameter, W is the width of the channel and α is a factor to compensate for the separation zone behind the cylinders where bed shear does not occur. Thompson and Roberson (1976) suggest values of α in the range 2.0 to 3.0. This factor made a negligible difference to the results and was assumed to be 2.5.

The surface shear friction factor was obtained using the equation appropriate to the boundary flow condition (equation (5-8) - (5-10)) as provided by the ASCE Task Force on Friction Factors in Open Channels (1963). The boundary flow condition is described by its shear Reynolds number (Re^*), which is defined by equation (5-8).

$$Re^* = \frac{u_* k_s}{\nu} \tag{5-6}$$

where
$$u_* = \sqrt{gRS_o} \tag{5-7}$$

u_* is the shear velocity, k_s is the equivalent roughness height, ν is the kinematic viscosity of water, g is the gravitational acceleration, R is the hydraulic radius (cross sectional flow area divided by the wetted perimeter) and S_o is the energy slope.

Hydraulically smooth:

$$\frac{1}{\sqrt{f_b}} = c\ \log\left(\frac{Re\sqrt{f_b}}{b}\right) \tag{5-8}$$

Transitional:

$$\frac{1}{\sqrt{f_b}} = -c\ \log\left(\frac{k_s}{a\,R} + \frac{b}{Re\sqrt{f_b}}\right) \tag{5-9}$$

Hydraulically Rough:

$$\frac{1}{\sqrt{f_b}} = c\ \log\left(\frac{a\ R}{k_s}\right) \tag{5-10}$$

$$Re = \frac{4VR}{\nu} \tag{5-11}$$

Re is the Reynolds number.

The task force recommends the following values for the coefficients:

a = 12

b = 2.51

c = 2

The value of *b* was however recalibrated for the flume and was found to be 9.55. The value of k_s was found to be 0.46 mm.

Equation (4-4) for the multiple cylinder regression analysis in section 4.6 was used to determine the value for the drag coefficient.

The experimental conditions for Heyneke *et al*. (2014) are given in Table 5-1. Pattern 1 is similar to the patterns utilised in the present experimental investigation, the other two patterns are considerably different.

5.1 Results

Figure 5-2 shows relatively good agreement between the measured and predicted discharges. The equations slightly over predict the discharge for the two higher areal densities (series A and B) and slightly under predict the discharge for the lowest density. Table 5-3 and Table 5-4 show very close agreement (error = 7.43% and 3.74% respectively) considering that the cylinder patterns were very different to the pattern used in the present study. This may indicate that the cylinder layout has a negligible influence on the drag coefficient but further verification would be

required. Figure 5-2 shows that at higher discharges, the equations slightly under predict the discharge. The Reynolds number range covered by the data of Heyneke *et al*. (2014) is between ± 17 500 and ± 35 500, whereas the Reynolds number range covered by the multiple cylinder experimental investigation is between ± 1 500 to ± 10 000. This may explain the deviation of the points for high discharges. The accuracy of the predictions could therefore be improved by carrying out further experimental investigations which considers a wider range of cylinder densities, determines the impact of cylinder layouts and expands on the current Reynolds number range covered by this investigation.

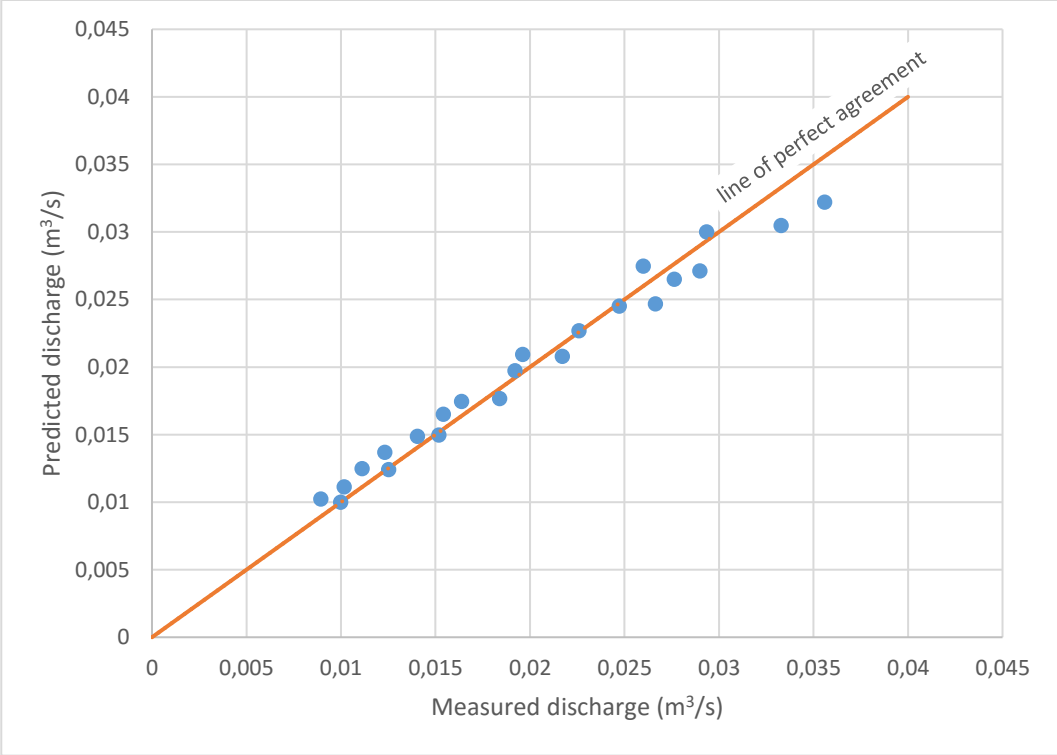

Figure 5-2: Measured discharge versus predicted discharge

Table 5-2: Measured and predicted discharges and corresponding errors for series A data

Measured discharge (l/s)	**Predicted discharge (l/s)**	**Error (%)**
10.17	11.13	9.48
12.32	13.69	11.14
15.41	16.50	7.08
19.20	19.73	2.76
22.59	22.70	0.49
25.99	27.47	5.69
29.34	30.00	2.27
	Average absolute error	**5.56**

Table 5-3: Measured and predicted discharges and corresponding errors for series B data

Measured discharge (l/s)	Predicted discharge (l/s)	Error (%)
8.93	10.23	14.51
11.12	12.48	12.27
14.04	14.87	5.92
16.37	17.45	6.57
19.60	20.93	6.77
24.72	24.52	-0.82
27.63	26.49	-4.14
	Average absolute error	**7.43**

Table 5-4: Measured and predicted discharges and corresponding errors for series C data

Measured discharge (l/s)	Predicted discharge (l/s)	Error (%)
9.99	10.00	0.09
12.53	12.42	-0.84
15.18	14.96	-1.45
18.40	17.67	-3.97
21.71	20.80	-4.18
26.64	24.67	-7.39
28.99	27.12	-6.44
	Average absolute error	**3.74**

5.2 Conclusion

The predicted discharges give a good approximation of the measured values. The predictions for high discharges are slightly under predicted. This has been attributed to the current data range not covering the range for the measured data. The predictions could be improved through a more extensive experimental investigation which covers a larger Reynolds number range, considers the impact (if any) of cylinder patterns and covers more cylinder areal densities.

6 CONCLUSIONS

6.1 Single cylinder experimental investigations

The results of the single circular cylinder experimental investigation showed that the relationship between the drag coefficient and Reynolds number follows that of an infinitely long cylinder a lot closer than that which previous researchers have reported. The drag coefficients are generally higher than those for the infinite cylinder. The explanation for this trend has been attributed to free surface flow. The drag coefficient increases sharply below cylinder Reynolds numbers of ± 4 000 which is significantly larger than the infinite cylinder where the sharp increase occurs at Reynolds numbers of ± 100. This is attributed to the possibility of increasing viscous drag or it may be due to the equipment being insufficiently sensitive. A regression analysis was carried out and an equation formulated which can be used for practical purposes.

The results for the single square and diamond shaped cylinders showed that the drag coefficients are substantially larger than the circular cylinders. The squares are approximately double the drag coefficient of the circular cylinder value for the same Reynolds number and the diamonds are approximately triple the value of the circular cylinders for the same Reynolds numbers. The square and diamond shapes are a lot less streamlined and therefore induce much larger wake zones and free surface drag. Interestingly, and contrary to the general drag equation, the results suggest that the drag force would be better approximated by not squaring the velocity term in the equation. A regression analysis was carried out and an equation formulated for practical purposes.

6.2 Multiple cylinder experimental investigation

The results of the experimental investigation show that the drag coefficient for a single cylinder amongst multiple cylinders is substantially larger than an isolated cylinder. The reason for the increase is unknown and an explanation is not transparent as the flow structure is highly complex. A possible hypothesis is that

the upstream cylinders channel and accelerate the conventional flow onto the downstream cylinders which causes the drag force to increase. This hypothesis would need to be verified by further testing.

The results did not reveal a clear or obvious relationship between the cylinder density and the drag coefficient as previous researchers have reported. This may be because the cylinders have much lower aspect ratios than the cylinders used by the other researchers.

A very simplistic regression analysis was carried out on the data. The resulting equation was used in the confirmation tests and gave reasonably accurate predictions of measured discharges. This proves the applicability of the equation for practical purposes. The equation should be improved through a more comprehensive experimental investigation.

6.3 Recommendations for further research

The results of this report are suitable for use in predicting flow characteristics in the field. The equations developed are however based entirely on empiricism and will benefit from refinement and extension by carrying out further experimental investigations. The equations are based entirely on experimental data which have been verified with further laboratory data. It would therefore be highly beneficial to verify and calibrate these equations with field data.

The single circular investigation should be extended by collecting more data for Reynolds numbers below ± 4 000 and above ± 20 000. The data should be collected with apparatus which is substantially more sensitive than the current apparatus. The unusual trend identified should be further investigated by gathering more data points in this region and quantifying the velocity structure around the cylinder. The relationship between the drag coefficient and the cylinder aspect ratio should be studied. This can be done by keeping flow conditions constant and varying the cylinder diameters.

The square and diamond cylinder database should be increased, specifically for Reynolds numbers below ± 1 000 and above ± 4 000. The additional data will elucidate the relationship between drag force and velocity, and drag force and velocity squared.

The database for multiple cylinders requires considerable expansion in terms of the Reynolds number range as well as the range of cylinder areal densities. This will improve the accuracy and usability of the current equations. The mechanisms by which the drag force on an individual cylinder is amplified by the presence of multiple cylinders requires investigation. The velocity structure around the cylinder should be determined for the individual case and compared to the structure for the multiple cylinder case whilst exposed to the same flow condition.

7 REFERENCES

Albertson, M. L., Barton, J. R. & Simons, D. B., 1960. *Fluid Mechanics for Engineers.* New Jersey: Prentice Hall, Englewood Cliffs.

ASCE Task Force on Friction Factors in Open Channels, 1963. Friction factors in open channels. *Journal of the Hydraulics Division, ASCE,* 89(HY2), pp. 97-143.

Cheng, N.-S., 2013. Calculation of drag coefficient for arrays of emergent circular cylinders with pseudofluid model. *Journal of Hydraulic Engineering,* 139(6), pp. 602-611.

Cheng, N. S. & Chiew, Y. M., 1999. Incipient sediment motion with upward seepage. *Journal of Hydraulic Research,* 37(5), pp. 665-681.

Chow, V. T., 1959. *Open Channel Hydraulics.* New York: McGraw-Hill.

Clift, R., Grace, J. R. & Weber, M. E., 1978. *Bubbles, drops and particles.* 1 ed. New York: Academic Press.

Cowan, W. L., 1956. Estimating hydraulic roughness coefficients. *Agric. Eng.,* 137(7), pp. 473-475.

Einstein, A. H. & Barbarossa, N. L., 1952. River channel roughness. *Trans. ASCE,* Volume 117, pp. 1121-1143.

Ergun, S., 1952. Fluid flow through packed columns. *Chem. Eng. Prog.,* 48(2), pp. 89-94.

Fenton, J. D., 2008. *Obstacles in streams and their roles as hydraulic structures.* Pisa, s.n., pp. 15-22.

Fenzl, R. N., 1962. *Hydraulic resistance of broad shallow vegetated channels,* Davis: University of California at Davis.

Finn, R. K., 1953. Determination of the drag on a cylinder at low Reynolds numbers. *Journal of Applied Physics,* 24(6), pp. 771-773.

Heyneke, M., Matulovich, K. & van der Haar, M., 2014. *Form resistance for large emergent roughness elements*, Final year investiigational project, School of Civil and Environmental Engineering, University of the Witwatersrand, Johannesburg, South Africa

Hicks, D. M. & Mason, P. D., 1991. *Roughness Characteristics of New Zealand Rivers.* Wellington: Water Resources Survey.

Ishikawa, Y., Mizuhara, K. & Ashida, S., 2000. Effect of density of trees on drag exerted on trees in river channels. *Journal of Forest Research,* 5(4), pp. 271-279.

James, C. S., 2012. *Partitioned resistance in channels with large emergent roughness elements,* Johannesburg: Draft Paper.

James, C. S., Birkhead, A. L., Jordanova, A. A. & O'Sullivan, J. J., 2004. Flow resistance of emergent vegetation. *Journal of Hydraulic Research,* 42(4), pp. 390-398.

James, C. S., Goldbeck, U. K., Patini, A. & Jordanova, A. A., 2008. Influence of foliage on flow resistance of emergent vegetation. *Journal of Hydraulic Research,* 46(4), pp. 536-542.

Jayaweera, K. O. L. F. & Mason, J., 1965. The behavior of freely falling cylinders and cones in a viscous fluid. *Journal of fluid mechanics,* 22(4), pp. 709-720.

Kothyari, U. C., Hayashi, K. & Hashimoto, H., 2009. Drag coefficient of unsubmerged rigid vegetation stems in open channel flows. *Journal of Hydraulic Research,* 47(6), pp. 691-699.

Kouwen, U. C. & Fathi-Moghadam, M., 2000. Friction factors for coniferous trees along rivers. *Journal of Hydraulic Engineering,* 126(10), pp. 732-740.

Lamb, H. S., 1945. *Hydrodynamics.* 1 ed. New York: Dover Publications.

Li, R. M. & Shen, H. W., 1973. Effect of tall vegetations on flow and sediment. *Journal of the Hydraulics Division,* 99(HY5), pp. 793-814.

Liu, D., Diplas, P., Fairbanks, J. D. & Hodges, C. C., 2008. An experimental study of flow through rigid vegetation. *Journal of Geophysical Research,* 113(F4).

Lorenz Messtechnik GmbH, 2015. *Miniature tension force sensor specifications,* Alfdorf: Lorenz Messtechnik GmbH.

Madhi, Y. & Bismilla, B. A., 2014. *Drag force on emergent broad circular cylinders,* Final year investiigational project, School of Civil and Environmental Engineering, University of the Witwatersrand, Johannesburg, South Africa

Nepf, H. M., 1999. "Drag, turbulence, and diffusion in flow through emergent vegetation.". *Water Resources Research,* 35(2), pp. 479-489.

Petryk, S. & Bosmajian, G., 1975. Analysis of flow through vegetation. *Journal of the Hydraulics Division. ASCE,* 101(HY7), pp. 871-884.

Ranga Raju, K. G., Rana, O. P. S., Asawa, G. L. & Pillai, A. S. N., 1983. Rational assessment of blockage effect in channel flow past smooth circular cylinders. *Journal of Hydraulic Research,* 21(4), pp. 289-302.

Raupach, M., 1992. Drag and drag partition on rough surfaces. *Boundary Layer Meteorology,* Volume 60, pp. 375-395.

Reuteler, D., 1994. *the drawings of Leonardo da Vinci.* [Online] Available at: http://www.drawingsofleonardo.org/images/oldmanwater.jpg [Accessed 12 August 2016].

Richter, B. R., Baumgartner, J. V., Wigington, R. & Braun, D. P., 1997. How much water does a river need?. *Freshwater Biology,* Volume 37, pp. 231-249.

Shields, F. D. & Gippel, C. J., 1995. Prediction of effects of woody debris removal on flow resistance. *Journal of Hydraulic Engineering,* 121(4), pp. 341-354.

Stoesser, T., Kim, S. J. & Diplas, P., 2010. Turbulent flow through idealized emergent vegetation. *Journal of Hydraulic Engineering,* 136(12), pp. 1003-1017.

Stone, B. M. & Shen, H. T., 2002. Hydraulic resistance of flow in channels with cylindrical roughness. *Journal of Hydraulic Engineering,* 128(5), pp. 500-506.

Tanino, Y. & Nepf, H. M., 2008. Laboratory investigation of mean drag in a random array of rigid, emergent cylinders. *Journal of Hydraulic Engineering,* 134(1), pp. 34-41.

Thompson, A. M., Wilson, B. N. & Hustrulid, T., 2003. Instrumentation to measure drag on idealized vegetal elements in overland flow. *Transactions of the ASABE,* 46(2), pp. 295-302.

Thompson, G. T. & Roberson, J. A., 1976. A theory of flow resistance for vegetated channels. *Trans. Am. Soc. Agric. Engrs,* 19(2), pp. 288-293.

Tritton, D. J., 1959. Experiments of the flow past a circular cylinder at low Reynolds numbers. *Journal of Fluid Mechanics,* 6(4), pp. 547-567.

Tsujimoto, T. & Kitamura, T., 1990. *Velocity profile of flow in vegetated-bed channels,* Japan: Kanazawa University.

Wieselsberger, C., 1922. *New data on the laws of fluid resistance.* Washington, DC, National Advisory Committee for Aeronautics.

Wilson, C. A. M. E., Xavier, P., Schoneboom, T., Aberle, J., Rauch, H. P., Lammeranner, W., Weissteiner, C., Thomas, H., 2010. *The hydrodynamic drag of full scale trees.* Braunschweig, Bundesanstalt fur Wasserbau.

APPENDIX A

Apparatus friction calibration results

Tension sensor

Table A- 1: Tension sensor data

Load Test					
Run No.	**Mass Applied (g)**	**Load Applied (N)**	**Load Cell Reading (N)**	**Difference (N)**	**Error (%)**
1	18,50	0,181	0,14	0,041	22,780
2	26,30	0,258	0,19	0,068	26,282
3	41,70	0,409	0,32	0,089	21,695
4	72,30	0,709	0,56	0,149	20,964
5	111,00	1,088	0,88	0,208	19,103
6	179,90	1,763	1,43	0,333	18,889
7	253,10	2,480	2,02	0,460	18,561
8	318,30	3,119	2,56	0,559	17,931
9	383,70	3,760	3,09	0,670	17,825
10	461,90	4,527	3,74	0,787	17,378
11	501,30	4,913	4,06	0,853	17,358

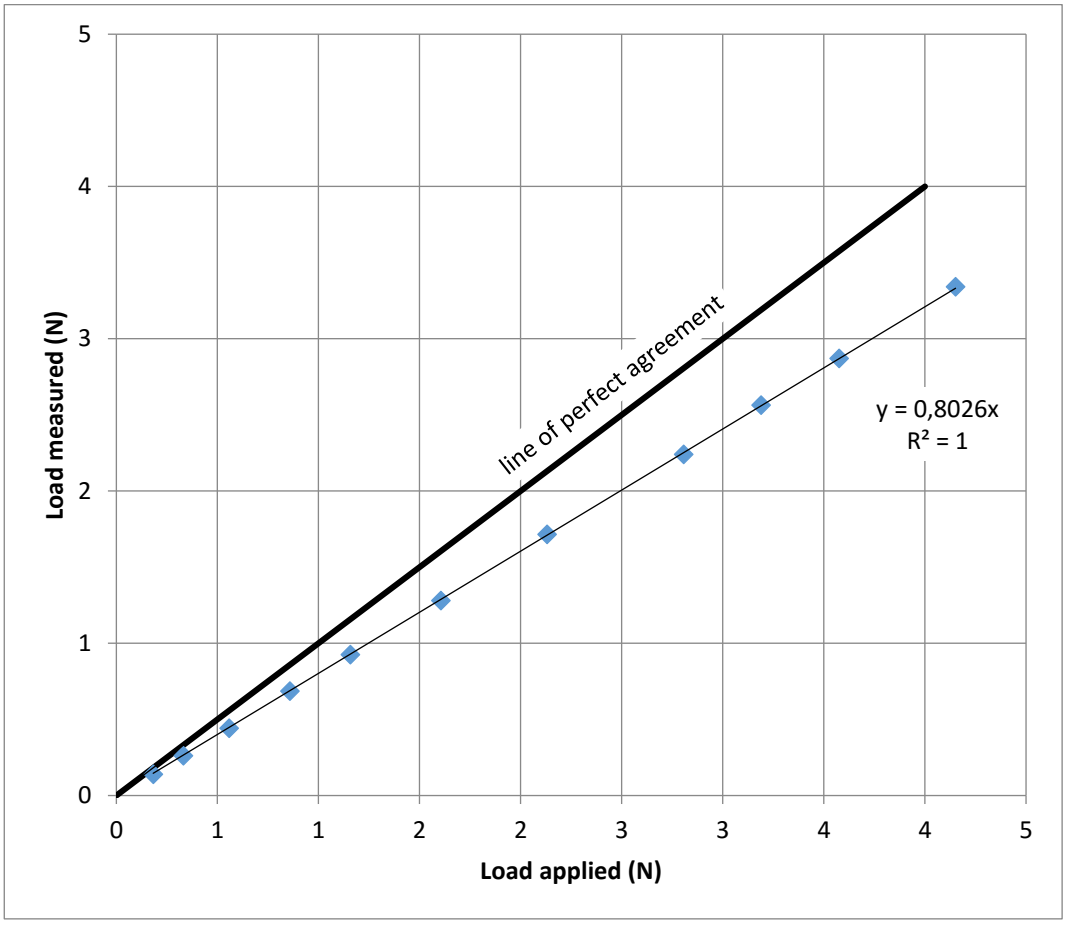

Figure A- 1: Load reading versus load applied for the tension sensor

Configuration 1

Table A- 2: Configuration 1 calibration data

Load Test					
Run No.	**Mass Applied (g)**	**Load Applied (N)**	**Load Cell Reading (N)**	**Difference (N)**	**Error (%)**
1	0,00	0,000	0,00	0,000	0,000
2	7,30	0,072	0,04	0,032	44,087
3	11,90	0,117	0,08	0,037	31,401
4	16,40	0,161	0,11	0,051	31,558
5	21,10	0,207	0,14	0,067	32,295
6	30,00	0,294	0,21	0,084	28,571
7	39,30	0,385	0,28	0,105	27,299
8	48,60	0,476	0,35	0,126	26,514
9	25,50	0,250	0,17	0,080	31,973
10	98,90	0,969	0,73	0,239	24,682
11	98,90	0,969	0,73	0,239	24,682
12	141,90	1,391	1,04	0,351	25,213
13	202,70	1,986	1,49	0,496	24,992
14	266,70	2,614	1,97	0,644	24,627
15	376,30	3,688	2,82	0,868	23,530
16	446,90	4,380	3,34	1,040	23,738
17	511,60	5,014	3,84	1,174	23,410

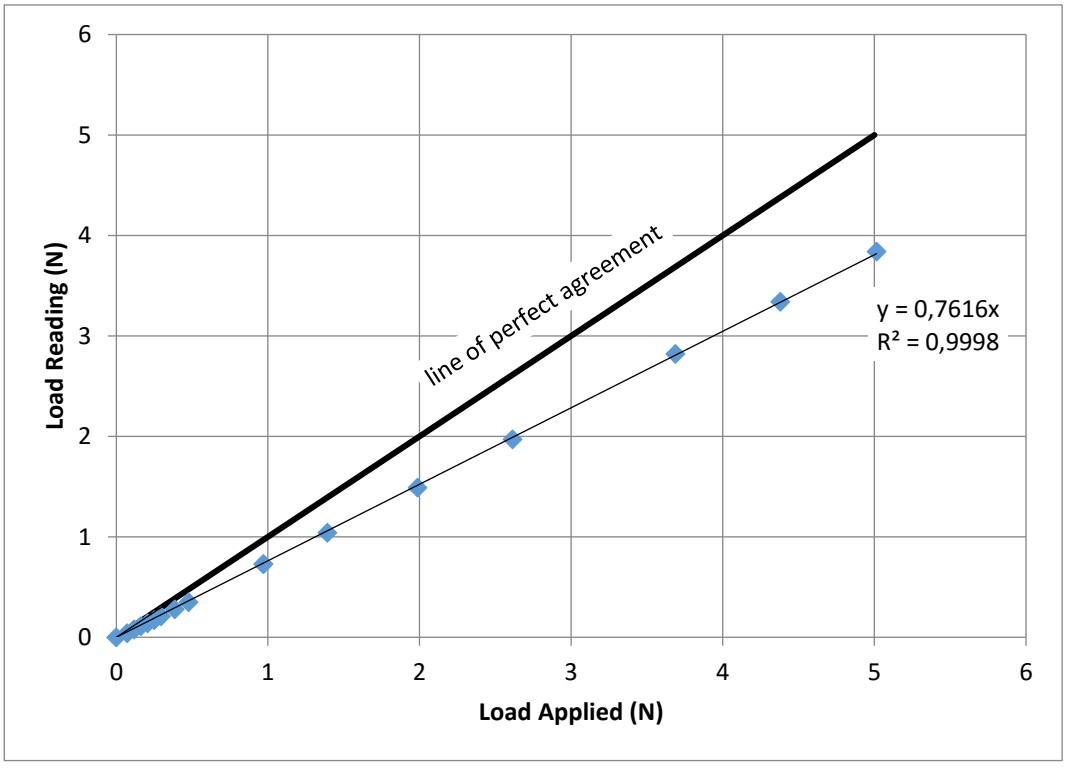

Figure A- 2: Load reading versus load applied for Configuration 1

Configuration 2

Table A- 3: Configuration 2 calibration data

Load Test					
Run No.	**Mass Applied (g)**	**Load Applied (N)**	**Load Cell Reading (N)**	**Difference (N)**	**Error (%)**
1	8,6	0,084	0,074	0,010	12,197
2	19,2	0,188	0,157	0,031	16,560
3	34,7	0,340	0,270	0,070	20,602
4	50,0	0,490	0,386	0,104	21,224
5	80,9	0,793	0,623	0,170	21,420
6	96,2	0,943	0,740	0,203	21,507
7	134,8	1,321	1,037	0,284	21,501
8	189,0	1,852	1,454	0,398	21,499
9	266,5	2,612	2,053	0,559	21,392
10	331,8	3,252	2,541	0,711	21,855
11	405,2	3,971	3,096	0,875	22,034
12	439,9	4,311	3,351	0,960	22,269
13	474,5	4,650	3,609	1,041	22,389
14	494,3	4,844	3,758	1,086	22,422

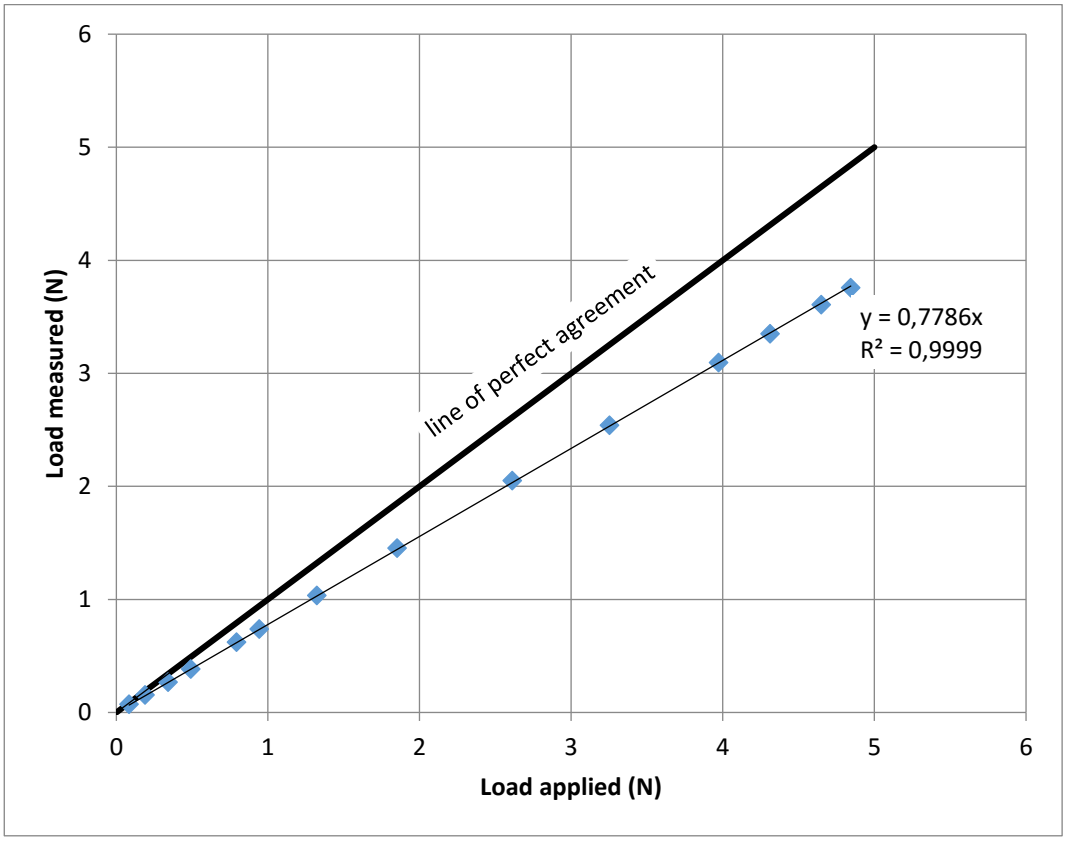

Figure A- 3: Load reading versus load applied for Configuration 2

Configuration 3

Table A- 4: Configuration 3 calibration data

Run No.	Mass Applied (g)	Load Applied (N)	Actual Load (N)	Difference (N)	Error (%)
1	13,6	0,133	0,102	0,031	23,469
2	21,3	0,209	0,159	0,050	24,068
3	28,9	0,283	0,215	0,068	24,087
4	44,3	0,434	0,332	0,103	23,642
5	51,9	0,509	0,393	0,116	22,830
6	67,3	0,660	0,509	0,151	22,825
7	90,5	0,887	0,681	0,206	23,272
8	120,6	1,182	0,916	0,266	22,496
9	151,0	1,480	1,146	0,334	22,591
10	196,3	1,924	1,499	0,425	22,079
11	226,9	2,224	1,731	0,493	22,176
12	285,7	2,800	2,319	0,481	17,174
13	324,7	3,182	2,479	0,703	22,094
14	363,1	3,558	2,773	0,785	22,071
15	402,3	3,943	3,068	0,875	22,182
16	421,7	4,133	3,213	0,920	22,253
17	441,2	4,324	3,378	0,946	21,885

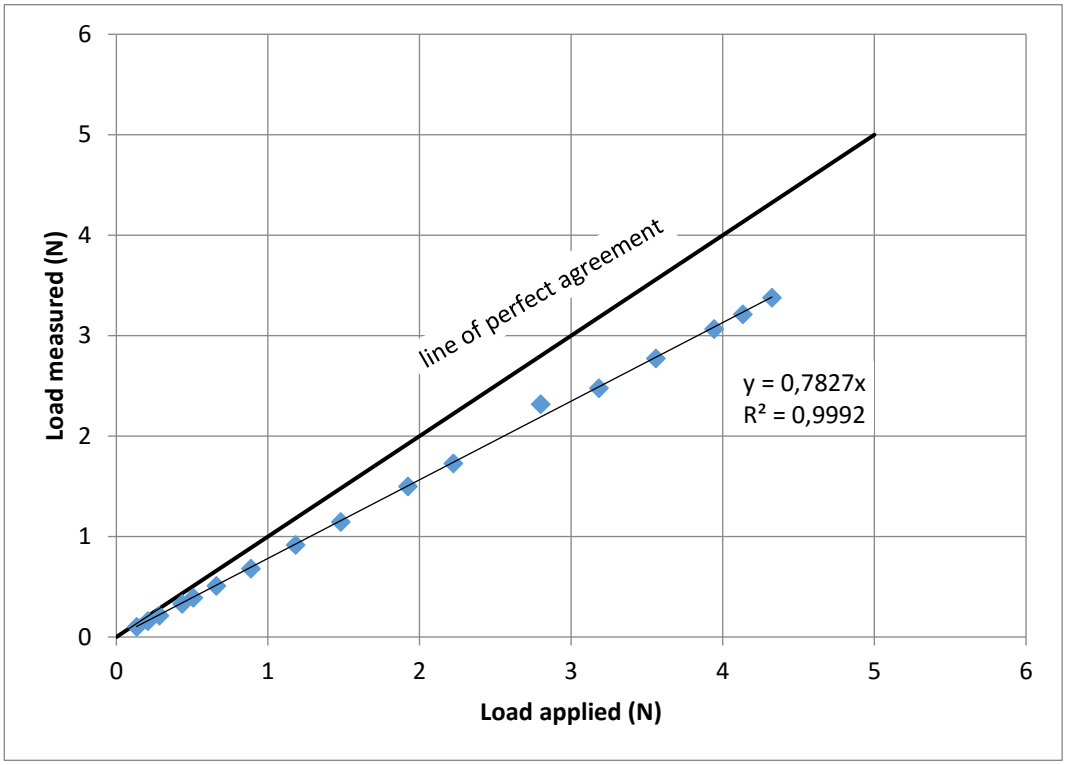

Figure A- 4: Load reading versus load applied for Configuration 3

APPENDIX B

Verification test results

Table B- 1: Verification test data

Run No.	Discharge (l/s)	Flow depth (mm)	Local Velocity (m/s)	Drag force (N)
1	19.83	229.74	0.09	0.06
2	15.08	158.64	0.12	0.09
3	35.33	212.34	0.22	0.34
4	25.86	134.92	0.23	0.36
5	39.19	223.31	0.23	0.37
6	32.75	175.71	0.25	0.42
7	34.03	170.45	0.27	0.53
8	46.14	201.75	0.31	0.69
9	57.75	220.41	0.35	0.88
10	52.14	184.90	0.38	1.07
11	51.33	170.27	0.40	1.20
12	58.56	173.51	0.43	1.42
13	58.19	176.90	0.46	1.61
14	58.58	160.52	0.49	1.86
15	58.58	164.92	0.50	1.89

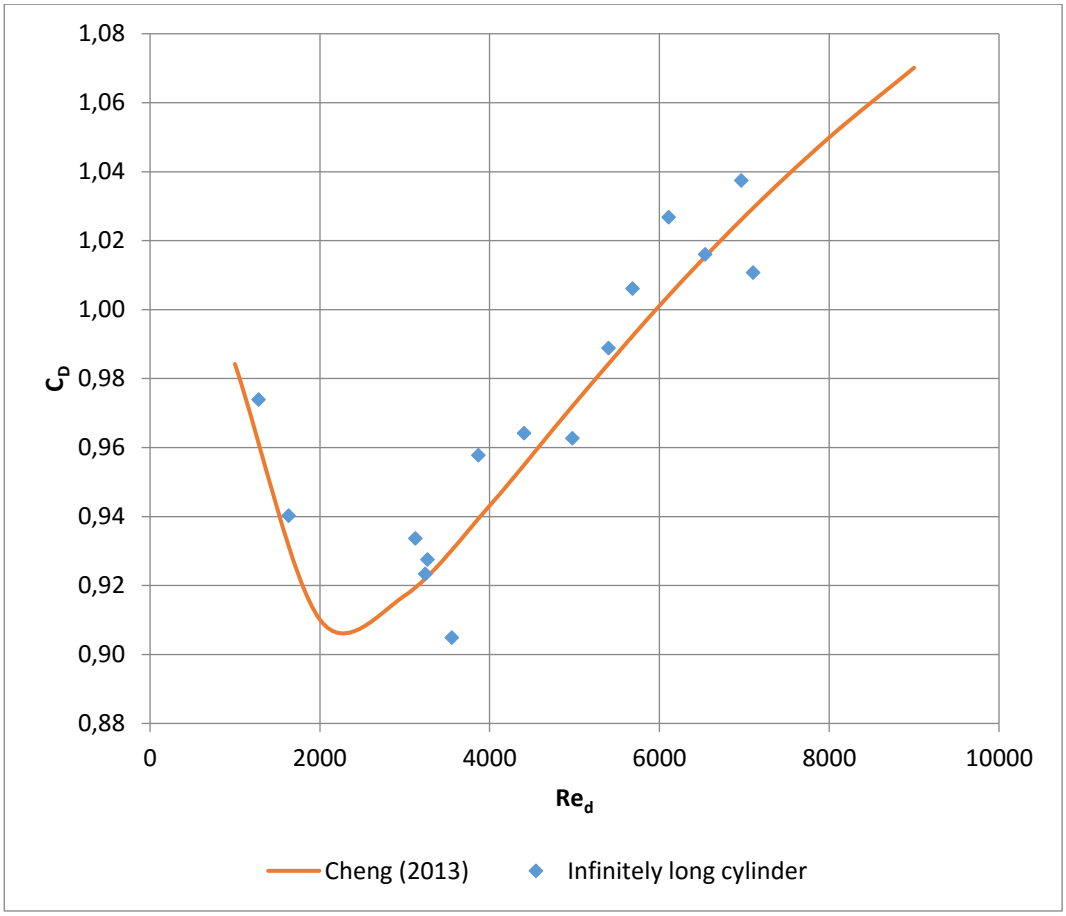

Figure B- 1: Relationship between drag coefficient and cylinder Reynolds number (local velocity)

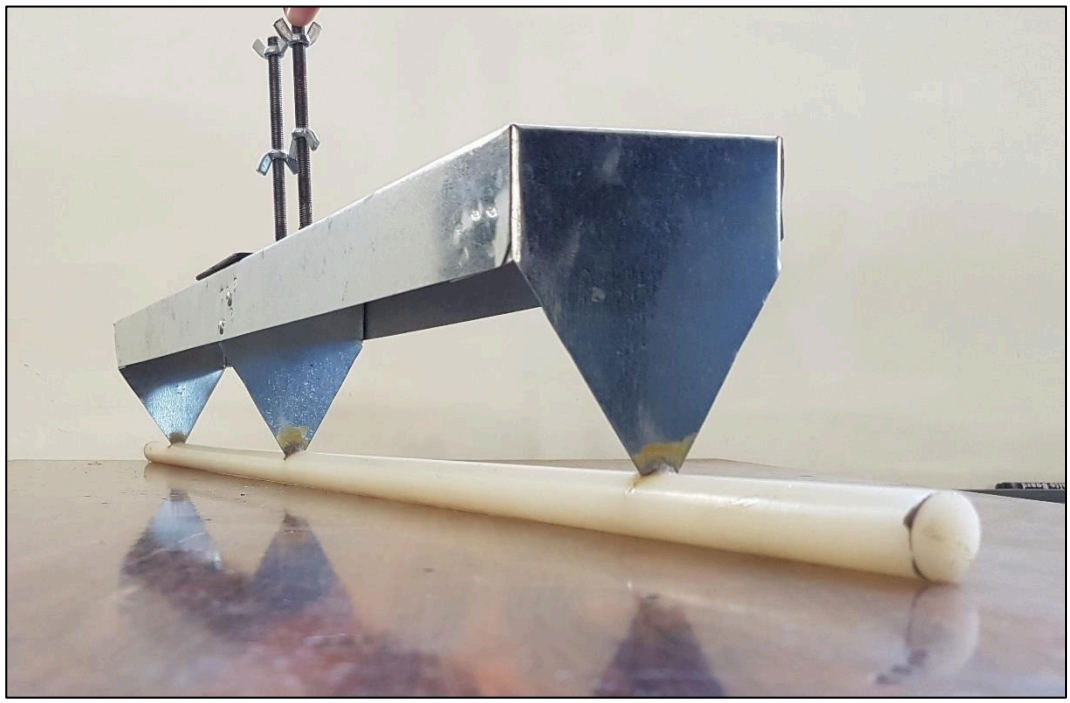

Figure B- 2: Photograph 1 of "infinitely' long cylinder apparatus for verification test



Figure B- 3: Photograph 2 of "infinitely' long cylinder apparatus for verification test



Figure B- 4: Photograph 2 of "infinitely' long cylinder apparatus for verification test

APPENDIX C

Single cylinder results

Circular cylinder

Table C- 1: Single circular cylinder experimental data

Run No.	Discharge (l/s)	Flow depth (mm)	Drag force (N)
1	3.44	251.94	0.019
2	6.03	407.94	0.029
3	11.19	248.57	0.051
4	6.44	247.19	0.021
5	17.67	244.84	0.044
6	25.00	242.64	0.068
7	12.06	251.72	0.035
8	12.25	231.22	0.040
9	25.42	424.64	0.094
10	12.50	172.92	0.052
11	16.81	216.81	0.062
12	12.50	140.87	0.062
13	22.42	245.14	0.118
14	21.56	219.16	0.080
15	16.81	160.54	0.068
16	26.72	241.68	0.160
17	17.31	144.01	0.080
18	10.75	84.35	0.050
19	21.94	169.87	0.130
20	12.50	76.44	0.107
21	27.14	157.51	0.280
22	40.97	214.63	0.480
23	57.72	242.16	0.880
24	23.25	78.35	0.445
25	27.58	84.90	0.640
26	58.47	160.00	1.410
27	27.58	67.15	0.870
28	41.81	85.18	1.680
29	59.06	100.35	2.740
30	3.86	245.04	0.003
31	5.17	247.47	0.005
32	12.06	382.98	0.014
33	22.40	391.36	0.087
34	28.86	385.02	0.133
35	36.64	380.26	0.232
36	22.39	230.27	0.118
37	22.40	201.01	0.134
38	45.28	381.65	0.377

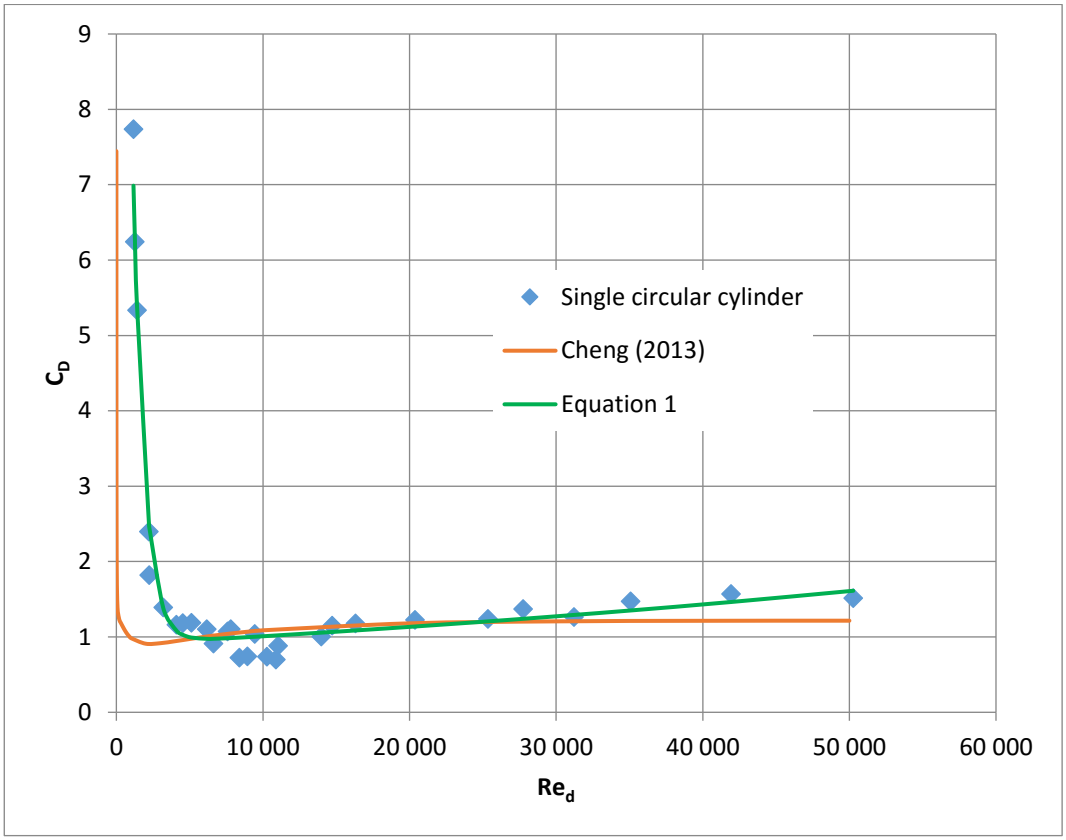

Figure C- 1: Relationship between drag coefficient and cylinder Reynolds number for a single circular cylinder.



Figure C- 2: 110 mm diameter, 250 mm long circular cylinder



Figure C- 3: 110 mm diameter, 450 mm long circular cylinder



Figure C- 4: 25 mm diameter, 450 mm long circular cylinder

Square cylinder

Table C- 2: Square cylinder data

Run No.	Discharge (l/s)	Flow depth (mm)	Drag force (N)
1	5.17	383.21	0.011
2	7.75	388.71	0.021
3	12.06	396.70	0.039
4	15.50	404.39	0.063
5	23.28	418.41	0.138
6	30.17	428.93	0.216
7	43.92	424.81	0.355
8	44.39	344.93	0.425
9	23.28	217.98	0.240
10	24.14	187.54	0.291
11	45.22	253.75	0.574
12	32.75	233.15	0.448
13	41.31	243.50	0.701
14	51.69	255.56	0.899
15	46.03	165.40	0.828
16	52.56	158.10	1.613
17	46.36	93.93	1.349
18	52.75	94.09	2.635

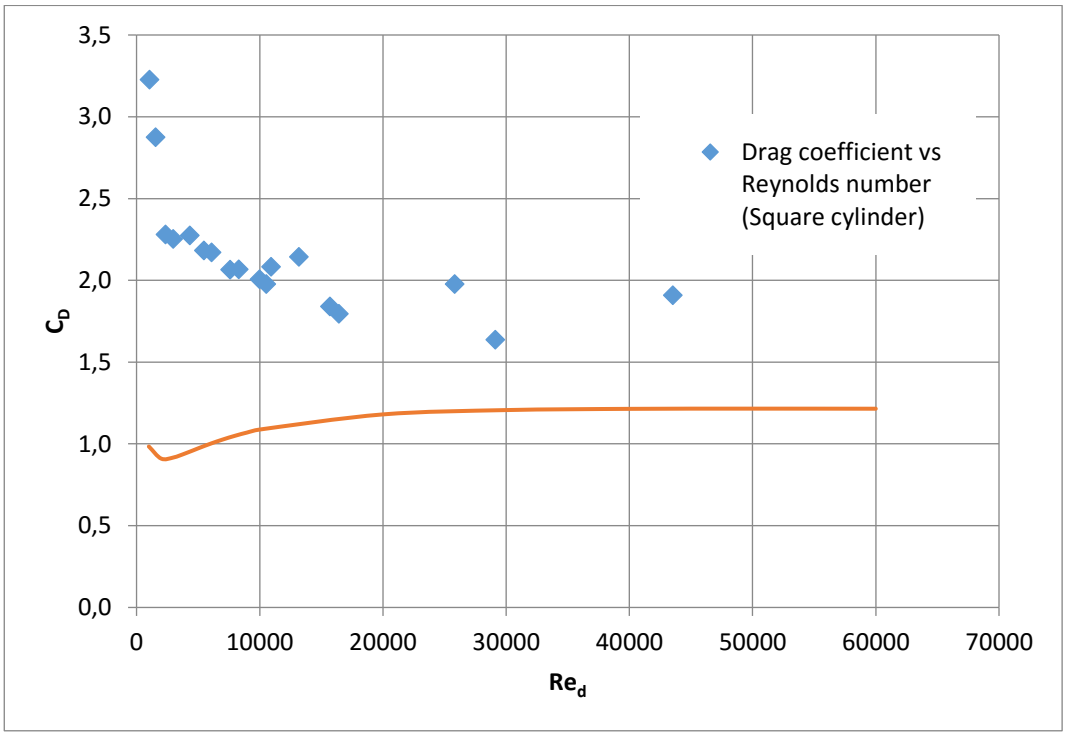

Figure C- 5: Relationship between drag coefficient and cylinder Reynolds number for a single square cylinder.



Figure C- 6: 100 mm square cylinder. (original hollow section steel)



Figure C- 7: 100 mm square cylinder (Perspex box)

Diamond cylinder

Table C- 3: Diamond cylinder data

Run No.	Discharge (l/s)	Flow depth (mm)	Drag force (N)
1	5.58	407.24	0.004
2	9.03	414.54	0.024
3	12.92	421.11	0.048
4	15.08	423.74	0.094
5	22.83	430.60	0.160
6	21.97	381.02	0.199
7	34.92	400.77	0.471
8	43.97	413.94	0.666
9	44.39	370.29	0.772
10	45.50	247.61	1.151

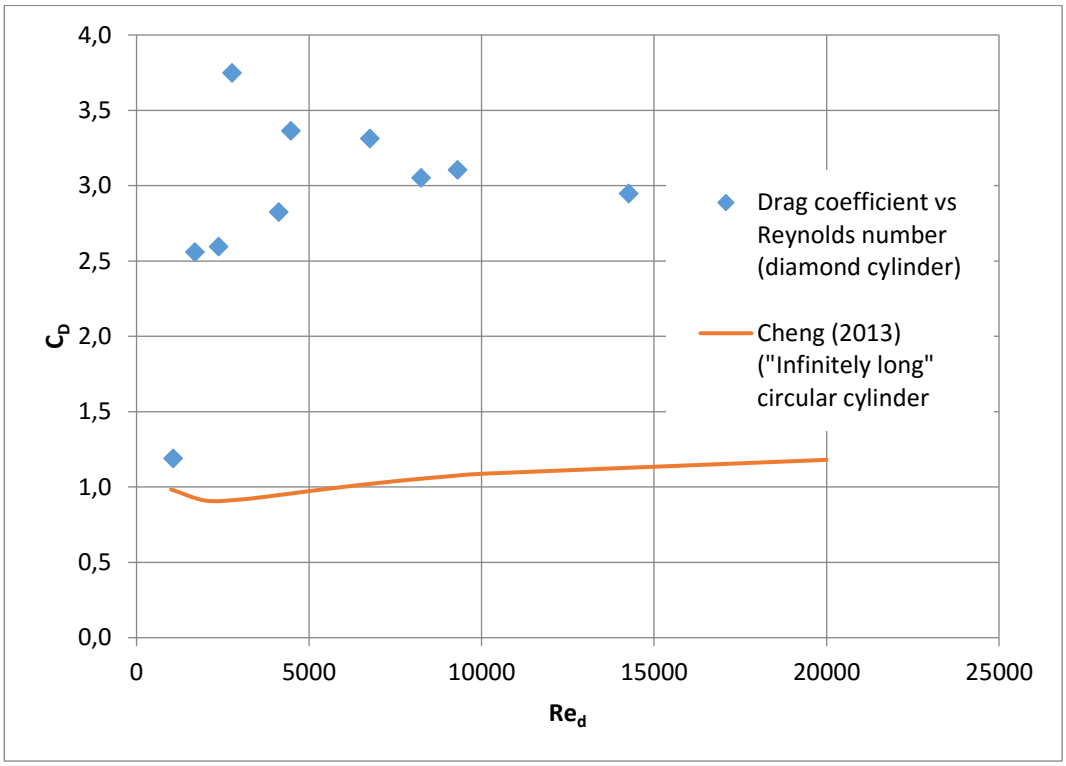

Figure C- 8: Relationship between drag coefficient and cylinder Reynolds number for a single diamond cylinder.



Figure C- 9: Alternate view of 100 mm square/diamond cylinder (Perspex box)

APPENDIX D

Multiple cylinder results

Combination 1

Table D- 1: Multiple cylinder data (Combination 1)

Run No.	Discharge (l/s)	Flow depth (mm)	Drag force (N)
1	4.31	235.03	0.010
2	6.44	240.69	0.023
3	11.64	237.42	0.075
4	15.50	245.74	0.129
5	21.50	244.83	0.236

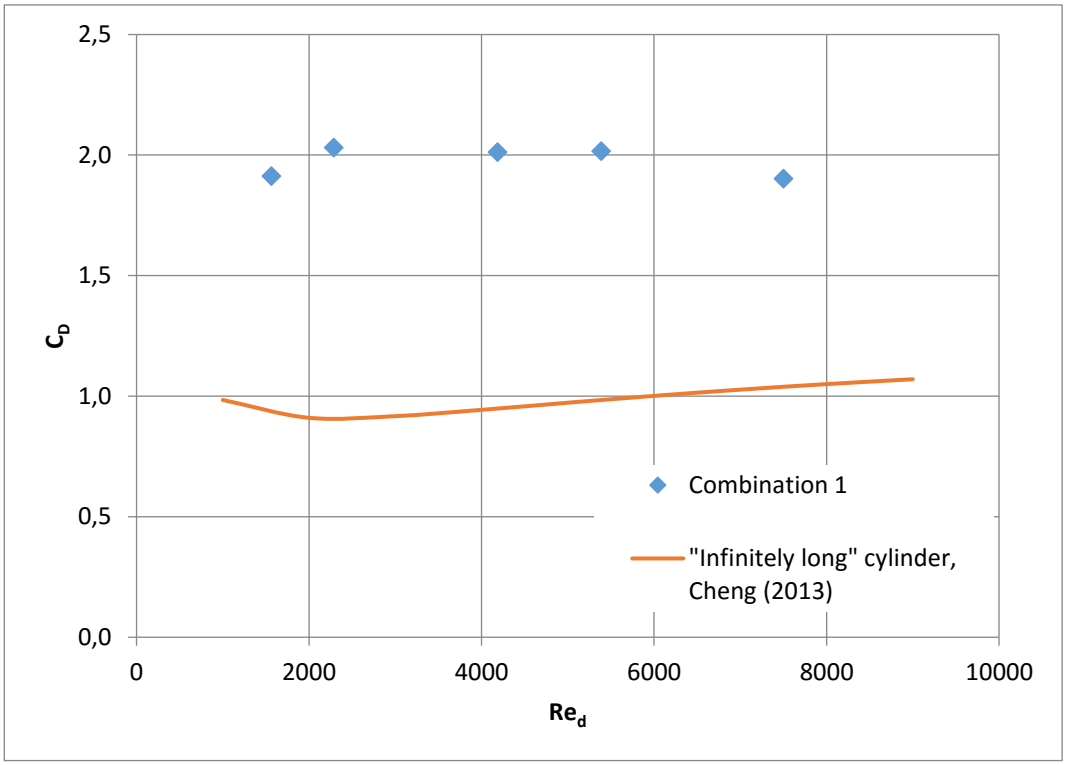

Figure D- 1: Relationship between drag coefficient and cylinder Reynolds number for multiple cylinders (Combination 1).

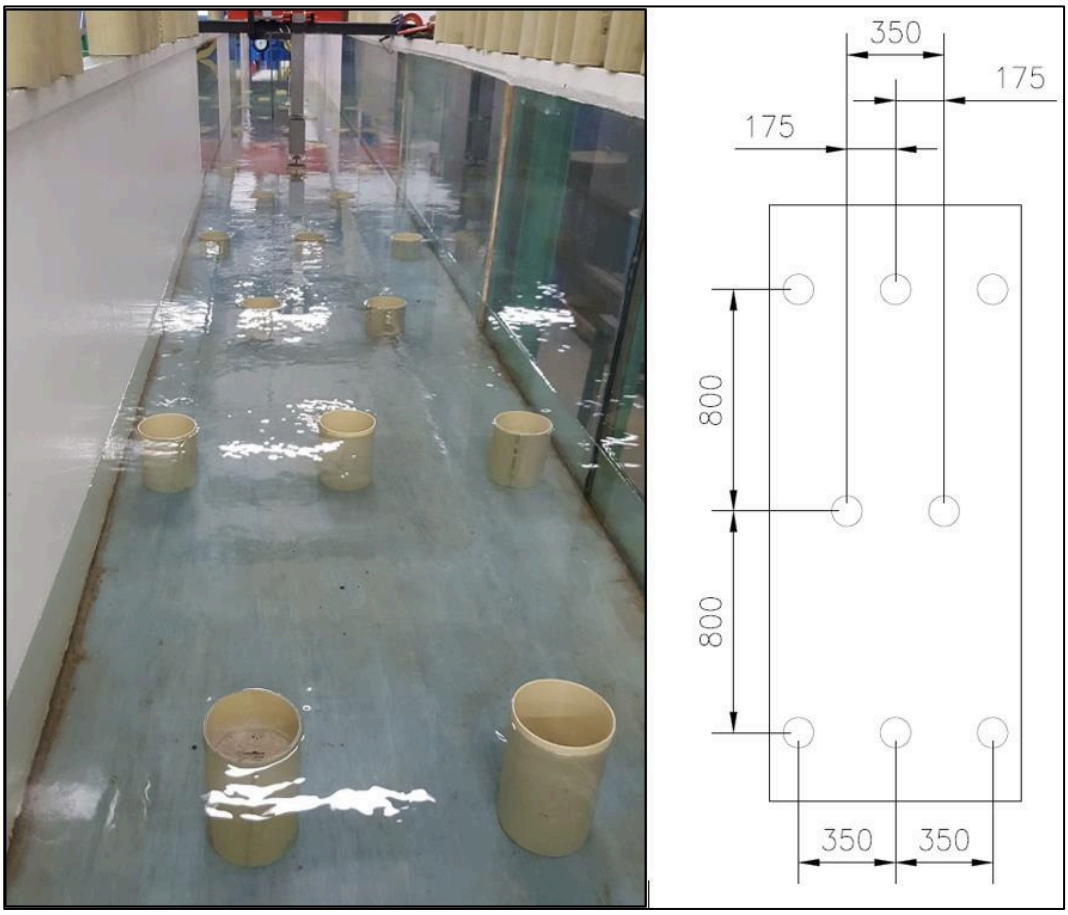

Figure D- 2: Photograph and dimensioned sketch of Combination 1.

Combination 2

Table D- 2: Multiple cylinder data (Combination 2)

Run No.	Discharge (l/s)	Flow depth (mm)	Drag force (N)
1	4.31	251.61	0.028
2	6.44	250.93	0.042
3	10.33	248.67	0.074
4	13.36	241.43	0.123
5	16.81	242.76	0.188
6	21.11	242.80	0.222

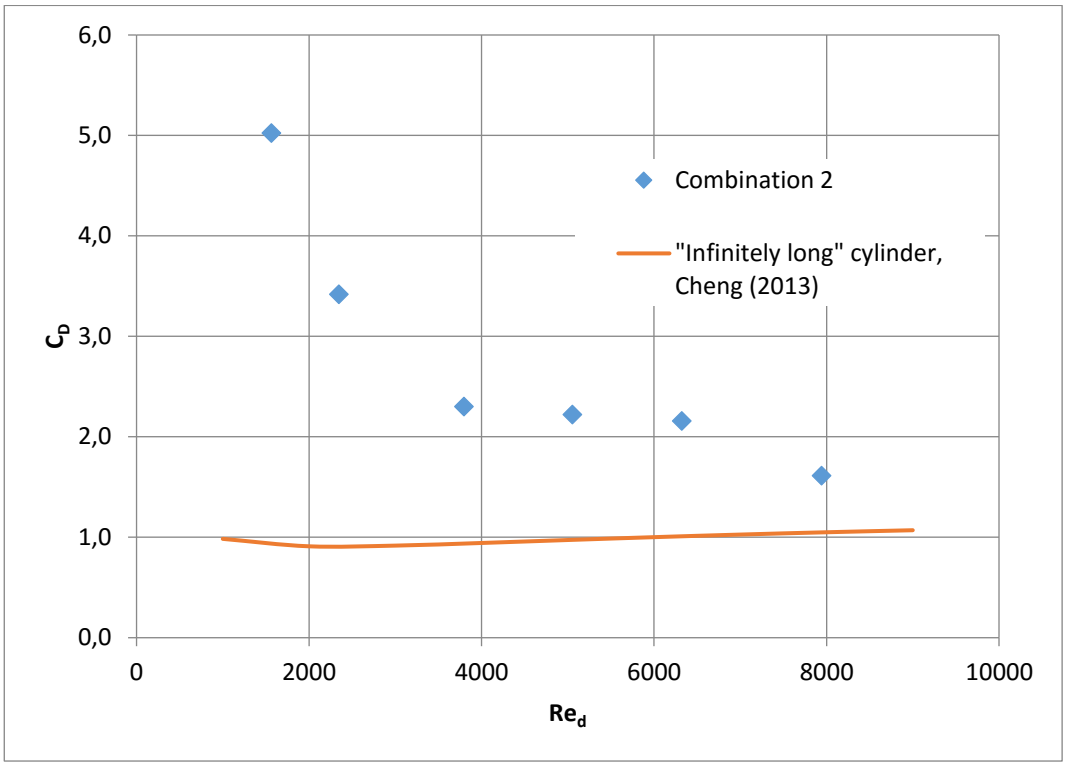

Figure D- 3: Relationship between drag coefficient and cylinder Reynolds number for multiple cylinders (Combination 2).

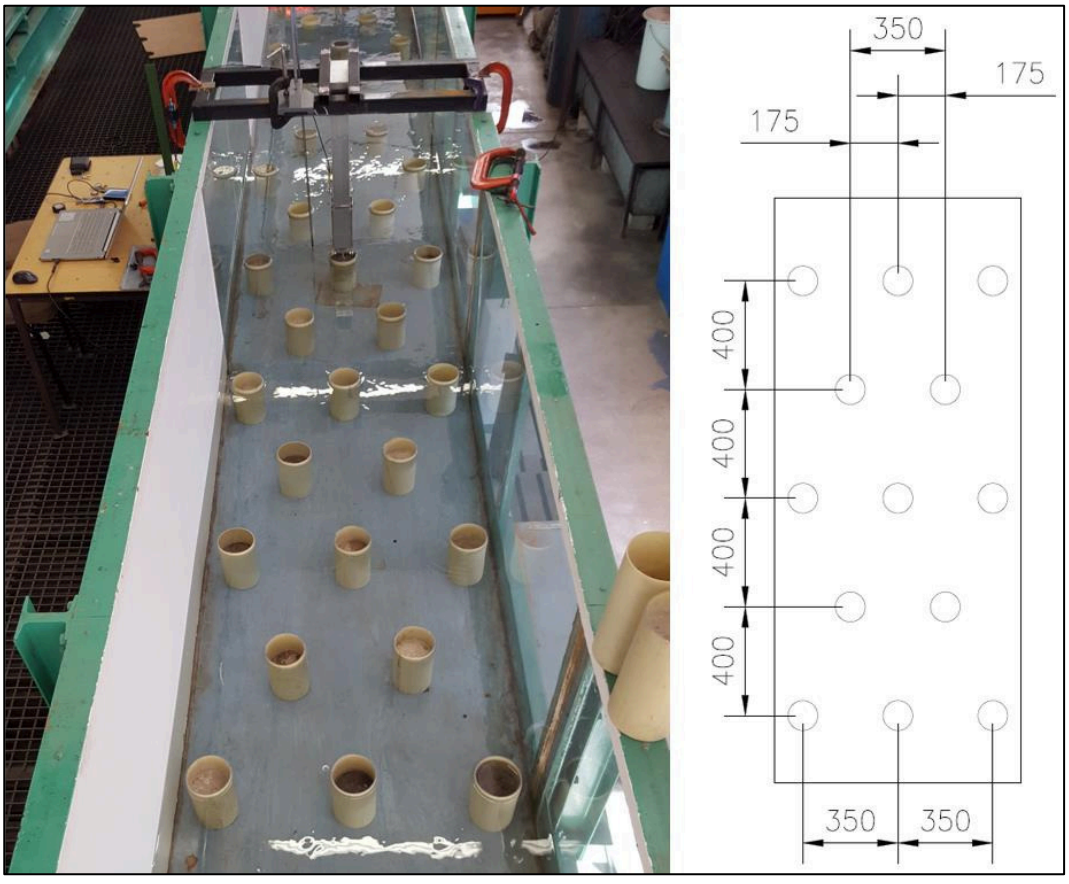

Figure D- 4: Photograph and dimensioned sketch of Combination 2.

Combination 3

Table D- 3: Multiple cylinder data (Combination 3)

Run No.	Discharge (l/s)	Flow depth (mm)	Drag force (N)
1	4.72	245.69	0.012
2	6.86	246.74	0.025
3	8.61	249.41	0.042
4	12.47	246.90	0.084
5	16.81	248.30	0.144
6	21.11	239.57	0.223

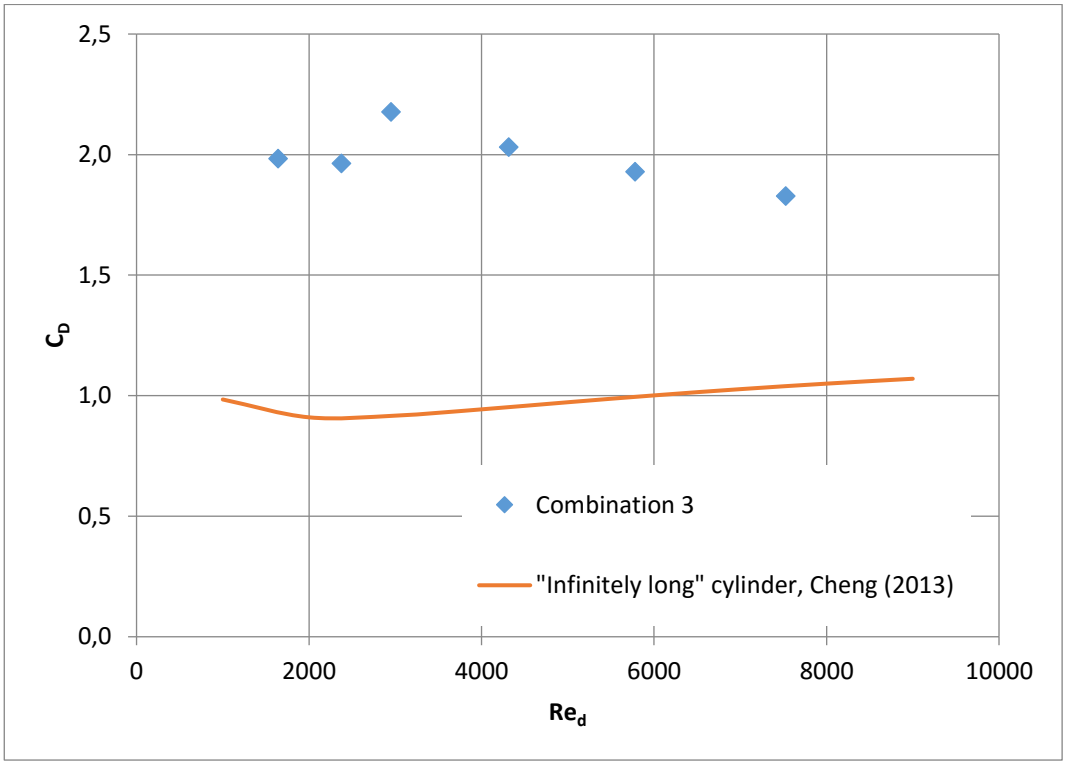

Figure D- 5: Relationship between drag coefficient and cylinder Reynolds number for multiple cylinders (Combination 3).

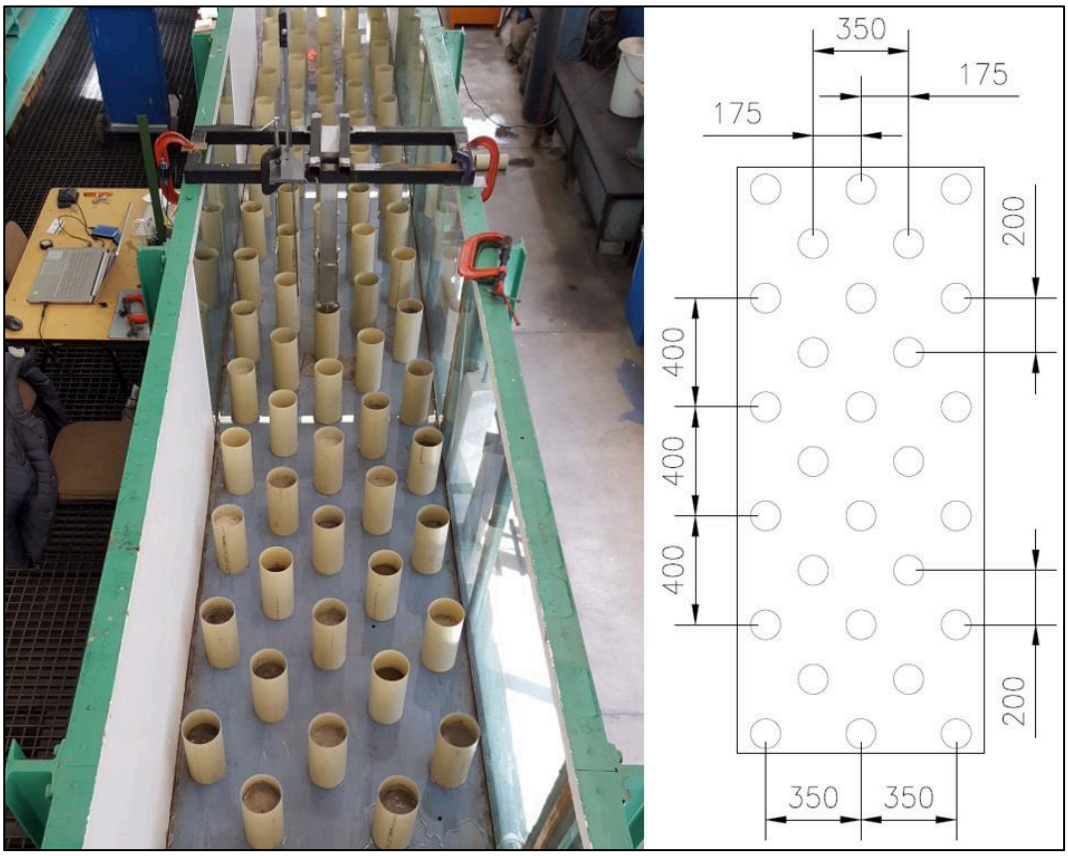

Figure D- 6: Photograph and dimensioned sketch of Combination 3.

Combination 4

Table D- 4: Multiple cylinder data (Combination 4)

Run No.	Discharge (l/s)	Flow depth (mm)	Drag force (N)
1	4.31	247.50	0.012
2	6.03	245.66	0.027
3	8.19	251.03	0.043
4	10.81	243.06	0.073
5	13.36	248.95	0.104
6	16.81	242.35	0.153
7	20.31	241.93	0.213
8	23.28	241.46	0.214

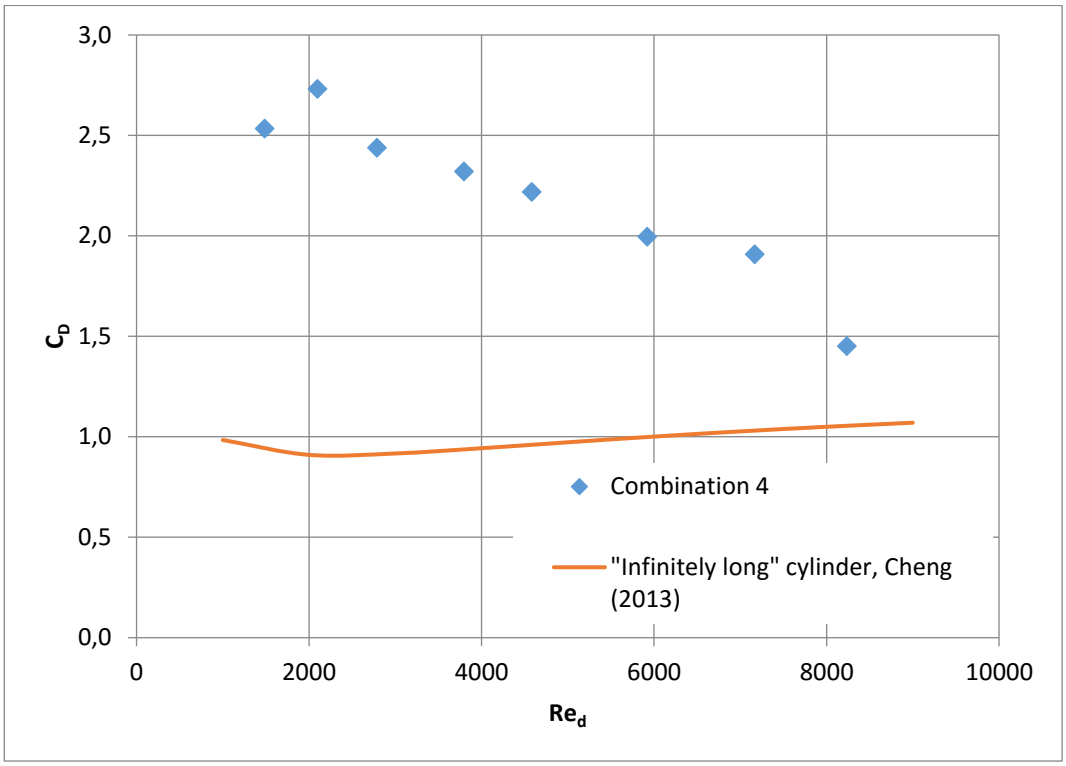

Figure D- 7: Relationship between drag coefficient and cylinder Reynolds number for multiple cylinders (Combination 4).

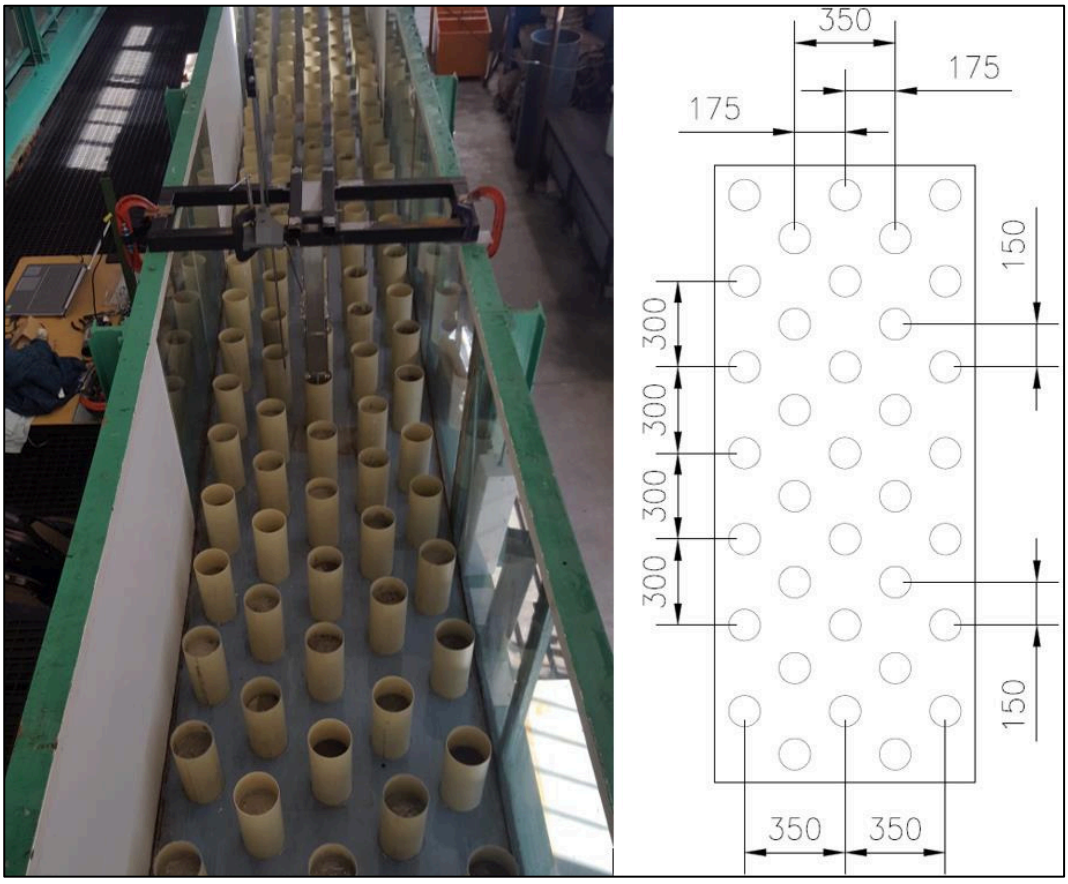

Figure D- 8: Photograph and dimensioned sketch of Combination 4.

APPENDIX E

Application for resistance prediction data (Heyneke, et al., 2014)

Table E- 1: Confirmation test data (Heyneke, et al., 2014)

Series	Discharge (l/s)	Flow depth (mm)	Areal Density (%)
A	10.17	44.76	6.65
	12.32	54.40	
	15.41	65.21	
	19.20	77.69	
	22.59	89.19	
	25.99	107.10	
	29.34	117.04	
B	8.93	31.92	3.80
	11.12	37.88	
	14.04	44.13	
	16.37	50.97	
	19.60	60.18	
	24.72	69.53	
	27.63	74.65	
	33.30	85.02	
C	9.99	28.61	2.85
	12.53	34.18	
	15.18	39.97	
	18.40	46.10	
	21.71	53.19	
	26.64	61.85	
	28.99	67.42	
	35.58	78.78	

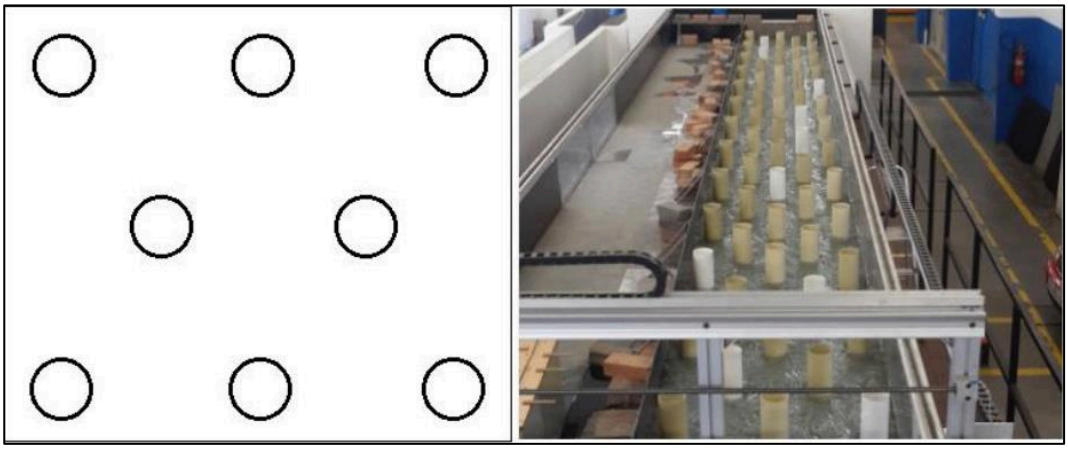

Figure E- 1: Series A cylinder layout. (Heyneke, et al., 2014)

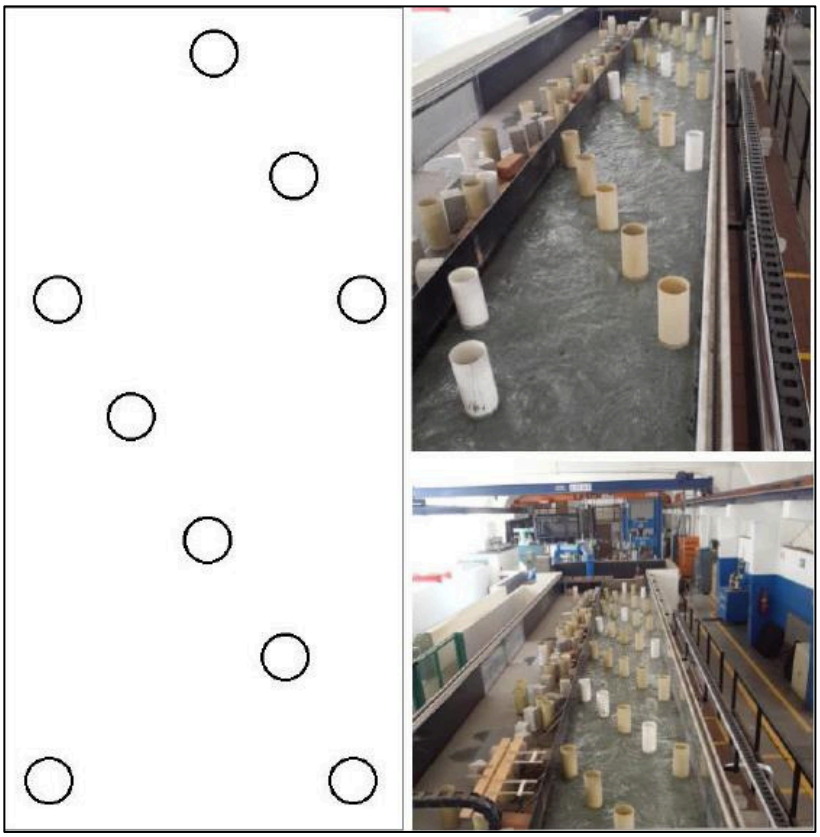

Figure E- 2: Series B cylinder layout. (Heyneke, et al., 2014)

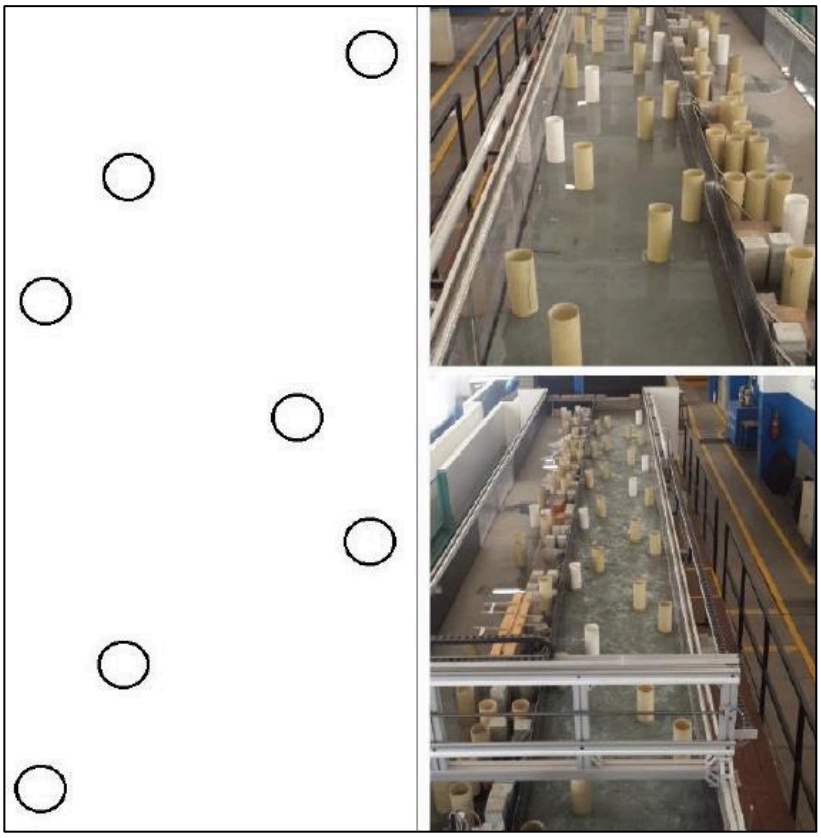

Figure E- 3: Series C cylinder layout. (Heyneke, et al., 2014)